

Vanadium and molybdenum oxide thin films on Au(111): growth and surface characterization

Dissertation

zur Erlangung des akademischen Grades
doctor rerum naturalium
(Dr. rer. nat.)
im Fach Chemie

eingereicht an der
Mathematisch-Naturwissenschaftlichen Fakultät I
Humboldt-Universität zu Berlin

von
M.Sc. Sebastien Guimond
geboren am 10.10.1977 in Quebec, Kanada

Präsident der Humboldt-Universität zu Berlin:

Prof. Dr. Dr. h.c. Christoph Marksches

Dekan der Mathematisch-Naturwissenschaftlichen Fakultät I:

Prof. Dr. Lutz-Helmut Schön

Gutachter:

1. Prof. Dr. Hans-Joachim Freund

2. Prof. Dr. Klaus Rademann

Tag der mündlichen Prüfung: 4. Juni 2009

Zusammenfassung

In der vorliegenden Arbeit wurden das Wachstum und die Oberflächenstruktur von definierten V_2O_3 -, V_2O_5 - und MoO_3 -Filmen auf $Au(111)$ sowie deren Einsatz als Modellsysteme zur Untersuchung von Elementarreaktionen auf Vanadiumoxid- und Molybdänoxid-basierten selektiven Oxidationskatalysatoren untersucht. Im Falle von $V_2O_3(0001)$ befindet sich an der Oberfläche der Filme eine Lage von Vanadylgruppen, welche kein Bestandteil der Kristallstruktur sind. Die O Atome der Vanadylgruppen können durch Elektronenbeschuss definiert entfernt werden, wodurch eine partiell oder vollständig V-terminierte Oberfläche erzeugt werden kann. Der Grad der Oberflächenreduktion wird durch die Elektronendosis festgelegt. Dieses ermöglicht eine Untersuchung des Einflusses der Vanadylgruppen und der unterkoordinierten V-Ionen auf die Reaktivität der Modellkatalysatoren. Die Präparation von defektarmen $V_2O_5(001)$ - und $MoO_3(010)$ -Filmen ist erstmals in der vorliegenden Arbeit dokumentiert. Diese Filme wurden mittels Oxidation in einer Hochdruckzelle bei einem Sauerstoffdruck von 50 mbar hergestellt. Anders als in vielen Publikationen berichtet sind diese hochkristallinen Schichten unter UHV-Bedingungen weitgehend reduktionsbeständig. Oberflächenverunreinigungen und Defekte scheinen aber einen großen Einfluss auf die Reduzierbarkeit zu haben. Die von den Strukturen der regulären Oxide abweichenden Strukturen der Koinzidenzgitter von V_2O_5 - und MoO_3 -Monolagen werden durch die Wechselwirkung mit der $Au(111)$ -Unterlage stabilisiert, was vermutlich durch die einfache Verschiebbarkeit von Koordinationseinheiten in V und Mo-Oxiden erleichtert wird. Für beide Oxide beginnt das Wachstum regulärer Oxidstrukturen erst nach Vollendung der zweiten Lage. Die für geträgerte V_2O_5 -Katalysatoren häufig vorgebrachte Annahme, dass V_2O_5 -Kristallkeimbildung direkt auf einer Monolage stattfindet, sollte somit mit Vorsicht betrachtet werden.

Abstract

The growth and the surface structure of well-ordered V_2O_3 , V_2O_5 and MoO_3 thin films have been investigated in this work. These films are seen as model systems for the study of elementary reaction steps occurring on vanadia and molybdena-based selective oxidation catalysts. It is shown that well-ordered $V_2O_3(0001)$ thin films can be prepared on $Au(111)$. The films are terminated by vanadyl groups which are not part of the V_2O_3 bulk structure. Electron irradiation specifically removes the oxygen atoms of the vanadyl groups, resulting in a V-terminated surface. The fraction of removed vanadyl groups is controlled by the electron dose. Such surfaces constitute interesting models to probe the relative role of both the vanadyl groups and the undercoordinated V ions at the surface of vanadia catalysts. The growth of well-ordered $V_2O_5(001)$ and $MoO_3(010)$ thin films containing few point defects is reported here for the first time. These films were grown on $Au(111)$ by oxidation under 50 mbar O_2 in a dedicated high pressure cell. Contrary to some of the results found in the literature, the films are not easily reduced by annealing in UHV. This evidences the contribution of radiation and surface contamination in some of the reported thermal reduction experiments. The growth of ultrathin V_2O_5 and MoO_3 layers on $Au(111)$ results in formation of interface-specific monolayer structures. These layers are coincidence lattices and they do not correspond to any known oxide bulk structure. They are assumed to be stabilized by electronic interaction with $Au(111)$. Their formation illustrates the polymorphic character and the ease of coordination units rearrangement which are characteristic of both oxides. The formation of a second layer apparently precedes the growth of bulk-like crystallites for both oxides. This observation is at odds with a common assumption that crystals nucleate as soon as a monolayer is formed during the preparation of supported vanadia catalysts.

Acknowledgements

First and foremost I would like to express my gratitude towards Prof. Hans-Joachim Freund for his support and for giving me the opportunity to pursue this PhD work in the Chemical Physics department of the Fritz-Haber-Institut. I would also like to thank Prof. Klaus Rademann for his help and for accepting to be my thesis director at the Humboldt University. Many thanks to Dr. Helmut Kuhlenbeck, who supervised my work and has been of invaluable help throughout this thesis.

I had the chance to meet a lot of great persons during my stay at the Fritz-Haber-Institute. Either as invaluable colleagues, friends or both, they all contributed to make this stay a very enjoyable period of my life. Special thanks go to Helder Marchetto, Doron Lahav, Marta Borasio, Celine Lemire, Mohammad Abu Haija, Yuriy Romanyshyn, Daniel Göbke, Alexander Uhl and Fank Höbel. I would also like to acknowledge the support of Manuela Misch and Erika Popovic. I am especially grateful for the technical support of Matthias Naschitzki, which greatly contributed to my work.

Last but not the least; I thank my friends and my family for their unfaltering support and their encouragements. This work is dedicated to them. Aurée: thanks for your support over all those years.

I am deeply grateful to Stefanie for being a part of my life and for accompanying me in the last stressful part of my work. Thanks for your patience.

Content:

| | | |
|------------|--|------------|
| 1 | <i>Introduction</i> | 6 |
| 2 | <i>Experimental</i> | 9 |
| 2.1 | Experimental setup | 9 |
| 2.1.1 | UHV systems | 9 |
| 2.1.2 | High pressure cell..... | 12 |
| 2.1.3 | Sample setup | 13 |
| 2.1.4 | Au(111) substrate | 14 |
| 2.2 | Experimental Techniques | 16 |
| 2.2.1 | Low energy electron diffraction (LEED) | 16 |
| 2.2.2 | Scanning tunneling microscopy (STM)..... | 17 |
| 2.2.3 | Photoelectron spectroscopy (PES) | 18 |
| 2.2.4 | Near-edge X-ray absorption fine structure (NEXAFS)..... | 19 |
| 3 | <i>Growth and surface reduction of $V_2O_3(0001)$ thin films</i> | 20 |
| 3.1 | Introduction | 20 |
| 3.2 | Preparation Method | 24 |
| 3.3 | Results and discussion | 25 |
| 3.3.1 | Vanadyl-terminated $V_2O_3(0001)/Au(111)$: growth and surface structure | 25 |
| 3.3.2 | Surface reduction with electrons: formation of a V-termination | 33 |
| 3.3.3 | Thermal stability of V-terminated $V_2O_3(0001)$ | 40 |
| 3.4 | Summary | 43 |
| 4 | <i>Growth of V_2O_5 thin films</i> | 45 |
| 4.1 | Introduction | 45 |
| 4.2 | Preparation Method | 47 |
| 4.3 | Results and discussion | 48 |
| 4.3.1 | Structure of the first layers | 48 |
| 4.3.2 | Thicker films: $V_2O_5(001)$ | 62 |
| 4.3.3 | Thermal stability | 74 |
| 4.4 | Summary | 82 |
| 5 | <i>Growth of MoO_3 thin films</i> | 84 |
| 5.1 | Introduction | 84 |
| 5.2 | Preparation Method | 88 |
| 5.3 | Results and discussion | 89 |
| 5.3.1 | Structure of the first layers | 90 |
| 5.3.2 | Thicker films: $MoO_3(010)$ | 99 |
| 5.3.3 | Thermal stability | 107 |
| 5.4 | Summary | 111 |
| 6 | <i>Conclusions and outlook</i> | 112 |
| | <i>References</i> | 114 |
| | <i>List of Abbreviations</i> | 121 |
| | <i>Publications</i> | 122 |

1 Introduction

Vanadium and molybdenum oxides are extensively used in heterogeneous selective oxidation catalysis, where they act as one of the key components of the catalysts¹⁻³. Both oxides have interesting physical properties and are characterized by a very rich chemistry, which somehow mirrors the diversity of possible vanadium and molybdenum formal oxidation states (ranging from +2 to +5 for V and from +4 to +6 for Mo) and coordination geometries¹.

It is known that the conversion between vanadium oxides of different stoichiometry is rather easy, and this property is one of the important factors that make vanadium oxides very good oxidation catalysts^{1,2}. They are used for instance for the oxidation of SO₂ to SO₃ (an important step in the production of sulphuric acid) and for the selective oxidation of various hydrocarbons^{1,4-6}. In these applications, a small quantity of vanadium pentoxide (V₂O₅) is dispersed on the surface of a supporting oxide such as SiO₂, Al₂O₃, TiO₂ or ZrO₂. These systems are often referred to as “monolayer catalysts”^{4,7} and depending on the support, they can have much higher reactivity and selectivity than V₂O₅ alone^{5,8}. Although it is rather clear that the supporting oxide plays an important role in influencing the electronic properties and the structure of the vanadium oxide layer, the physical origins of the improved catalytic properties are still not fully understood. Also, the exact nature (atomic structure, thickness) of the VO_x layers loosely called “monolayer” has still not been clearly elucidated. This was evidenced in a recent study, where it was shown that some of the common conclusions made on the structure of the layers based on frequency shifts observed with vibrational spectroscopy might be wrong⁹. More generally, in spite of their importance, many questions about the surface structure and the reaction mechanisms related to these highly complex systems remain unanswered. The same holds true for molybdenum trioxide (MoO₃) based catalysts, where the nature of the active sites and the reaction mechanisms at the surface are still debated^{1,3}. As detailed in section 5.1, MoO₃ and V₂O₅ have a lot of properties in common.

One of the factors hampering a more precise understanding of these systems is their considerable structural complexity. A useful approach to gain insight into these problems is the use of well-defined model surfaces, systems that are much simpler and that can be studied at the molecular level using the range of surface science techniques that are nowadays available. The V₂O₅(001) and MoO₃(010) single crystal surfaces are relevant model systems and they have been the subject of experimental and theoretical studies^{1,2,10,11}. Although such single crystals can be grown, their preparation is involved and time consuming¹². They are also sensitive to beam damage¹³⁻¹⁵ and must therefore be cleaved frequently when electron based

surface science techniques are applied, which is uncomfortable and can be a problem in view of the small crystal sizes. To avoid these complications, the possibility of growing well-ordered V_2O_5 and MoO_3 thin films would be advantageous. This has not been reported yet in the literature.

The growth of both V_2O_5 and MoO_3 thin films on a Au(111) substrate was investigated in the present study and the results are presented in Chapters 4 and 5, respectively. Due to the high oxygen content of the oxides, oxygen pressures which are not suitable for UHV systems have been used for the preparation of both systems. A dedicated high pressure cell was built for these experiments and it is described in section 2.1.3. The films have been investigated with a combination of several surface sensitive analytical methods, including low energy electron diffraction (LEED), scanning tunneling microscopy (STM), photoelectron spectroscopy (PES) and near-edge X-ray absorption fine structure (NEXAFS). In the context of model reactivity studies, the thermal stability of the V_2O_5 and MoO_3 surfaces under UHV conditions is an important factor that has to be taken into account. For that reason, the thin films were also investigated with temperature programmed desorption (TPD).

Ultrathin metal oxide films are generally important for a wide range of technological applications. They do not only play a crucial role in heterogeneous catalysis, but also in semiconductor devices and in the protection of metals against corrosion, for instance ¹⁶. Oxide layers with thicknesses in the sub-nanometer range are also interesting on the fundamental scientific level because they may exhibit physical and chemical properties that considerably differ from those of the corresponding bulk materials ^{17,18}. This is due to their limited thickness (spatial confinement) and to the relative importance of their interface with adjacent materials. Thus, understanding the properties and the growth of oxide “nanolayers” is interesting and relevant to the development of novel materials and applications. In this context, the formation of V_2O_5 and MoO_3 layers on Au(111) has been investigated for different thicknesses, ranging from a single oxide layer to films with a thickness in the ~ 5 nm range. In particular, the formation of surface specific monolayer structures on the Au(111) substrate has been given a special attention (see sections 4.3.1. and 5.3.1.).

The catalytic oxidation reactions occurring at the surface of vanadium and molybdenum oxides are often described by the Mars-van Krevelen mechanism ^{2,19}, where oxygen is transferred from the oxide to the reacting molecules (the oxygen content of the oxide being subsequently replenished from the gas phase). This implies that reduced sites will invariably form at the surface of the oxide during the catalytic reactions, even though they might be transient states (i.e. they may afterwards be reoxidized with oxygen from the gas or from the bulk of

the oxide). For vanadium oxides, it is actually often argued that lower oxidation states might play an important role in the processes occurring on the V_2O_5 based catalysts^{20,21}. For instance, the interaction of gas phase O_2 with the reduced sites may lead to activated oxygen species that can participate in the reactions (see ref.²² and references therein). For these reasons, and also due to its interesting physical properties, V_2O_3 has been the subject of many theoretical and experimental investigations (see refs.^{1,22-29}, for instance). Vanadium sesquioxide, V_2O_3 , can be produced by the reduction of V_2O_5 . The (0001) surface of V_2O_3 is preferentially exposed during the growth of thin films and it has consequently received considerable attention. A detailed STM, LEED and XPS investigation on the preparation of $V_2O_3(0001)/Au(111)$ thin films is presented in Chapter 3. The surface structure and the presence of point defects have been characterized (section 3.3.1). Earlier work has shown that the $V_2O_3(0001)$ surface is terminated by vanadyl groups under typical UHV preparation conditions^{26,28}. Dupuis *et al* also reported that the vanadyl groups can be removed by electron bombardment²⁶. Nevertheless, the reduction process along with the structure of the resulting reduced surfaces remained unclear until now. This has been investigated in details in the present study and the results are presented in sections 3.3.2. and 3.3.3.

A more detailed description of the relevant characteristics of the three systems investigated in this study, V_2O_3 , V_2O_5 and MoO_3 , are given in Chapters 3, 4 and 5, respectively.

2 Experimental

The experimental setup and the various analytical methods that were used throughout the present study are presented in this chapter. The ultrahigh vacuum (UHV) systems in which the experiments took place, the high pressure cell used for the preparation of both V_2O_5 and MoO_3 thin films, and the Au(111) substrate are first described. Following this, the surface characterization techniques are briefly introduced. The experimental conditions that were used for each technique are also given.

2.1 Experimental setup

2.1.1 UHV systems

Most of the experiments were performed in the UHV system depicted in Figures 2.1 and 2.2. This is a commercial system (Omicron) which consists of a single UHV chamber containing facilities for sample preparation (sputtering, metal evaporation) and surface characterization. The system is evacuated by a combination of a turbomolecular and an ion pumps. The base pressure of the system after bakeout is 1×10^{-10} mbar or lower. The system is equipped with a non-monochromatized dual anode (Mg and Al) X-ray gun and a hemispherical electron energy analyzer for X-ray photoelectron spectroscopy (XPS). For surface structure characterization, the system comprises LEED optics and a room temperature STM. The STM stage is contained in a side compartment which is directly connected to the main chamber. The system also includes a quadrupole mass spectrometer that can be used for residual gas analysis and for temperature programmed desorption (TPD). It is housed in an individually pumped Feulner cup³⁰ consisting of a gold-plated tube terminated by a cone which ends with a nozzle with a diameter of ~ 5 mm. This assembly can be seen on the right side of Figure 2.1 (b). In a TPD experiment, the sample surface is brought close (~ 1 mm) to the nozzle entrance. The sample is then heated at a constant rate and the mass spectrometer signal of desorbing molecules is detected as a function of the temperature. The purpose of the Feulner cup is to limit the detection of molecules desorbing from other surfaces by geometrically shielding them from the mass spectrometer. In this study, TPD was used to investigate the thermal stability of the V_2O_5 and MoO_3 films. The desorption of oxygen and VO_x or MoO_x fragments was monitored. The heating rate was kept constant at 0.5 K/s with a computer-controlled feedback system (manufactured by H. Schlichting, Germany).

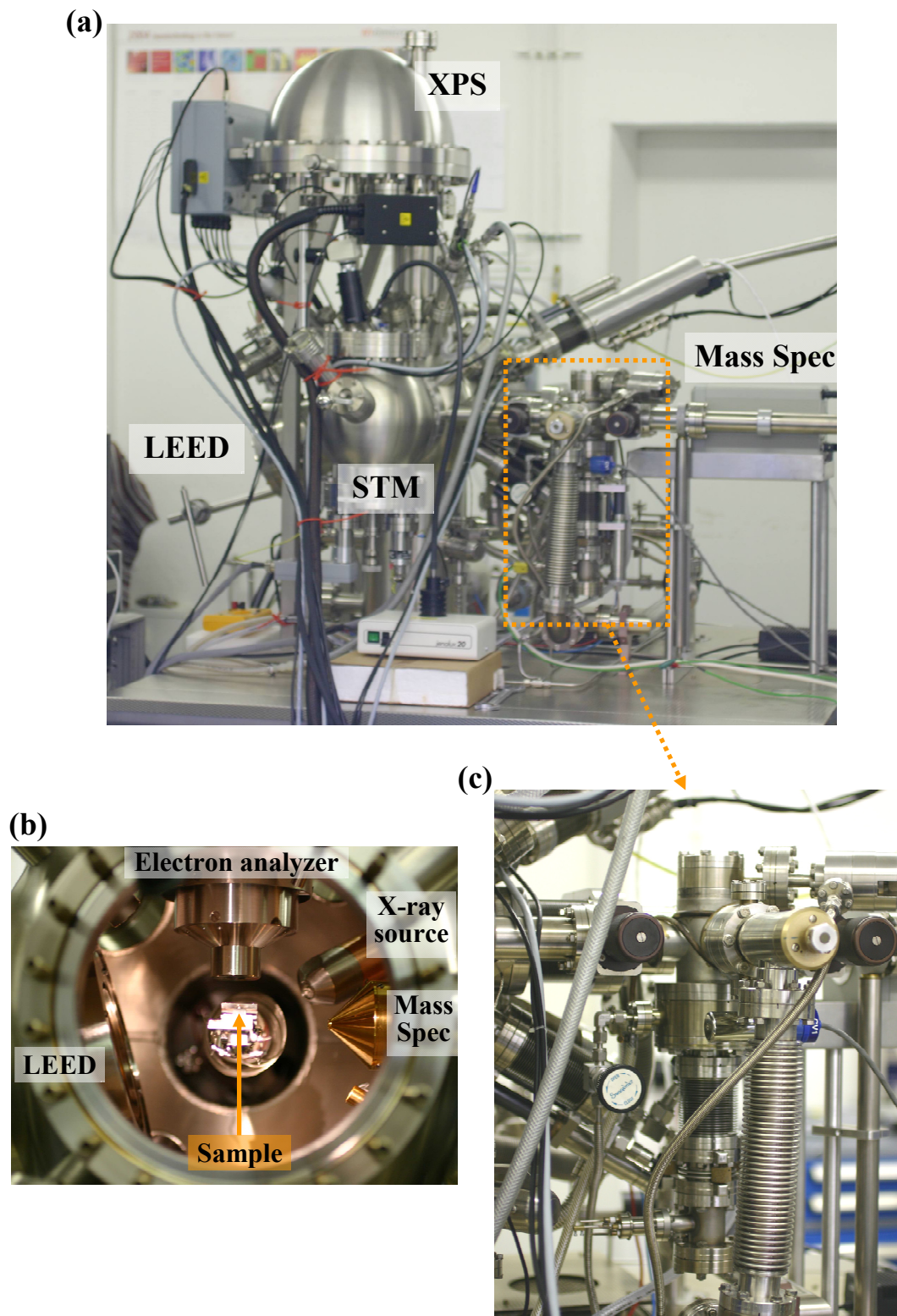


Figure 2.1. Ultrahigh vacuum system. (a): general view, (b): interior view of the vacuum chamber showing the sample position and the surrounding analysis equipment (STM compartment removed), (c): closer view of the high pressure cell.

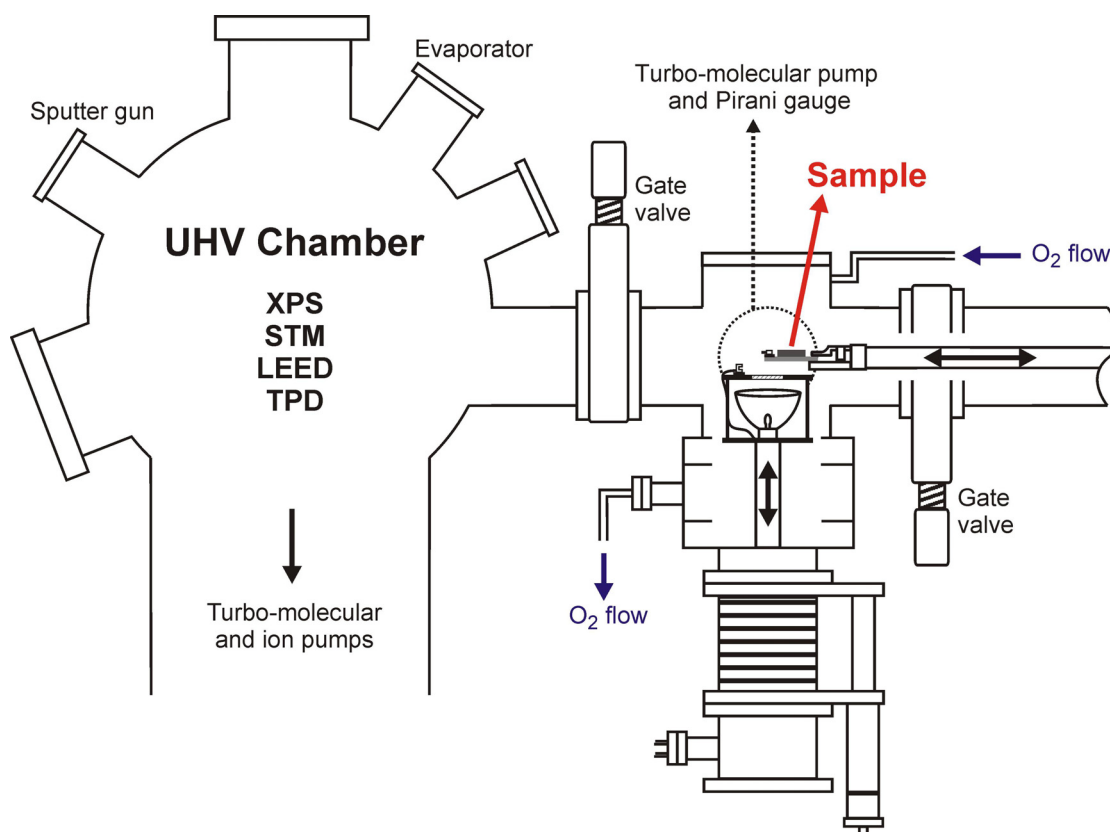


Figure 2.2. Scheme of the ultrahigh vacuum system with the high pressure cell.

The positioning (XYZ, rotation) of the sample in the UHV chamber is achieved with a manipulator. Figure 2.1 (b) gives a view of the setup along the rotation axis of the manipulator. The sample can be transferred between the manipulator and the STM stage with a wobble stick mechanism. A magnetically coupled transporter allows the transfer between the UHV chamber's manipulator and the high pressure cell (see Figure 2.2).

The NEXAFS and valence band photoemission spectroscopy experiments were carried out in another UHV system connected to the UE52-PGM undulator beamline of the BESSY II synchrotron radiation center in Berlin. This system is attached to a plane grating monochromator which delivers photons in the energy range from 90 eV to 1500 eV. The system consists of two chambers which may be separated by a gate valve. One of the chambers contains facilities for sample preparation and LEED optics. The other chamber contains a Scienta SES200 electron energy analyzer which was used for photoelectron spectroscopy. NEXAFS spectra were acquired in the same analysis chamber, either by measuring the current flowing between the ground potential and the sample (total yield detection) or by using a partial yield detector. The valence band PES and NEXAFS spectra have been recorded with linearly polarized synchrotron light. This system had a base pressure of about 5×10^{-10} mbar during the experiments.

In both systems, vanadium and molybdenum were evaporated with an Omicron EFM3 electron beam evaporator. The evaporation rate was calibrated in-situ with a quartz crystal microbalance. The same high pressure cell, sample transfer system and sample holder setup have been used in both UHV systems.

2.1.2 High pressure cell

The high pressure cell which was constructed for this study is shown in Figure 2.1 (c) and it is schematically described on the right part of Figure 2.2. It is directly connected to the chamber via a gate valve, which allows sample transfer without exposure to air. It basically consists of a small UHV chamber containing a movable sample heating stage. The high pressure cell can be evacuated by its own turbomolecular pump and it is baked-out before the experiments, allowing it to reach a base pressure around 1×10^{-10} mbar. This is important to limit possible surface contamination of the sample in the high pressure cell. With the sample inserted in its heating stage, the high pressure cell can be fully isolated from the rest of the system (i.e. from the main chamber, from the transfer mechanism and from its own pumping line) via a set of gate valves. Oxygen (99.999% purity, Linde) is then leaked from the top of the high pressure cell until the desired pressure is reached (50 mbar in the present experiments). In order to establish an oxygen flow over the sample, the gas is then evacuated from the bottom of the cell with a roughing pump. The pumping speed and the gas flow are adjusted to keep the pressure constant at 50 mbar. The use of an O_2 flow limits the possible accumulation of gas phase contaminations originating from molecules desorbing from the heated surfaces during annealing. As a further precaution, the inner walls of the high pressure cell are coated with gold (to limit adsorption of contaminations). The cell can also be water-cooled via a copper tube welded on its exterior surface. The heating stage of the high pressure cell is a movable assembly consisting of a socket for the insertion of the sample holder (see below), some thermocouple connectors for temperature measurement and a halogen lamp. The latter is located below the sample and is used to heat it from the backside. It is a 150 W halogen lamp (Osram Xenophot) which has an elliptical mirror and a focal length of 2 cm. The distance between the lamp and the sample is fixed in such a way that the backside of the sample is at the focal point of the lamp. After an oxidation step at 50 mbar and before transferring the sample back to the main chamber, the high pressure cell is evacuated with the turbomolecular pump.

2.1.3 Sample setup

To allow the transfer between the manipulator of the main chamber and the high pressure cell's heating stage, the sample was mounted on a small sample holder, as schematically described in Figure 2.3. This holder fits in the sockets built in the manipulator, the STM stage and the high pressure cell's heating stage. It is designed to enable sample heating and temperature measurement in both the main chamber and the high pressure cell. Clamps are inserted in slits on the sides of the sample to fix it against the base plate of the holder. A chromel/alumel thermocouple is fit between one of the clamps and the slit and it is pressed against the sample. The two sides of the thermocouple are connected to isolated pins, which are inserted in corresponding thermocouple plugs in the manipulator and high pressure cell sample stages. The base plate of the holder has a hole behind the sample for heating. In the manipulator of the main chamber (both UHV systems), the sample could be heated radiatively from the backside with a tungsten filament. For temperatures higher than 400°C, electron beam heating was applied by setting the sample to a positive high voltage (the W filament is electrically isolated from the rest of the manipulator and remains at ground potential). In the high pressure cell, the sample was heated from the backside with a halogen lamp (see above). Most of the sample holder parts (the base plate, the clamps and the screws) are made of platinum. This is to avoid extensive oxidation/oxygen adsorption or any gas phase transport of oxide from the holder to the sample surface during the high pressure (50 mbar) oxidation.

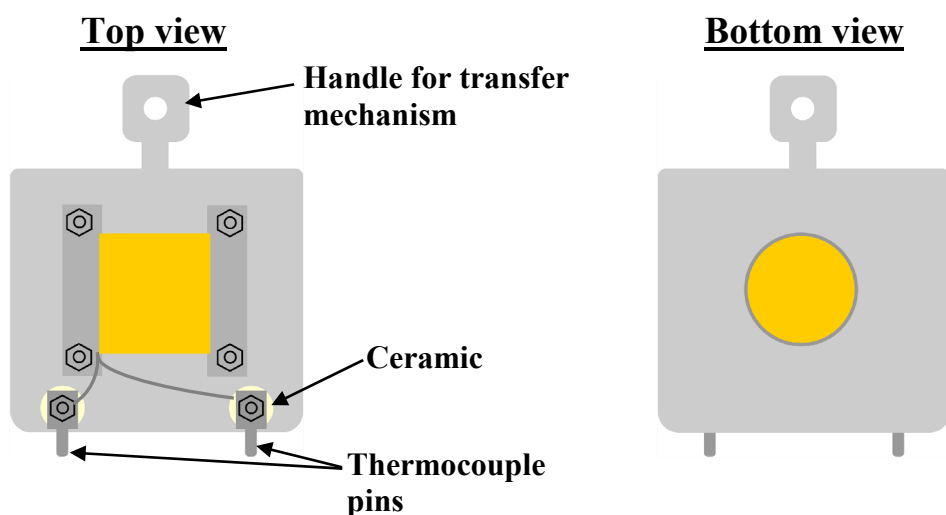


Figure 2.3. Scheme of the sample holder.

2.1.4 Au(111) substrate

The atoms in the (111) plane of Au have a hexagonal arrangement with a 2.884 Å unit cell vector^{31,32}. The Au(111) surface exhibits a characteristic “herringbone” reconstruction, which has a rectangular unit cell with lattice vectors $\sqrt{3}a$ and $22a$ ^{31,32}. This reconstruction arises from surface stress relaxation, which increases the density of Au atoms at the surface by about 4.55%. This leads to a uniaxial contraction of the topmost atomic layer with respect to the subsurface atoms and to the formation of fcc and hcp stacking regions that are separated by rows of bridging Au atoms (see Figure 2.4). The latter appear as bright stripes in the STM images. A regular arrangement of rotational domains of uniaxially contracted areas allows for a more isotropic stress distribution and gives rise to the observation of the characteristic zig-zag (herringbone) pattern.

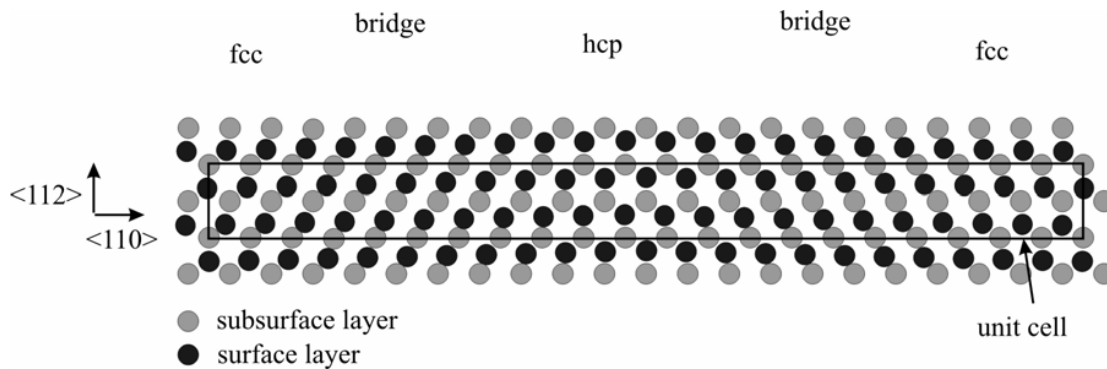


Figure 2.4. Au(111) “herringbone” surface reconstruction³¹

The Au(111) sample was cleaned by cycles of Ar^+ sputtering (4000 eV, $\sim 7 \mu\text{A}$) at room temperature and annealing at 700°C for 20 min in UHV. This procedure was repeated several times until no contaminants were detected using XPS and extended terraces displaying the Au(111) herringbone reconstruction could be observed with STM (see Figure 2.5 (a)-(d)). For a clean and well-ordered surface, faint satellite diffraction spots pertaining to the reconstruction could also be observed in the LEED pattern (Figure 2.5 (e)).

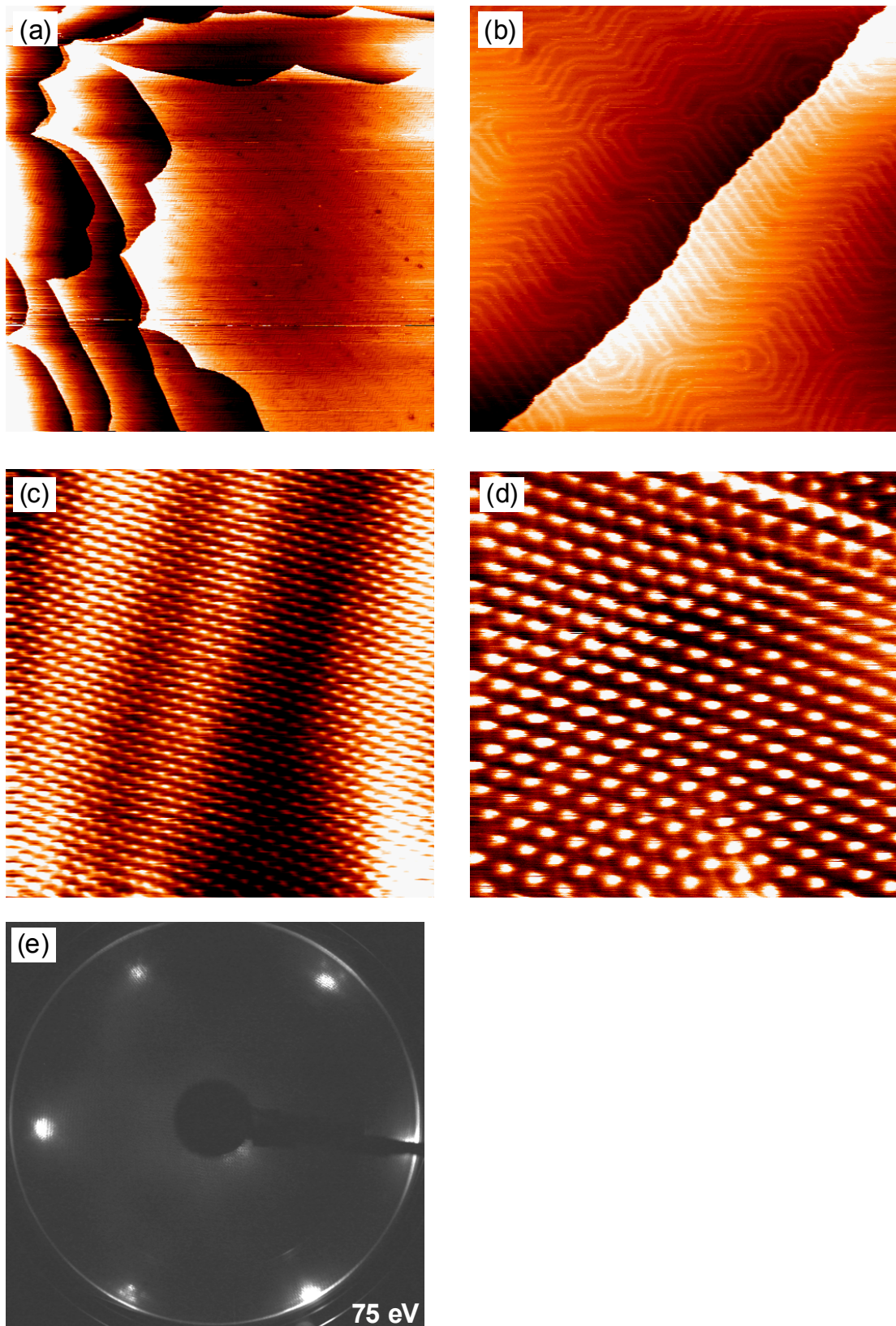


Figure 2.5. STM images ((a): 500 nm x 500 nm, (b): 100 nm x 100 nm, (c): 10 nm x 10 nm, (d): 5 nm x 5 nm. All images: 0.1 V, 1 nA) and LEED pattern of the clean Au(111) substrate.

2.2 Experimental Techniques

The analytical techniques that have been used in the present study are rather well established surface science methods. Their basic principle is only briefly described here. References are given for more detailed descriptions.

2.2.1 Low energy electron diffraction (LEED)

LEED allows the determination of the surface structure of crystalline materials^{33,34}. A typical LEED experiment uses a collimated electron beam of a well-defined low energy (usually in the range 20 – 200 eV) incident normally on the sample. As the electrons hit the sample surface, they are coherently scattered by the regular arrangement of surface atoms. The waves associated with the scattered electrons undergo a constructive interference if the path difference between waves scattered from different surface atoms is equal to an integral multiple (n) of the wavelength λ . The wavelength λ of an electron of momentum p may be calculated from the de Broglie formula:

$$\lambda = \frac{h}{p} = \frac{h}{mv}$$

where h is Planck's constant, m is the electron's mass and v its velocity. The range of wavelengths of electrons employed in LEED experiments is comparable with inter-atomic distances. The condition for a constructive interference of the scattered electrons in one dimension is given by:

$$a \sin\theta = n\lambda$$

where a is the distance between the scattering atoms and θ is the scattering angle with respect to the normal incidence beam. The integer n is often called the order of diffraction. The back scattered electrons can be detected on a phosphorescent screen, on which the diffraction pattern becomes visible. In the present work, photographs of the diffraction patterns were made with a digital camera. Only the elastically-scattered electrons contribute to the diffraction pattern; secondary electrons and the primary electrons that have lost energy due to inelastic scattering are removed by energy-filtering grids placed in front of the fluorescent screen that is employed to display the pattern. The basic reason for the high surface sensitivity of LEED is the fact that interaction between solids and electrons with energy in the 20-200 eV range is particularly strong. The electrons quickly lose kinetic energy upon penetrating the crystal due to various inelastic processes (plasmon excitations, electron-electron interactions, etc...).

2.2.2 Scanning tunneling microscopy (STM)

STM is based on the concept of quantum tunneling³⁵⁻³⁷. When a sharp conducting tip is brought very near to a metallic or semiconducting surface, the wave function of the two surfaces overlap and a bias between the two can allow electrons to tunnel through the vacuum between them. A rough approximation of the resulting current, I , is given by³⁷:

$$I = C \rho_t \rho_s \exp(-Z \phi^{1/2})$$

where Z is the sample-tip separation, ϕ is a parameter related to the barrier between the sample and the tip and C is a constant. ρ_t and ρ_s are the electron density of the tip and of the sample, respectively. Note that this expression is a significant simplification of the STM tunneling process. Nevertheless, it shows that the current is exponentially dependent on the sample-tip separation. This forms the basis of the very high spatial resolution of tunneling microscopy. The tunneling current also varies as a function of the local density of states (LDOS) close to the Fermi level of the sample. As the probe passes over the surface of a sample, changes in the tunneling conditions due to variations in the surface topography or LDOS are translated into an image. An assembly of piezoelectric transducers is used to raster the tip over the sample surface.

In principle, images can be recorded in two different ways. In the “constant height” operation mode the variation in tunneling current is recorded as the tip scans the sample surface at an overall constant height. Local variations in the topography or in the density of states at the sample surface will influence the tunneling current. In the “constant current mode”, which was used in the present study, a feedback mechanism maintains a constant current by adjusting the sample-tip separation. As the tip is scanned over the sample, the vertical position of the tip is altered to maintain a constant current. An image is then formed by the signal required to alter the vertical tip position at each point.

Tunneling spectroscopy performed in the STM provides information about the electronic structure of the sample by probing the sample surface density of states as a function of energy. In the present study, this was done by turning off the feedback mechanism and then recording the variation in current while varying the sample bias (I/V curves).

The STM apparatus used in this study is a commercial room-temperature microscope (Omicron STM1). It is based on a “tripod” configuration where the tip is rastered over the sample surface with three piezoelectric elements: two are used for the XY positioning and a third element adjusts the tip-sample separation (Z direction). The images were recorded with

both etched tungsten (Omicron) and Pt/Ir (Molecular Imaging) tips for the V_2O_3 thin films (the results were similar). However, in the case of the V_2O_5 and MoO_3 layers strong tip-surface interactions rendered the use of W tips difficult and only Pt/Ir tips could be reliably used. Tips were cleaned in-situ by mild Ar sputtering and field emission. The scanning x and y dimensions have been calibrated by imaging the unit cell of Au(111). The analysis of the images has been done with both the Omicron Scala Pro and the WSxM³⁸ softwares. Most of images presented here are unfiltered and only background corrected. FFT filtering was used in some cases to decrease spurious noise. However, this did not influence the interpretation of the images.

2.2.3 Photoelectron spectroscopy (PES)

Photoelectron spectroscopy is based on the photoelectric effect. It utilizes photoionization and energy-dispersive analysis of the emitted photoelectrons to study the composition and electronic state of the surface region of a sample^{33,34,39}. During a photoemission experiment, a sample is irradiated by monochromatic photons which excite electrons from occupied states into empty states within the solid. These electrons can then travel through the surface layer and be released into the vacuum, where they are detected by an electron energy analyzer. Depending on the photon energy, electrons from different energy levels can be photo-emitted with varying cross-sections. Typically, photons in the ultraviolet range (UPS) are used for the photoemission of valence electrons and X-rays (XPS) are employed for the investigation of core levels. The excitation by a fixed photon energy $h\nu$ populates empty states above the vacuum level in the sample and the energy distribution of the electrons measured outside the sample gives information about the distribution of occupied states (valence and core levels, depending on the photon energy). The kinetic energy (E_k) of the electrons measured in the energy analyzer is related to the binding energy of the initial states (E_i) by the following formula:

$$E_k = h\nu - E_i - \varphi$$

where φ is the spectrometer work function. The excitation of electrons from each occupied states will give rise to peaks in the photoelectric spectrum (intensity as a function of the electron kinetic energy or binding energy). These peaks generally appear superimposed on a secondary intensity background, which is due to the detection of electrons that have lost quasi-continuous amounts of energy due to multiple scattering in the crystal. The kinetic energy of the photoelectrons is usually around a few hundreds of eV for XPS, which corresponds to an inelastic mean free path in the range of 10 Å. This makes photoelectron spectroscopy a sur-

face sensitive technique. XPS can be used to identify the chemical elements present in a solid surface since the various elements have different core level binding energies. The exact core level binding energies of a specific element can also yield additional information about the chemical environment of this element. For instance, the position of the $V2p_{3/2}$ signal (which shifts from ~ 512.4 for V^{0+} to ~ 517.2 for V^{5+}) is usually used to identify V oxidation states⁴⁰. Generally, a higher oxidation state increases the effective nuclear charge which acts on the inner core electrons and increases their binding energy. A higher oxidation state also generally leads to a reduced screening of the core holes in the final state, which translates in a shift towards higher binding energy.

The XPS data presented in this study were acquired using Mg $K\alpha$ radiation (1253.6 eV). The binding energy scale of the spectra was referenced to the $Au4f_{7/2}$ peak of the clean Au(111) substrate at 84 eV⁴¹. No background intensity was subtracted from the reported spectra. However, the spectra have been corrected for X-ray satellites using the routine supplied with the CasaXPS program⁴². The valence band photoemission spectra were recorded at the BESSY II synchrotron in Berlin with a photon energy of 121 eV.

2.2.4 Near-edge X-ray absorption fine structure (NEXAFS)

NEXAFS measures the excitation probability as a function of photon energy near to the core level excitation thresholds^{34,43}. This technique requires an X-ray source with a tunable energy and must therefore be carried-out at a synchrotron. In a NEXAFS experiment, the photon energy is varied in an energy range close to an absorption edge, where core electrons are excited to unoccupied states. These transitions may lead to pronounced fine structures, which are called NEXAFS resonances. This occurs when the X-ray photon energy corresponds to the energy required for the excitation of a core level electron into a partially-filled or empty final state in the solid. Such a final state may be an unoccupied molecular orbital, for instance. Therefore, NEXAFS can give information about both the occupied and the empty electronic states in a sample. Because NEXAFS measurements involve dipole transitions from well-defined initial and final states, the application of the dipole selection rule often provides information about the local symmetry of the molecular orbitals. In this sense, NEXAFS can also be sensitive to the bond orientations in a sample.

3 Growth and surface reduction of $V_2O_3(0001)$ thin films

3.1 Introduction

At room temperature, vanadium sesquioxide (V_2O_3) has a trigonal crystalline structure isomorphic to corundum $\alpha-Al_2O_3$ and is paramagnetic metallic¹. The oxide undergoes a phase transition at a temperature around 150-170K, below which it is antiferromagnetic insulating and has a monoclinic structure. The origin of this phase transition, often considered as an example of a Mott-Hubbard transition, has been debated over the last years and it is still not completely understood (see refs.^{1,44} and references therein). The structure of trigonal corundum V_2O_3 along [0001] is described by alternating rows of O planes and two hexagonal V planes that are very close together (arbitrarily named V and V' here) in the stacking sequence ...OVV'OVV'...⁴⁵. This stacking is indicated on the model structure shown in Figure 3.1 (a). The atom density of the O planes is three times as large as that of each individual V plane (resulting in a V_2O_3 stoichiometry). As shown in the (0001) model surface structure of Figure 3.1 (c), the atoms in the O planes have a quasi-hexagonal arrangement. In contrast, the atoms of the V and V' layers are arranged together in a corrugated honeycomb pattern in the (0001) plane; see Figure 3.1 (a). The vanadium ions in V_2O_3 have a formal valence charge of +3, which corresponds to a $3d^2$ electronic configuration. In this ionic picture, the oxygen ions (O^{2-}) are expected to have a $2p^6$ configuration. However, ab initio DFT cluster studies rather suggest smaller atomic charges (between +1.6 and +2 for V and about -0.8 for O in the bulk)⁴⁶, emphasizing the importance of covalent bonding in V_2O_3 . Likewise, photoelectron and X-ray absorption spectroscopy studies indicate the presence of strong hybridization between the $O2p$ and $V3d$ states^{47,48}.

The growth of ordered V_2O_3 thin films was reported for a rather broad variety of single crystalline substrates, including Au(111)^{26,49,50}, W(110)²⁶, Pd(111)⁵¹, Rh(111)²⁸, Re(0001)⁵² and $Cu_3Au(100)$ ⁵⁰. The films were typically prepared by evaporation of metallic vanadium (with a thickness of several layers) and oxidation in $\sim 1 \times 10^{-7}$ mbar O_2 at $\sim 300-350^\circ C$ (during and/or after evaporation). In most cases, the preparation led to an ordered V_2O_3 thin film with a (0001) surface orientation (i.e. with the basal face of the corundum structure parallel to the substrate plane).

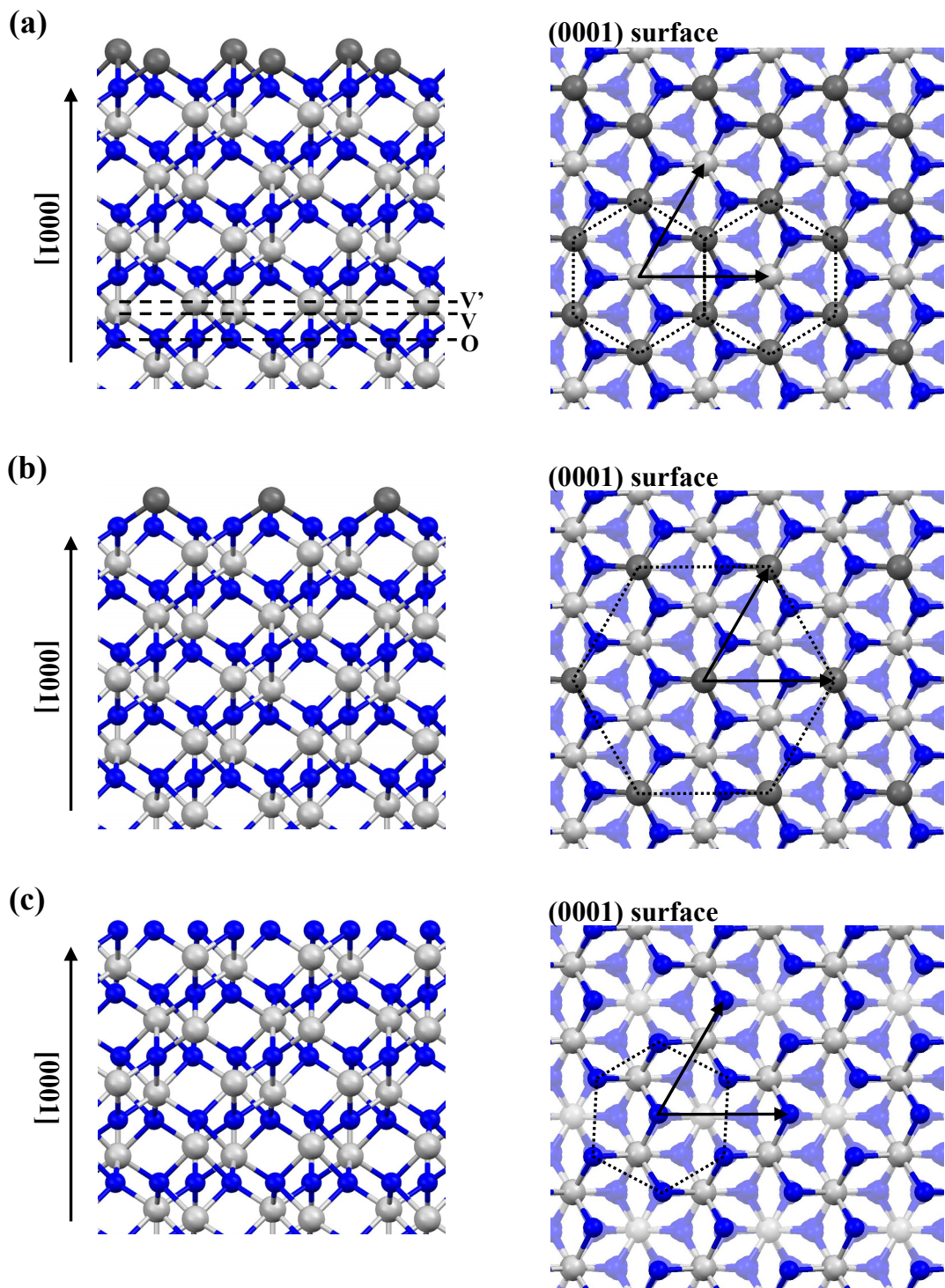


Figure 3.1. V_2O_3 geometric structure⁴⁵ showing the three possible ideal bulk-terminated (0001) surfaces (see text). (a): $\dots OVV'$ termination. (b): $\dots V'OV$ termination. (c): $\dots VV'O$ termination. Gray spheres indicate the position of the vanadium atoms while blue spheres pertain to oxygen atoms (darker gray spheres are used to highlight the position of the surface vanadium atoms). The (0001) surface unit cell is indicated by arrows for the images on the right.

The surface termination of the $V_2O_3(0001)$ thin films was investigated by several groups^{26-28,53}. In principle, cutting a V_2O_3 single crystal along (0001) could lead to three different bulk-like surface terminations: a surface exposing both V and V' layers (...OVV' stacking), a surface terminated by only one metal layer (...V'OV stacking) and a surface terminated by oxygen atoms (...VV'O stacking). These structures are shown schematically in Figure 3.1. For each termination, the image on the left displays the atomic arrangement along the [0001] direction while the image on the right gives a top view of the (0001) surface. Based on electrostatic considerations⁵⁴, the single metal layer termination (...V'OV, Figure 3.1 (b)) is the only structure which is expected to be stable. The two other terminations are polar surfaces and they are characterized by a very high Madelung potential (also when surface relaxation is taken into account⁵⁵). As shown in Figure 3.1 (b), the single metal layer termination has a hexagonal structure and a surface lattice constant of 4.91 Å⁴⁵. A single metal layer surface termination was already observed for the (0001) surface of Cr_2O_3 , which is isostructural to corundum V_2O_3 ⁵⁶.

Extensive spectroscopic and theoretical studies^{25-29,53} revealed that after preparation with the conditions typically used (see above), $V_2O_3(0001)$ is actually terminated by vanadyl groups (V=O), a structural element that is not found in the bulk structure of V_2O_3 . This “vanadyl-terminated” surface is similar to the single metal layer termination depicted in Figure 3.1 (b), with the exception that each vanadium atom at the surface forms a double bond with an extra oxygen atom (...VV'O-V=O stacking, see Figure 3.2). The vanadyl groups were also found to be aligned with the bond axis perpendicular to the surface (i.e. they are standing upright)²⁸. The presence of these surface species can be detected with various spectroscopic techniques: vanadyl groups have a specific signature in vibrational spectroscopy and they can also be distinguished with photoelectron spectroscopy and NEXAFS^{26,28}. The vanadium ions of the vanadyl groups at the $V_2O_3(0001)$ surface effectively have a higher oxidation state than their bulk counterpart. Formally, they have a 5+ oxidation state. Considering this, it is near at hand to state that the vanadyl-terminated $V_2O_3(0001)$ surface can be related to vanadium pentoxide (see Chapter 5). However, one should note that the vanadium ions of the $V_2O_3(0001)$ surface vanadyl groups are four fold coordinated, in contrast to the 5-fold coordinated V ions found in V_2O_5 .

As shown by the findings of Dupuis *et al*²⁶ and Schoiswohl *et al*²⁸, the vanadyl groups on $V_2O_3(0001)$ are thermally very stable in UHV. They remain on the surface after annealing up to a temperature of 750°C, above which the film itself decomposes. This obviously prevents the possibility of removing the vanadyl groups by simple annealing steps. Nevertheless,

Dupuis *et al* reported that the vanadyl groups can be removed by electron irradiation²⁶. This was shown by the disappearance of the various V=O spectroscopic signatures after the irradiation. The authors also showed that the vanadyl terminated surface can be relatively easily retrieved upon oxygen adsorption. A more detailed investigation of the adsorption of oxygen on the $V_2O_3(0001)$ surface reduced by electron irradiation was reported later by Abu Haija and coworkers²². Being able to remove completely or partially the vanadyl groups in a selective way is of some interest for reactivity studies, where it allows probing the role of the vanadyl groups, for instance. The adsorption of H_2O , CO , CO_2 , propane, propene and methanol was compared for the vanadyl-terminated and the reduced (i.e. without V=O groups) $V_2O_3(0001)$ surfaces^{23,24,57,58}. Whereas only molecular adsorption generally takes place on the V=O terminated surface, several dissociation reactions were observed on the reduced surface.

The present investigation took place in the context of these studies, and it aimed at better characterizing and understanding the surface structure of both the vanadyl terminated and the reduced $V_2O_3(0001)$ thin films. For this purpose, a combination of STM, LEED and XPS measurements were carried-out. First, the growth of the $V_2O_3(0001)$ thin films on Au(111) and the presence of defects on the as-prepared vanadyl terminated surface were investigated. The electron induced surface reduction was then examined in more details. So far, a detailed structural investigation was lacking and it was simply assumed that the reduction process only removes the vanadyl oxygen atoms and leaves behind a single V layer termination (as depicted in Figure 3.1 (b)).

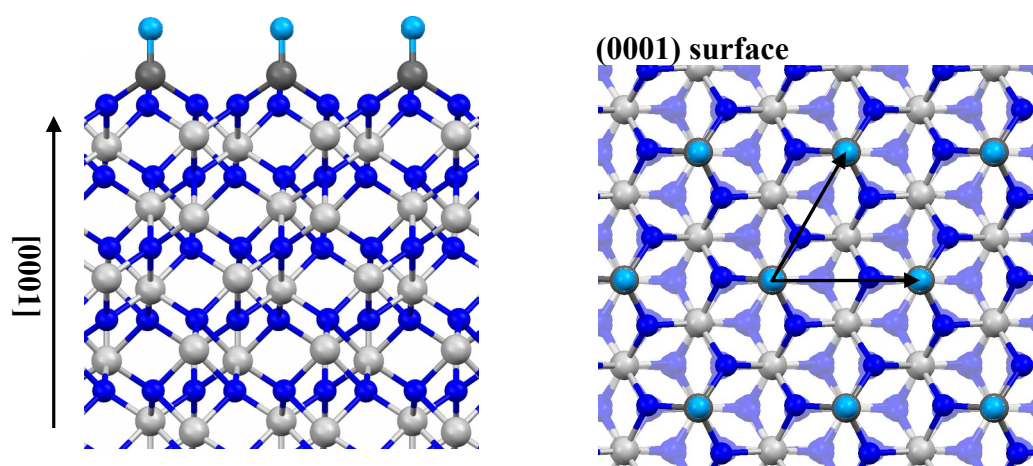


Figure 3.2. Geometric structure of V_2O_3 with vanadyl-terminated (0001) surface. Gray spheres indicate the position of the vanadium atoms while blue spheres pertain to oxygen atoms (light blue balls highlight the position of the vanadyl oxygen atoms).

3.2 Preparation Method

The films were prepared by reactive evaporation of vanadium in a partial pressure of oxygen ranging between 5×10^{-8} mbar and 5×10^{-7} mbar. During the evaporation, the Au(111) substrate was kept at 300°C . The amount of deposited vanadium was equivalent to a metallic V thickness of about 50 \AA and the evaporation rate was kept around $0.5 \text{ \AA}/\text{min}$ (calibrated in situ with a quartz crystal microbalance prior to the thin film preparation). This quantity of evaporated vanadium corresponds to an oxide film thickness of about 100 \AA . As compared to the ultrathin films described in chapters 4 and 5, the V_2O_3 films can be considered as thick films. As shown below, annealing in UHV was necessary to order the films after the deposition. Au(111) was chosen as a substrate because its surface lattice provides a good base for the epitaxial growth of $\text{V}_2\text{O}_3(0001)$ ²⁶: Au(111) is characterized by a hexagonal lattice with a 2.884 \AA unit cell, which is close to the average oxygen-oxygen distance (2.86 \AA) in the quasi-hexagonal O planes of $\text{V}_2\text{O}_3(0001)$, see Figure 3.1 (c). Nevertheless, since the preparation of ordered $\text{V}_2\text{O}_3(0001)$ was also reported for various other substrates (see above), it is possible that a good lattice match with the substrate is not crucial for this system.

The procedure used for the surface reduction of the thin films is depicted in Figure 3.3. A tungsten filament was brought at a distance of 2 mm in front of the sample surface and heated until it starts emitting electrons. To accelerate the electrons towards the thin film surface, the sample was set to a potential of 500 V. The electron emission current between the filament and the sample was kept constant at 1 mA.

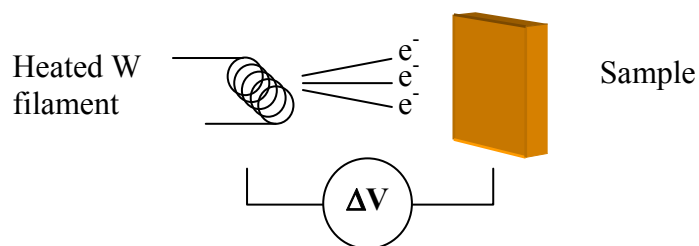


Figure 3.3. Schematic description of the procedure for surface reduction with electron irradiation.

In order to vary the degree of surface reduction of the thin films (see section 3.3.2), different irradiation times were used. For these experiments, the sample and the tungsten filament were always set at the same position. The irradiation duration was however kept short enough to limit electron bombardment-induced heating. Typically, the sample temperature reached

about 60°C after the longest irradiation time used here, 20 seconds. Higher electron doses were used for some experiments, in which cases the surface was simply irradiated in several cycles of 20 sec, the sample being allowed to cool down between each cycle. The electron dose is proportional to the emitted electron current multiplied by the total irradiation time. Precise values of the electron dose for the sample surface (in $\mu\text{C}/\text{cm}^2$, for instance) are not reported here since a fraction of the emitted electrons most probably reaches the sample holder which is also set to 500 V. Nevertheless, at least a reasonable part of the whole electron dose impinges onto the sample (which has an area of $\sim 0.5 \text{ cm}^2$)

3.3 Results and discussion

3.3.1 Vanadyl-terminated $\text{V}_2\text{O}_3(0001)/\text{Au}(111)$: growth and surface structure

As shown in Figures 3.4 (a) and (b), the as-deposited films have a high surface roughness and are not very well ordered. These data were acquired for a film prepared by the deposition of about 40 Å V in a partial pressure of 1×10^{-7} mbar O_2 , with the Au(111) substrate kept at 300°C. The large scale STM image reveals a film consisting of clusters with lateral dimensions on the order of 10 nm. The corresponding LEED pattern indicates that the crystallites are ordered to a limited extent: although the spots are broad and diffuse, they can be related to the hexagonal structure of corundum $\text{V}_2\text{O}_3(0001)$ with a ~ 4.9 Å lattice constant⁴⁵. While the as-deposited films are not well ordered, their stoichiometry corresponds to V_2O_3 . This can be deduced from the XPS spectrum shown in Figure 3.5. The maxima of the $\text{V}2\text{p}_{3/2}$ and $\text{O}1\text{s}$ peaks appear at binding energies of 515.8 eV and 530.2 eV, respectively, which corresponds very well to the reported XPS data for V_2O_3 ^{26,28,47}.

A series of annealing steps in UHV was carried-out to order the films. Increasing the annealing temperature up to 600°C led to a drastic improvement, as displayed in Figures 3.4 (c)-(f). Large scale STM images show extended terraces separated by steps of monoatomic height (apparent height ~ 2.5 Å). STM images acquired at higher resolution (Figure 3.4 (e) and (f)) reveal a well ordered surface with a $\text{V}_2\text{O}_3(0001)$ 4.9 Å hexagonal unit cell (indicated by a grey parallelogram on Figure 3.4 (f)). Likewise, the LEED patterns exhibit sharp spots (see Figure 3.4 (d)) and confirm the high degree of surface order.

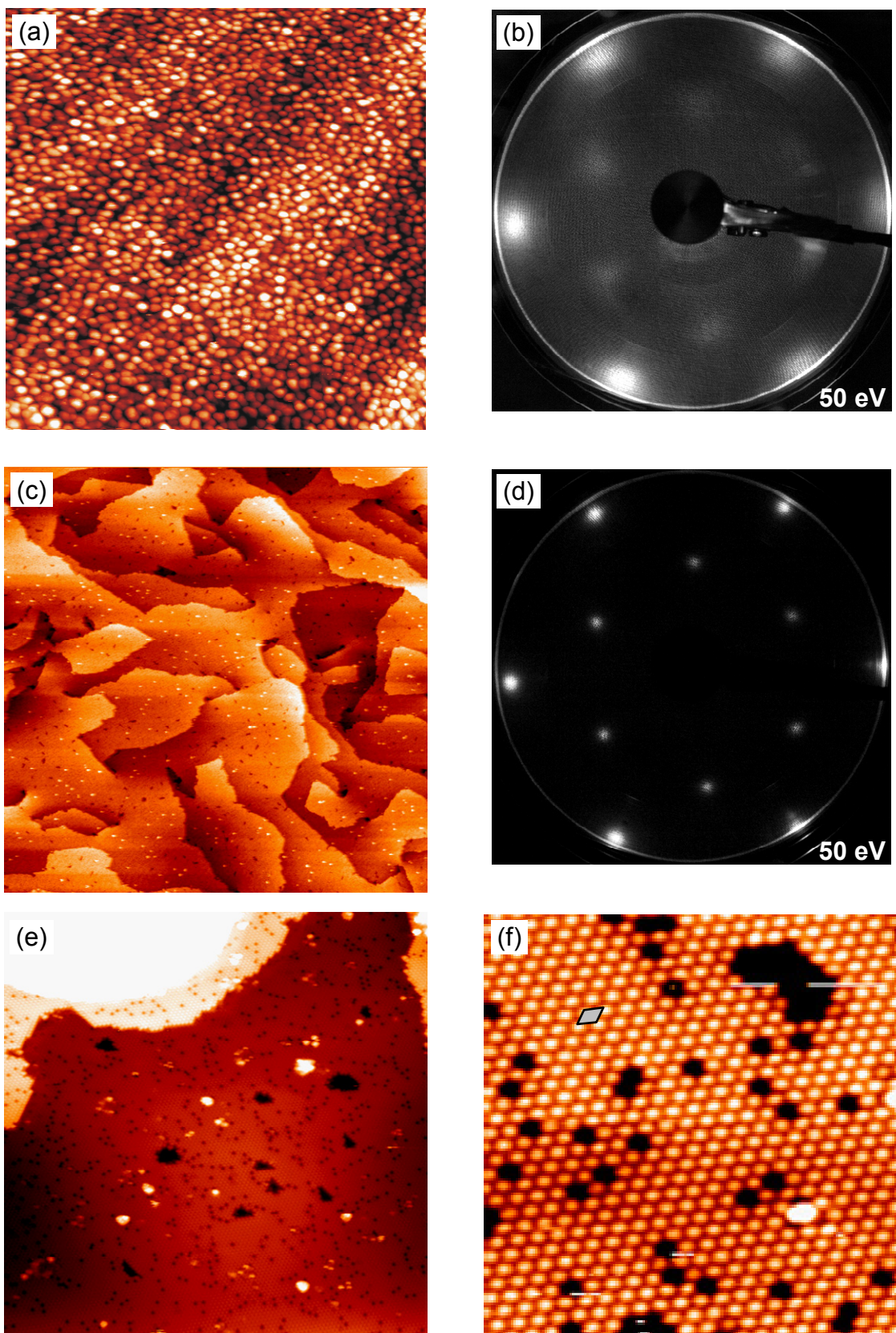


Figure 3.4. STM images ((a): 300 nm x 300 nm, 3 V, 0.2 nA, (c): 200 nm x 200 nm, 3 V, 0.2 nA, (e): 50 nm x 50 nm, -1.5 V, 0.2 nA, (f): 10 nm x 10 nm, -1.5 V, 0.2 nA) and LEED patterns obtained for a V_2O_3 film deposited on Au(111). (a), (b): immediately after deposition. (c)-(f): after an additional annealing step at 600°C in UHV.

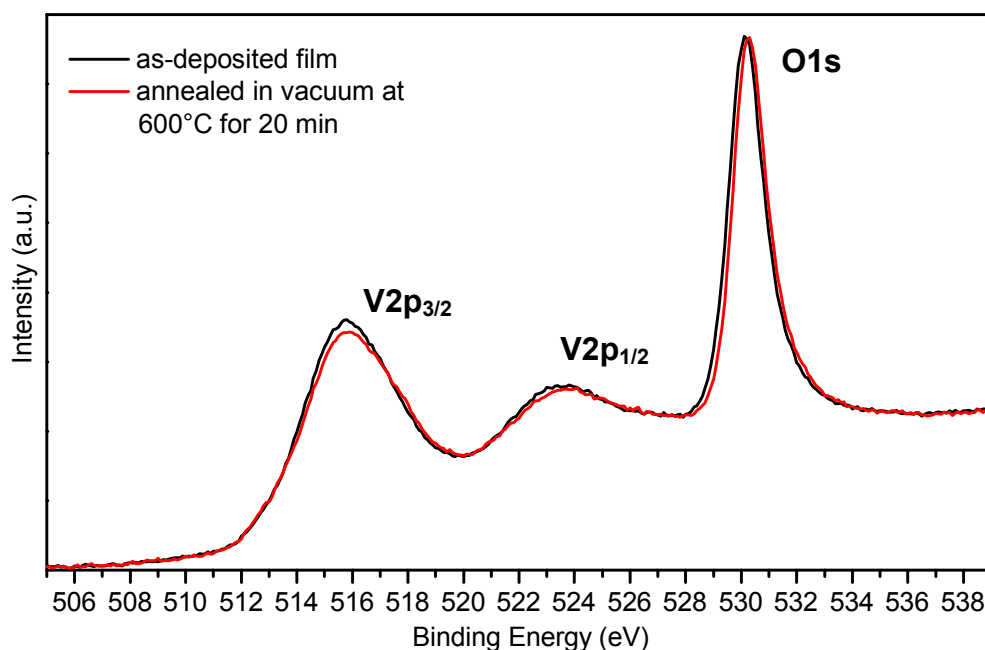


Figure 3.5. XPS spectra (V2p and O1s region) of a V_2O_3 film deposited on Au(111), immediately after deposition and after an additional annealing step at 600°C in UHV. The intensity was normalized to the background signal at 500 eV. Mg $K\alpha$, $\theta = 70^\circ$.

The films are also rather flat and cover the whole surface of the substrate. This can be deduced by the absence of holes in the STM images and by the extinction of Au signals in the XPS spectra (which is also due to the thickness of the film). Annealing the films at 600°C in UHV leads to slight changes in the V2p and O1s core level PES signals (see Figure 3.5). A shoulder on the high binding energy side of the V2p peaks gets more prominent and the O1s peak slightly shifts towards higher binding energy. The shoulder on the high binding energy side of the V2p signal can be attributed to the contribution of the surface vanadyl groups^{26,28}. In a simple picture, the vanadium ions involved in the vanadyl bonds have a higher oxidation state than those of the V_2O_3 bulk structure. This leads to a stronger initial core electron binding energy and to a lower screening of the core holes by the valence electrons, resulting in a measured higher binding energy for the core level photoelectric signals²⁹. The contribution of the surface vanadyl groups to the V2p_{3/2} peak intensity was reported to appear at a binding energy of about 517.2 eV^{26,28,29}, a position which is characteristic for V_2O_5 (see chapter 4 or ref.⁴⁷, for instance). The relative intensity increase of the V2p high binding energy shoulder observed here after the annealing at 600°C is in line with the ordering of the film and the increase of the terrace area covered by vanadyl groups (as shown in Figure 3.4). Annealing in UHV at temperatures higher than 600°C does not lead to any additional improvement in the surface order of the films. Actually, no significant changes in both the surface structure (STM,

LEED) and composition (XPS) were observed up to 670°C. However, upon annealing at 700°C the layers start decomposing and dewetting: large gaps can be observed, in which the Au(111) surface can be imaged with STM (see Figure 3.6).

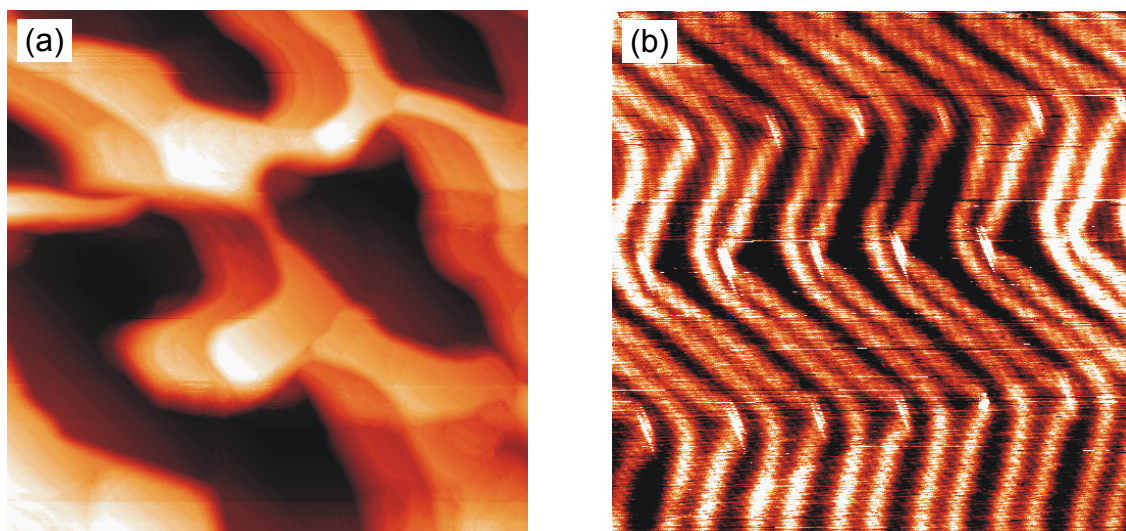


Figure 3.6. STM images ((a): 300 nm x 300 nm, 3 V, 0.2 nA, (b): 50 nm x 50 nm, 0.1 V, 10 nA) obtained after the annealing of a $V_2O_3(0001)/Au(111)$ film in UHV at 700°C for 30 min. Image (b) was acquired in one of the dark contrast areas of figure (a).

The STM images displayed in Figures 3.4 (e) and (f) show two different types of point defects: diffuse bright features and single missing bright protrusions. The origin of the diffuse bright “blobs” is still unclear. The density of these features seems to vary as a function of the precise sample history (annealing, exposure to oxygen, time in vacuum before the STM analysis, etc) but no clear trend can be found as a function of the oxidation/reduction of the sample, for instance. They could be attributed to some adsorbate or to occasional strong tip-sample interactions. The diffusion of small quantities of Au from the substrate is not expected but can not be totally ruled out (such a small quantity would be difficult to detect with XPS). The majority of the other type of point defects, the missing bright protrusions (i.e. the dark spots), can be identified as oxygen-rich point defects. These point defects must be distinguished from the more extended dark contrast areas on the terraces, which are simply lower terraces (separated by a step edge). The presence of oxygen-rich point defects on the (1x1) vanadyl-terminated $V_2O_3(0001)$ surface was also reported by Schoiswohl *et al*²⁸. They have observed that dosing the film surface with O_2 at 400°C (with O_2 partial pressures between 1×10^{-8} mbar and 1×10^{-6} mbar) leads to a progressive increase of the missing bright protrusions. Eventually, these point defects form ordered arrays with a $(\sqrt{3} \times \sqrt{3})R30^\circ$ periodicity with respect to the (1x1) vanadyl surface lattice. The authors have also reported that the oxygen-rich

point defects, once formed, are rather stable towards annealing in UHV. Similar observations could be made in the present study. It was not possible to reduce the quantity of these point defects by annealing the films in UHV. Also, preparing the films in a higher O_2 pressure, 5×10^{-7} mbar, led to a clear increase of the missing bright protrusions and to the appearance of $(\sqrt{3} \times \sqrt{3})R30^\circ$ patches (compare Figure 3.7 (a) with Figure 3.4 (e)). Both the (1×1) and the $(\sqrt{3} \times \sqrt{3})R30^\circ$ unit cells are indicated on Figure 3.7 (b).

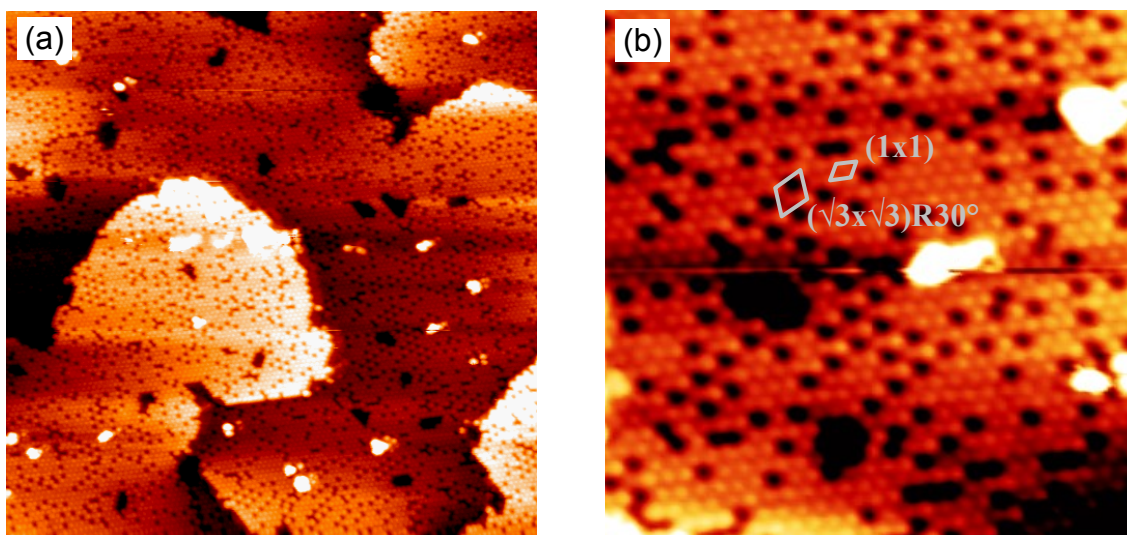


Figure 3.7. STM images ((a): 50 nm x 50 nm, 1.5 V, 0.2 nA, (b): 14 nm x 14 nm, 1.5 V, 0.2 nA) of a $V_2O_3(0001)/Au(111)$ film prepared by the evaporation of vanadium in 5×10^{-7} mbar O_2 at $300^\circ C$, followed by annealing in UHV at $600^\circ C$ for 20 min.

Various possible $V_2O_3(0001)$ surface terminations were investigated with DFT by Kresse *et al* ²⁷. These terminations include some of those mentioned in section 3.1: single metal layer, oxygen layer and vanadyl termination. As can be evaluated from the graph shown in Figure 3.8, the calculations predict that out of these three possible surface structures the vanadyl termination is the most stable in the range of oxygen chemical potential relevant for the formation of V_2O_3 . Note here that the oxygen layer termination is labeled with the stacking $..V-O_3V_3O_3$ on the graph. This is to indicate that this structure deviates from the ideal bulk-like oxygen termination depicted in Figure 3.1 (c). According to the model proposed by the authors, one half of the vanadium atoms from the second double (VV') layer would move to the first VV' layer to reduce surface energy. Kresse and coworkers also evaluated two alternative structures where either one third or two third of the $V=O$ groups are removed from the (1×1) vanadyl-terminated surface (both the V and the O atom forming the vanadyl moiety are removed). They are labeled $..V_2O_3-(VO)_{0.66}$ and $..V_2O_3-(VO)_{0.33}$ in Figure 3.8, respec-

tively. The two structures have a $(\sqrt{3}\times\sqrt{3})R30^\circ$ periodicity with respect to the (1×1) vanadyl surface lattice. In comparison to the (1×1) vanadyl termination, these surface structures effectively expose more oxygen atoms, since the oxygen plane of $V_2O_3(0001)$ is locally uncovered where the vanadyl groups are removed. They can therefore be considered as oxygen-rich surface reconstructions. Both structures are schematically described in Figure 3.9.

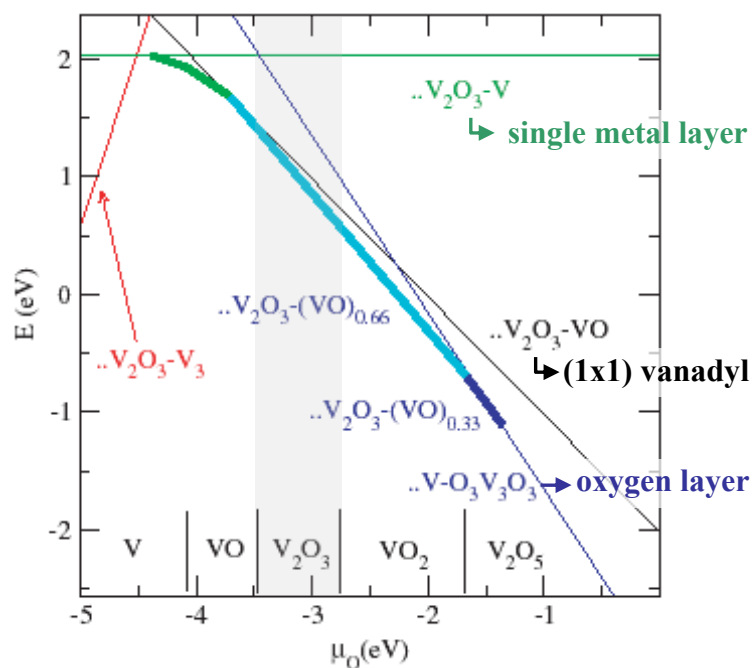


Figure 3.8. Surface energy per primitive surface cell versus chemical potential of oxygen (μ_O) for different terminations of $V_2O_3(0001)$. The stability ranges of the bulk oxides are indicated at the bottom of the diagram. Graph taken from ref. ²⁷

Coming back to the graph shown in Figure 3.8, it can be seen that the $..V_2O_3-(VO)_{0.66}$ structure is predicted to be slightly more stable than the (1×1) vanadyl termination over a broad range of oxygen chemical potential. The calculations of Todorova *et al* also predict the stability of the $..V_2O_3-(VO)_{0.66}$ structure ²⁹. The “missing bright protrusion” point defects observed in the STM images can therefore be assigned to missing $V=O$ molecules. The predicted relative stability of the $(\sqrt{3}\times\sqrt{3})R30^\circ$ reconstructions somehow explains the fact that it was not possible to prepare a (1×1) vanadyl-terminated $V_2O_3(0001)$ surface that did not contain any oxygen-rich point defects in the present study. Reducing the oxygen partial pressure below 1×10^{-7} mbar during preparation helped diminishing the density of these point defects to a limited extent. However, this parameter could only be varied in a small window since the evaporation in 5×10^{-8} mbar O_2 or less resulted in the formation of a bulk-reduced and not very well ordered film (as judged by XPS and STM), possibly due to kinetic effects.

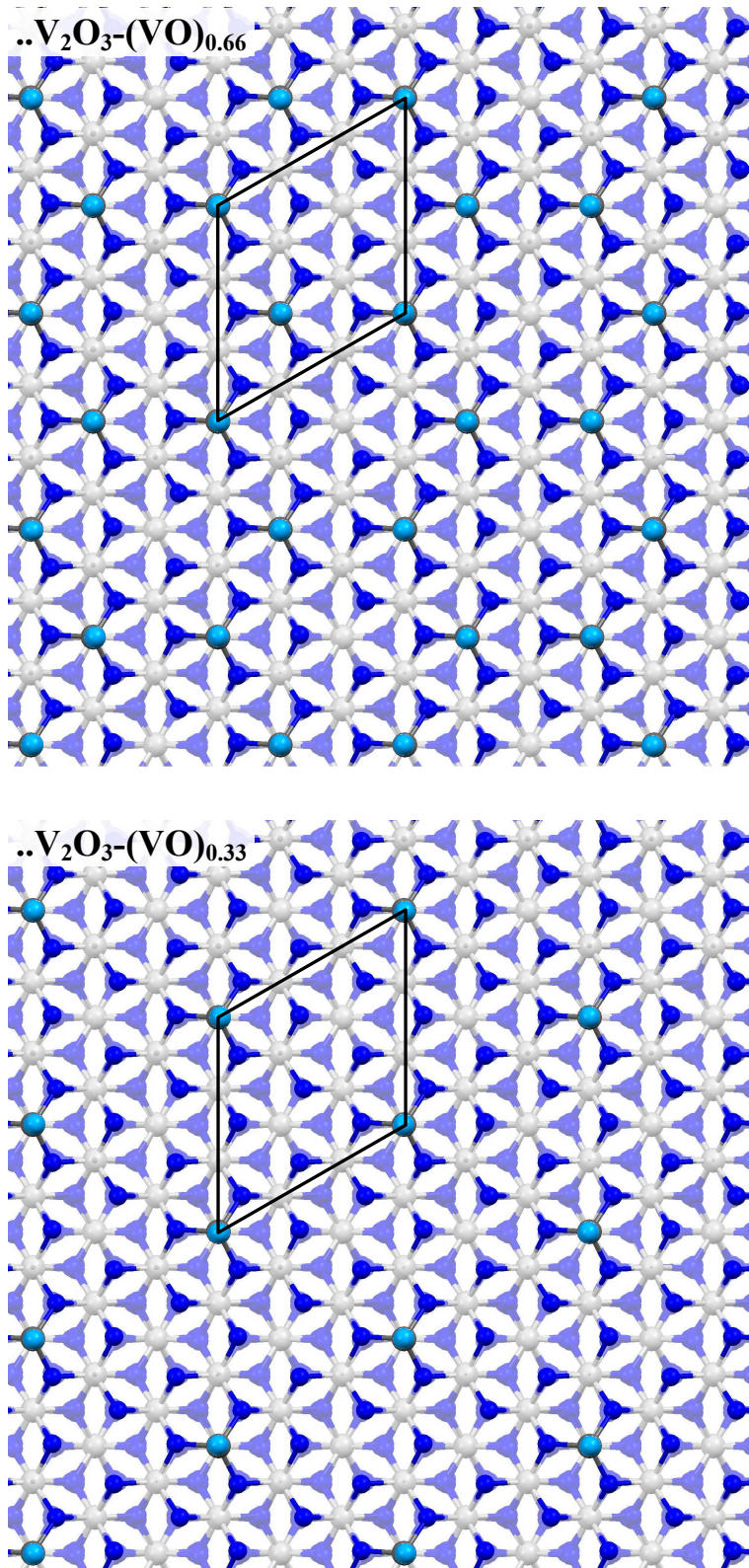


Figure 3.9. Geometric structure of the $\text{..V}_2\text{O}_3\text{-(VO)}_{0.66}$ and $\text{..V}_2\text{O}_3\text{-(VO)}_{0.33}$ $\text{V}_2\text{O}_3(0001)$ surface reconstructions. Gray spheres indicate the position of the vanadium atoms while blues spheres pertain to oxygen atoms (light blue balls highlight the position of the vanadyl oxygen atoms). The $(\sqrt{3} \times \sqrt{3})R30^\circ$ unit cell is indicated on both images.

The best results were obtained by reducing the surface of the films with electrons (see section 3.3.2) and then reoxidising it with a short exposure (1 minute) to $\sim 2 \times 10^{-8}$ mbar O_2 at 250°C . Since the reduction with electrons is limited to the very first surface layers, reoxidation can be done in milder conditions (i.e. with a lower oxygen chemical potential) than the bulk and the formation of oxygen-rich defects can be reduced. An example is given in Figure 3.10, which shows STM images obtained after reducing the film described in Figures 3.4 (c)-(f) with electrons (2×20 sec, 1 mA) and then reoxidising it by annealing at 250°C in 2×10^{-8} mbar O_2 for 1 minute. After the reduction/reoxidation procedure, the film was shortly flashed at 600°C in UHV to order the surface. Apart from the point defects described above, the STM images of the $V_2O_3(0001)/\text{Au}(111)$ films also reveal a few isolated line defects and screw dislocations. Both types of structural defects can be observed in Figure 3.10 (a), for instance. A screw dislocation can be observed in the upper part of the image, where a terrace seems to follow a spiral pattern and apparently grow on top of itself.

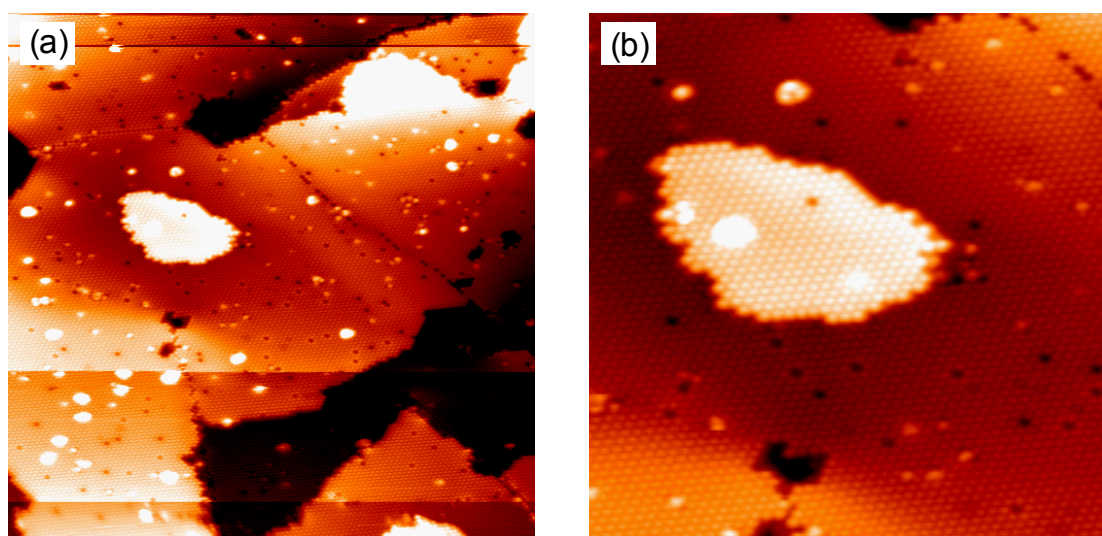


Figure 3.10. STM images ((a): 50 nm x 50 nm, -1.5 V, 0.2 nA, (b): 20 nm x 20 nm, 1.5 V, 0.2 nA) obtained on a $V_2O_3(0001)/\text{Au}(111)$ film after surface reduction with electrons and subsequent reoxidation (exposure to 2×10^{-8} mbar O_2 at 250°C for 1 minute followed by a flash at 600°C in UHV).

The results presented in this section show that well-ordered vanadyl-terminated $V_2O_3(0001)$ films can be grown on $\text{Au}(111)$. Their surface contains stable oxygen-rich point defects (missing $\text{V}=\text{O}$ molecules) that are related to the $(\sqrt{3} \times \sqrt{3})R30^\circ$ structures reported by other authors^{27,28}. Nevertheless, the density of these point defects can be limited by careful surface treatment, involving reduction with electrons and controlled reoxidation.

3.3.2 Surface reduction with electrons: formation of a V-termination

The surface reduction of the films was investigated as a function of the applied electron dose with STM and XPS. Before each reduction experiment, the (1x1) vanadyl terminated surface was carefully prepared and STM was used to ascertain a small quantity of oxygen-rich point defects. Representative STM and XPS results are shown in Figures 3.11 and 3.12, respectively. The high resolution STM images show that a number of missing bright protrusions appear after the shortest irradiation periods. Since great care was taken to limit the quantity of oxygen-rich point defects before the electron irradiation, most of the missing bright protrusions observed here can be related to the reduction process. Concomitant with the appearance of these new point defects, the surface sensitive XPS spectrum (electron collection angle of 70° with respect to the surface normal) acquired after an irradiation of 1 second shows a slight decrease of the O1s intensity and shift of the V2p peaks towards lower binding energy. This is consistent with a removal of oxygen atoms from the surface of the film. The quantity of missing bright protrusions obviously increases with the electron dose (i.e. with the irradiation time) and after an irradiation of 10-20 s the surface looks somewhat disordered. However, closer inspection reveals that the remaining bright protrusions are still positioned according to the original hexagonal registry of the non-reduced surface. Upon further increase of the electron dose, an ordered surface structure with a 4.9 Å hexagonal unit cell is obtained (see image obtained after 2 cycles of 20 s irradiation). This surface periodicity is equivalent to the one observed on the (1x1) vanadyl-terminated surface. Comparing the two (1x1) surfaces, the STM corrugation is clearly and reproducibly lower in the case of the reduced surface. The XPS signals follow the progression observed with STM. As the electron dose is increased, the O1s intensity continuously decreases and the V2p features are shifted towards lower binding energy. The overall shape of the V2p peaks is also slightly modified, as the intensity of the high binding energy shoulder vanishes and a new component at lower binding energy seems to appear. Scanning tunneling spectroscopy (STS) was carried-out on both the vanadyl-terminated and the reduced (1x1) surfaces. In the two cases, dI/dV curves were obtained at numerous places on the surface and averaged together to ensure reproducibility. The results, shown in Figure 3.13, confirm the different electronic structure between the two surfaces. The curves obtained for the reduced surface point towards a lower density of empty states (positive sample bias) and a higher density of filled states (presumably of V3d character, around 0.5 eV below the Fermi level).

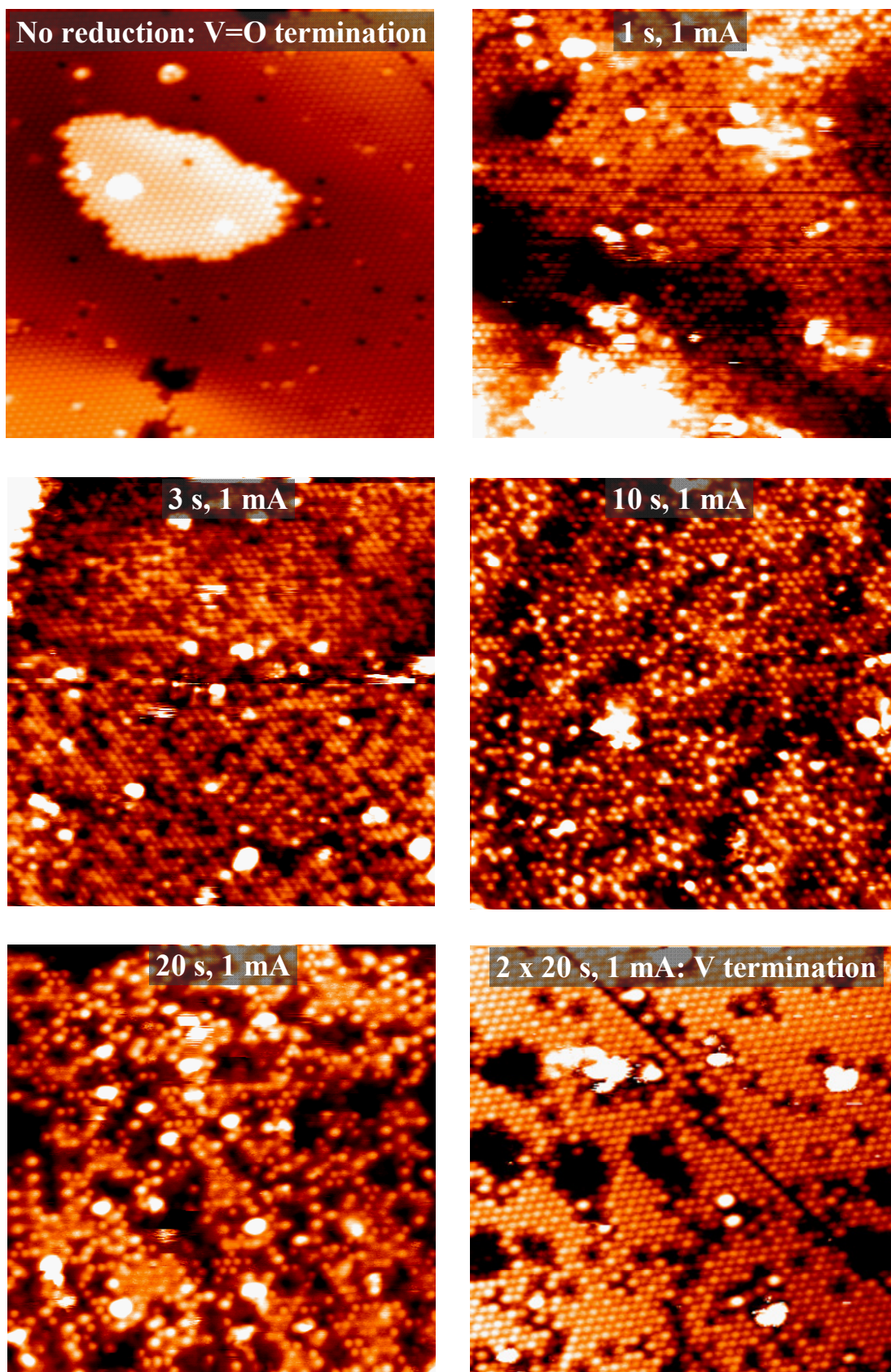


Figure 3.11. STM images of a $V_2O_3(0001)/Au(111)$ film exposed to various electron irradiation doses. All images: 20 nm x 20 nm, 1.5 V, 0.2 nA.

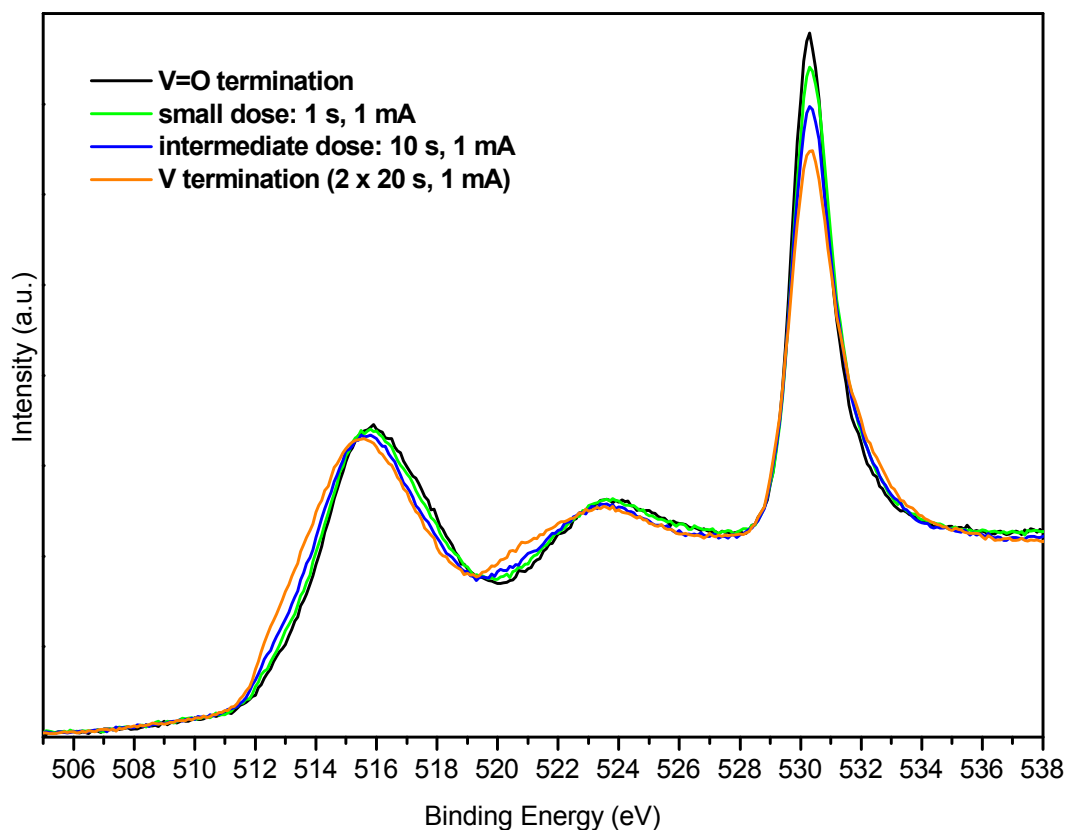


Figure 3.12. XPS spectra (V2p and O1s region) of a $V_2O_3(0001)/Au(111)$ film exposed to various electron irradiation doses. The intensity was normalized to the background signal at 500 eV. Mg $K\alpha$, $\theta = 70^\circ$.

Altogether, these observations are consistent with a gradual removal of the vanadyl oxygen atoms from the surface during the reduction with electrons (as also revealed by vibrational spectroscopy measurements²⁶). The geometric models shown in Figure 3.14 illustrate the progression of this reduction process. In the course of the irradiation, vanadyl oxygen atoms are gradually removed from the surface and the reduced V ions left behind appear as missing bright protrusions in the STM images. It is important to distinguish these missing bright protrusion from the ones pertaining to oxygen-rich point defects described in section 3.3.1: the latter are caused by the removal of a whole V=O molecule. The removal of vanadyl O during the electron irradiation seems to occur in a more or less random manner on the surface. Nevertheless, some missing bright protrusion pairs or short rows are observed at the beginning of the reduction process (see images obtained after 1 s and 3 s of irradiation). This could imply that the vanadyl groups neighboring a reduced V atom are more prone to reduction (due to relaxation effects like in the case of $V_2O_5(001)$, see Chapter 5). However,

based on the theoretical investigations of Todorova *et al*, such a concerted reduction mechanism appears to be very unlikely²⁹.

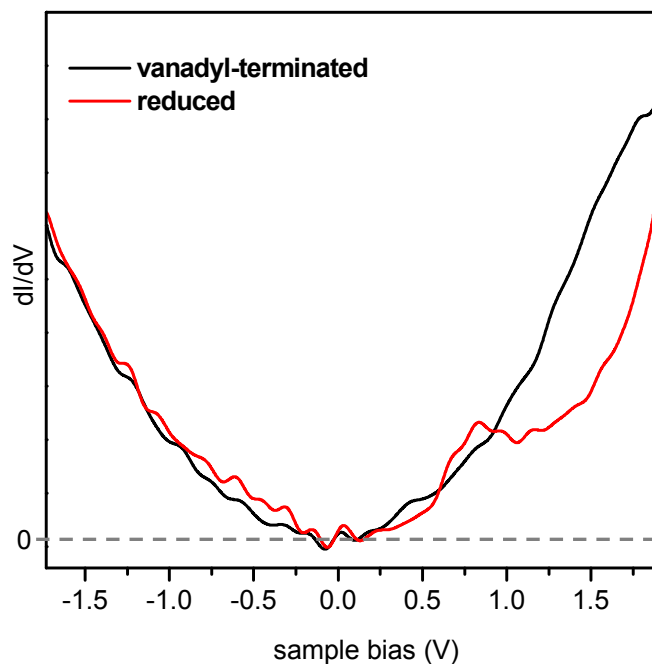


Figure 3.13. STS dI/dV curves compared for the (1x1) vanadyl terminated and the (1x1) reduced surfaces of $V_2O_3(0001)/Au(111)$ thin films. Reduced surface exposed to two electron irradiation cycles of 20 s at 1 mA.

The complete removal of the vanadyl oxygen atoms ultimately results in the formation of a V-terminated surface, which obviously has the same lattice as the vanadyl-terminated surface. Note that the precise structure of this surface might differ slightly from the ideal bulk-like V-termination depicted in Figure 3.1 (b). The calculations of Czekaj and coworkers indeed predict that the topmost V layer relaxes inwards by about 30% for this surface (in addition to some rearrangement of sub-surface vanadium)⁵⁵.

At intermediate irradiation doses, only a fraction of the vanadyl oxygen atoms is removed. In this range, the quantity of remaining bright protrusions observed in the STM images is seen to decrease for an increasing degree of reduction. The positions of the bright protrusions are therefore assigned to the remaining V=O groups.

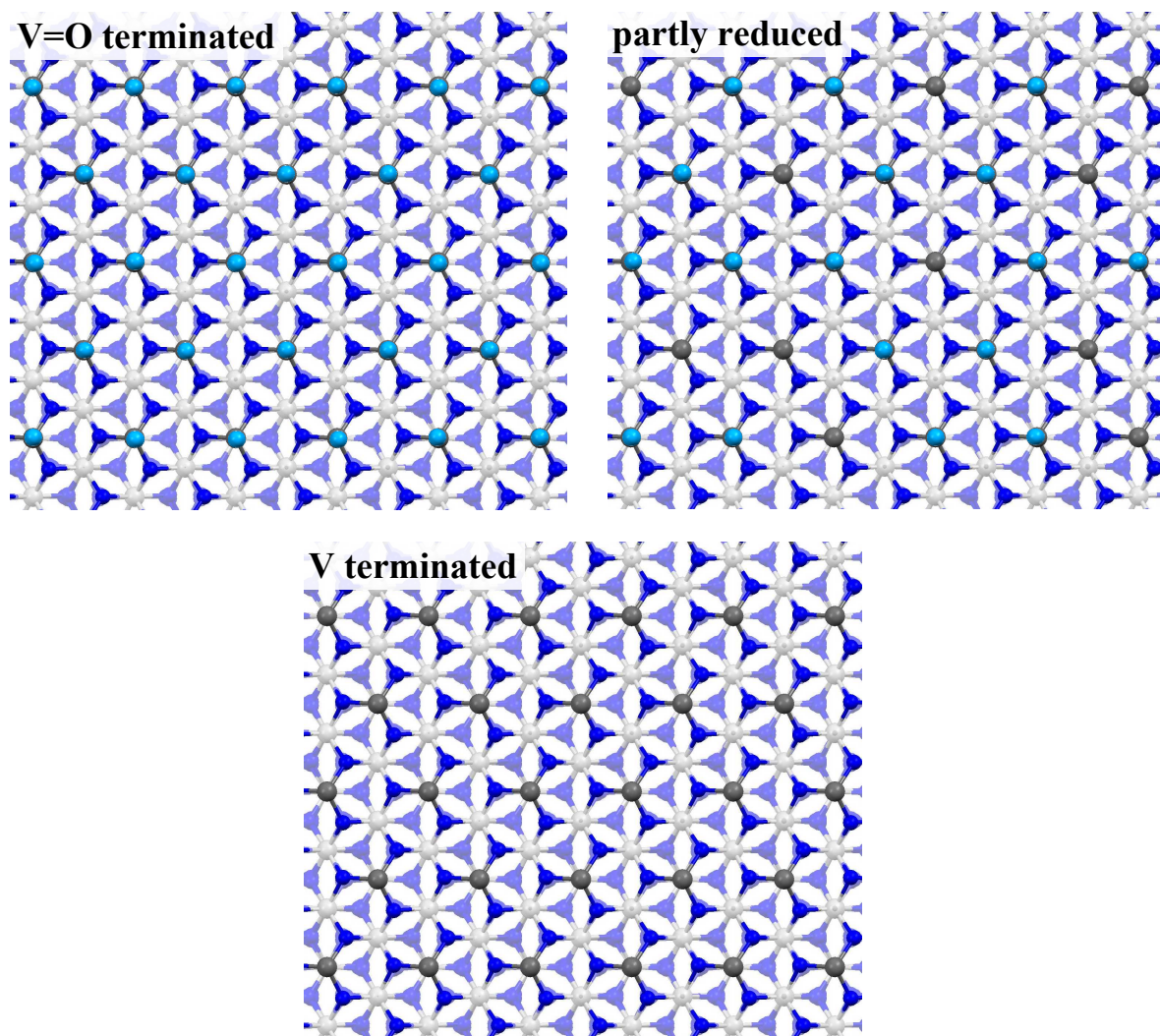


Figure 3.14. $V_2O_3(0001)$ reduction with electron irradiation: geometric structure of the vanadyl terminated, partly reduced and fully reduced (V-terminated) surfaces. Gray and blues spheres indicate the position of the vanadium and oxygen atoms, respectively (light blue balls: vanadyl oxygen atoms).

The data presented in this section indicate that the reduction of $V_2O_3(0001)$ with 500 eV electrons is mostly limited to the surface vanadyl groups. This conclusion is further supported by the fact that XPS spectra and STM images do not change as a function of the electron dose once all the V=O groups have been removed (at least for up to twice the dose required for a complete V=O removal). Of course, this does not necessarily mean that further reduction can not occur after prolonged electron irradiation. It probably occurs, but much more slowly. Vanadyl oxygen atoms at the surface are directly exposed to the vacuum and can readily move away if the V=O bond is broken, in contrast the O atoms from deeper layers that must first diffuse to the surface. Other possible factors include the lower V coordination and the different density of electronic states involved for the surface vanadyl O centers. Nevertheless, the

appearance of a shoulder at the lower binding energy side of the XPS V2p peaks after surface reduction could in principle be interpreted as an indication of the presence of vanadium ions that have a lower oxidation state than the bulk V ions of V_2O_3 . However, this does not necessarily mean that extensive reduction occurs. The DFT cluster calculations of Czekaj *et al* for V-terminated $V_2O_3(0001)$ clearly indicate that the surface V centers have a lower atomic charge than in the bulk⁴⁶. Based on Mulliken population analysis, the authors reported an atomic charge of ~ 0.7 for the terminating 3-fold coordinated V ions, in contrast to an atomic charge between 1.6 and 2 for the bulk 6-fold coordinated V centers. It is therefore possible that the core level photoelectron signals associated with the surface V centers are slightly shifted towards lower binding energy in comparison with the bulk signals for V-terminated $V_2O_3(0001)$.

The electron-induced surface reduction process observed here can be described on the basis of electron-stimulated desorption (ESD) theory (see chapter 5 of ref.³⁴ and refs.^{59,60}, for instance). ESD differs from thermal desorption in several important ways, the most obvious being the fact that ESD is a process occurring far from equilibrium. It is generally considered that the energy transfer between an electron and an adspecies (surface atom or molecule) occurs as an isolated event. This is due to the fact that the probability of a surface atom interacting simultaneously with more than one primary electron is small. It is also well accepted that the direct momentum transfer between a low energy electron and a surface specie is far too small to account for the observed desorption and does not play a significant role. ESD is rather based on electronic excitation and bond breaking mechanisms. Electronic energy transfer processes that can lead to desorption of surface species include the excitation of ground states into antibonding or nonbonding states (Menzel-Gomer-Redhead model, MGR) and the generation of core holes followed by Auger decay⁶¹. A very simplified scheme of the MGR model is depicted in Figure 3.15 (a). As a starting point, the model assumes that an incident electron initiates a Frank–Condon transition which takes the adspecies-solid system from a ground state to an electronically excited state or ionic state. The interaction energy curve of the excited state specie may be very different from that of the ground state neutral specie. The excited state may have a shallow attractive potential well or no attractive region at all. After the excitation process, the system will relax by the excited adspecies moving away from the surface. The reduction of the system potential energy imparts equivalent kinetic energy to the desorbing specie.

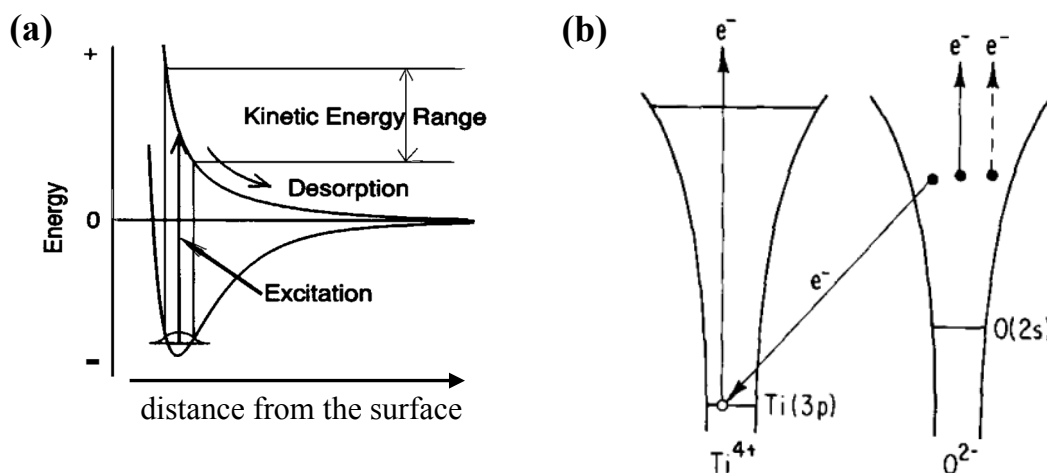


Figure 3.15. Schematic description of electron stimulated desorption (ESD) models: (a) MGR, (b) Knotek-Feibelman.^{34,60,62}

The exact surface reduction mechanism (s) involved here for the vanadyl-terminated $V_2O_3(0001)$ surface can not be identified with certainty at the moment. Nevertheless, it is worth pointing out that the role of core hole formation has been shown to play a key role for several oxide systems. For instance, Knotek and Feibelman have shown that the threshold energy for the electron-stimulated oxygen desorption from TiO_2 , WO_3 and V_2O_5 corresponds to the excitation energy of the metal ions 3p core holes (about 38 eV for V3p)⁶². In comparison, valence electron bonding-antibonding transitions described by the MGR model occur at much lower energy for the three oxides (below 20 eV). The mechanism connecting the formation of the core holes at the metal centers with oxygen desorption is still not clearly determined. Knotek and Feibelman initially proposed the occurrence of an inter-atomic Auger relaxation process where the metal core hole gets filled with an electron from a ligand O2p orbital: if the two electrons necessary for the Auger decay come from a surface O, this atom will become formally electrically neutral and easy to desorb (this is described in Figure 3.15 (b) for TiO_2 ⁶²). Nevertheless, to be valid this model must consider an empty metal 3d band; otherwise, the occurrence of a much faster intra-atomic Auger decay would most probably prevail⁶². This is not necessarily a valid assumption since the oxides considered by the model all have a non-negligible degree of covalency and some level of 3d occupation⁶³. As recently pointed out by Dulub *et al*, a multihole final state of the O ligand following the formation of a metal core hole is actually quite probable for early transition metal oxides even if Auger de-excitation is disregarded⁶⁴. This observation is based on the cluster model core-hole excitations calculations reported by Zimmermann and coworkers, which point towards a significant charge transfer from the ligand orbitals to the 3d electron shell on the metal atom for the core

hole photoemission final states of various transition metal oxides (including V_2O_5 and V_2O_3)⁶³. In a simple physical picture, the creation of a core hole at the metal center pulls the 3d band down in energy and electrons flow from the oxygen ligand to the metal. The formation of V3p core holes probably also plays an important role in the electron-induced removal of surface vanadyl oxygen atoms observed in the present study.

3.3.3 Thermal stability of V-terminated $V_2O_3(0001)$

The V-terminated surface has been predicted to be thermodynamically unstable, even under strongly reducing conditions (see Figure 3.8)²⁷. Actually, such a surface could not be prepared in other reported $V_2O_3(0001)$ surface reduction experiments. Schoiswohl *et al* have reduced the film surface by depositing an additional layer of metallic vanadium²⁸. The resulting surface structure was disordered after V evaporation at room temperature, and two different types of surface reconstruction were obtained after annealing (see below). The fact that an energetically unfavorable structure could be obtained here highlights the strong non-equilibrium character of ESD processes. The reduced surfaces (both fully and partly reduced) obtained in the present experiments appear to be only kinetically stabilized since they reconstruct upon annealing in UHV. Nevertheless, they are stable up to about 300°C. They are first observed to undergo reconstruction after annealing at 350°C - 400°C in UHV. The reconstructed surfaces show the coexistence of two different structures. The relative area covered by both structures apparently varies as a function of the initial reduction degree (i.e. partial reduction with a fraction of remaining V=O groups or V termination). An example of such a reconstructed surface is depicted in Figure 3.16, where STM images are shown for a partially reduced surface (15 s, 1 mA irradiation) shortly annealed at 400°C in UHV. The corresponding XPS spectra obtained before and after the annealing step are shown in Figure 3.17. The large scale STM images of the reconstructed surface (Figure 3.16 (a)) display flat patches along with terrace areas having a “fuzzy” appearance. Images taken at higher resolution are shown in Figures 3.16 (b)-(d). They reveal that the fuzzy areas are covered by “trimers” (bright triangular features in which three maxima can be resolved). The trimers are not arranged very regularly on the surface and it seems that some remainders of the (1x1) surface structure can be imaged between them. On the other hand, the flat areas exhibit a well ordered hexagonal structure with a $\sim 5 \text{ \AA}$ unit cell vector, where the bright protrusions appear to be elongated in one direction. These areas are also characterized by a very low corrugation, which generally could imply a metal-like surface layer. As shown in Figure 3.18, their dI/dV curve also differentiates them from both hexagonal (1x1) vanadyl- or V-terminated surfaces.

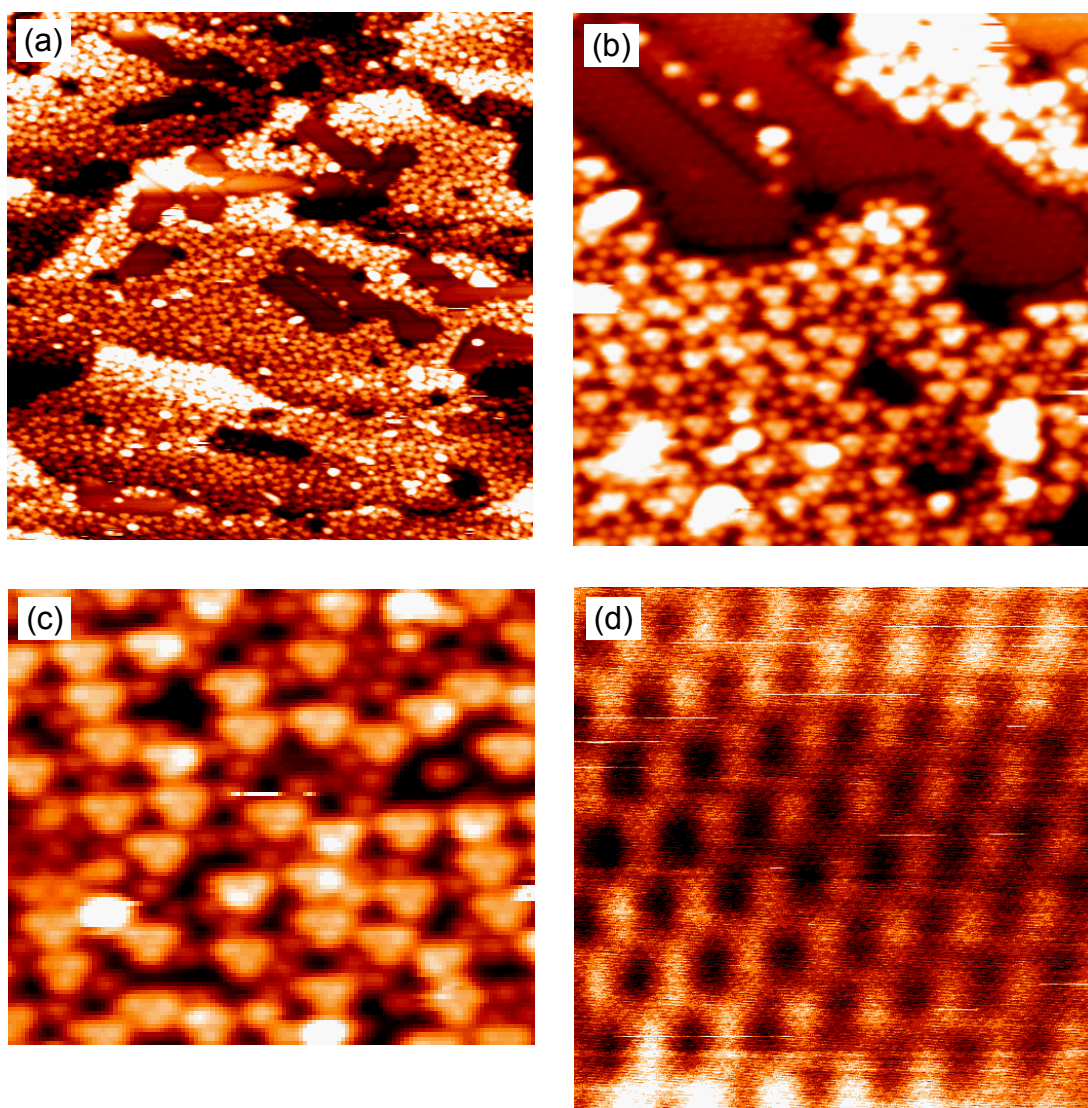


Figure 3.16. STM images of a $V_2O_3(0001)/Au(111)$ film reduced by electron irradiation (15 s, 1 mA) and then flashed at $400^\circ C$ in UHV. (a): 50 nm x 50 nm, -2 V, 0.2 nA, (b): 15 nm x 15 nm, -1.5 V, 0.2 nA, (c): 7.3 nm x 6.3 nm, -1.5 V, 0.2 nA, (d): 3.5 nm x 3.5 nm, -1.5 V, 0.2 nA. Image (d) was acquired in one of the low corrugation areas of (a).

The two reconstructed structures have been observed by Schoiswohl *et al*²⁸. The authors have reduced the vanadyl terminated $V_2O_3(0001)$ surface by depositing an extra layer of metallic vanadium. Following the deposition, they had to shortly anneal the sample at $450^\circ C$ in UHV to induce ordering in the overlayer. Similar to our findings, the resulting surface exposed a mixture of both “fuzzy” (trimers-covered) and “flat” (low corrugation) areas. Structures were proposed by the authors for the two different surface features. The trimers were assigned to a structure formed by a triangle of oxygen atoms with a vanadium atom in its center. The hexagonal, low corrugation areas were attributed to a buckled V_3 termination layer, i.e. a $\dots V_2O_3V_3$ surface stacking. At this surface, the vanadium ions have a quasi-hexagonal arrangement and the average V-V distance is about 2.8 Å. However, buckling in the layer

results in a 4.9 Å hexagonal unit cell. Note that this structure was evaluated by DFT and was found to be thermodynamically unstable²⁷. Obviously, the structures of the two reconstruction features (trimers and low corrugation surface) are not clarified yet and more extensive investigations, both experimental and theoretical, would be required.

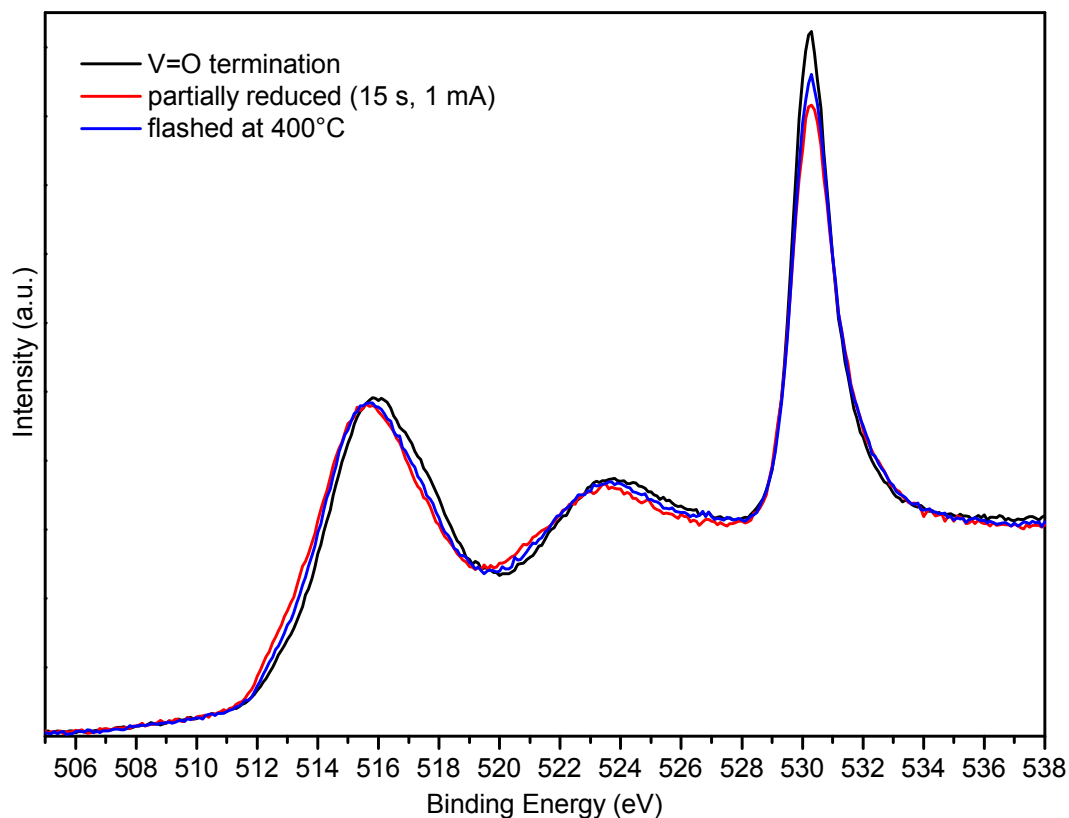


Figure 3.17. XPS spectra (V2p and O1s region) of a $V_2O_3(0001)/Au(111)$ film reduced with electrons (15 s, 1 mA) and then flashed at 400°C in UHV. The spectrum corresponding to the initial vanadyl-terminated surface is also shown for comparison. The intensity was normalized to the background signal at 500 eV. Mg $K\alpha$, $\theta = 70^\circ$.

The XPS spectra shown in Figure 3.17 reveal a slight increase of the O1s intensity and a very small shift of the V2p peaks towards higher binding energy for the reconstructed surface (in comparison to the reduced surface). This possibly indicates that the reconstruction of the reduced surfaces occurring at 400°C in UHV is accompanied by the diffusion of oxygen from the bulk of the film to the surface. The same surface was subsequently annealed at 600°C in UHV. This led to a recovery of the vanadyl terminated (1x1) surface. Further experiments however revealed that it is not possible to carry-out more than 1-2 cycles of electron reduction and UHV annealing at 600°C and still retrieve the vanadyl termination. Therefore, it appears

that the bulk of the film can act as an oxygen reservoir, which can perhaps be more or less filled depending on the preparation conditions, and can be depleted after some electron reduction/UHV annealing cycles. This effect should be taken in consideration for experiments where the reactivity of the reduced surfaces at temperatures above 400°C is considered.

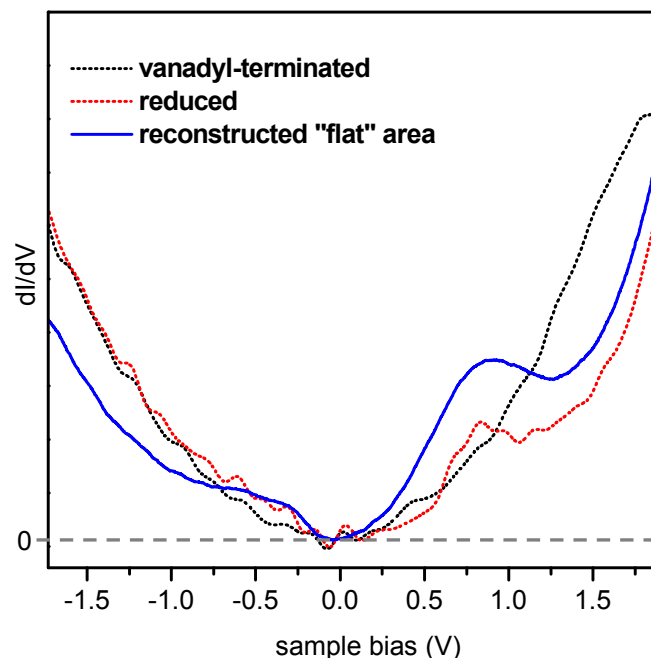


Figure 3.18. STS dI/dV curves: low corrugation structure obtained after the reconstruction of a reduced $V_2O_3(0001)$ surface compared to both (1×1) vanadyl terminated and (1×1) V-terminated surfaces.

3.4 Summary

Well-ordered $V_2O_3(0001)$ thin films can be prepared on Au(111) by reactive evaporation of vanadium in an oxygen partial pressure followed by annealing in vacuum. All the films were shown to invariably contain a certain quantity of oxygen-rich point defects, which is to be expected in view of the predicted thermodynamic stability of these structures. The quantity of the oxygen-rich point defects can however be controlled to some extent by surface preparation involving reduction with electrons and careful reoxidation.

The irradiation of the films with 500 eV electrons results in the removal of the vanadyl oxygen atoms and in the formation of a V-terminated surface. The results support the assumption that the reduction is limited to the vanadyl groups and does not significantly take place in the subsurface layers or in the bulk (within the electron doses investigated here). The V-terminated surface is actually a thermodynamically unfavorable structure which could only be

obtained by ESD, a process allowing surface reduction in non-equilibrium conditions. UHV annealing of the reduced films at 400°C results in a surface reconstruction, which consists of two different types of structures. By using an appropriate electron irradiation dose, only a fraction of the vanadyl groups can be removed. Such a surface exposes both vanadyl groups and 3-fold coordinated V ions.

It is of great interest to be able to selectively and quantitatively remove the vanadyl groups at the surface of $V_2O_3(0001)$, as this allows probing the role of the vanadyl groups in the surface adsorption/reaction mechanisms involved in vanadium-oxide based catalysis. Based on the results obtained in the present study, the adsorption of methanol on $V_2O_3(0001)$ was studied as a function of the surface reduction degree⁵⁸. It could be shown that the concentration of vanadyl groups controls the selectivity of the methanol oxy-dehydrogenation towards formaldehyde.

4 Growth of V₂O₅ thin films

4.1 Introduction

Well ordered V₂O₅ thin films of various thicknesses were obtained by the oxidation of vanadium on Au(111) using the high pressure cell described in section 2.1.3. They are described in this chapter. Generally, the growth of V₂O₅ thin films using various methods has already been reported in the literature. These methods include flash-evaporation of V₂O₅^{65,66}, pulsed-laser deposition⁶⁷, magnetron sputtering^{68,69}, chemical vapor deposition⁷⁰ and spray pyrolysis⁷¹. However, in many of these cases sub-stoichiometric films (i.e. containing some V⁴⁺ species) were obtained. Several films were also amorphous or polycrystalline at best. More generally, the growth of well-ordered, flat V₂O₅ films suitable for reactivity model studies has not been reported yet. In the present work, the oxidation of physical vapor deposited (PVD) V layers with O₂ was used as a relatively simple and cheap method to grow V₂O₅ films in a well controlled manner. Vanadium pentoxide is the oxide with the highest vanadium oxidation state (formally V⁵⁺) in the vanadium-oxygen system and the oxidation of V to V₂O₅ requires O₂ pressures that are not suitable for ultra high vacuum (UHV) systems (probably due to kinetic effects). This has been evidenced by several studies, where it was shown that the preparation of films by reactive evaporation or post-deposition oxidation of V under oxygen pressures in the 10⁻⁷-10⁻⁶ mbar range results in the formation of oxides having a V³⁺ or V⁴⁺ oxidation state (see^{26,28,72-75}, for instance). Wong *et al* investigated the formation of ultra-thin (~ monolayer) oxide films by oxidation of vapor-deposited V in 10⁻³ mbar O₂⁷⁶. They reported that the resulting films contained primarily V⁵⁺ ions, but also a fraction of V⁴⁺ species. To circumvent this limitation, a dedicated high pressure cell was used in this study to carry “*in situ*” (i.e. without exposure to ambient atmosphere) the oxidation of V in 50 mbar O₂.

V₂O₅ has an orthorhombic structure consisting of layers parallel to (001)^{2,77,78}. The unit cell parameters are $a = 11.512$, $b = 3.564$ and $c = 4.368$ Å⁷⁸. The crystalline structure of V₂O₅ projected along [010] is depicted in Figure 4.1. The V coordination is best described as distorted square pyramidal and the layers are composed of VO₅ units that are sharing edges or corners in the (001) plane. The structure contains three structurally different oxygen centers and these are labeled in Figure 4.1 (b): terminal oxygen coordinated to only one vanadium atom (*O(1)*) and bridging oxygen coordinated to two (*O(2)*) or three (*O(3)*) vanadium atoms. For each square pyramid, the apical oxygen atom (terminal, *O(1)*) forms a double bond with

the V atom, and these vanadyl groups (V=O) are oriented along [001] in alternating directions towards one of the next neighboring layers. The layers are considered to be held together by van der Waals V=O \cdots V interactions and (001) is the easiest cleavage plane of V₂O₅^{1,2}.

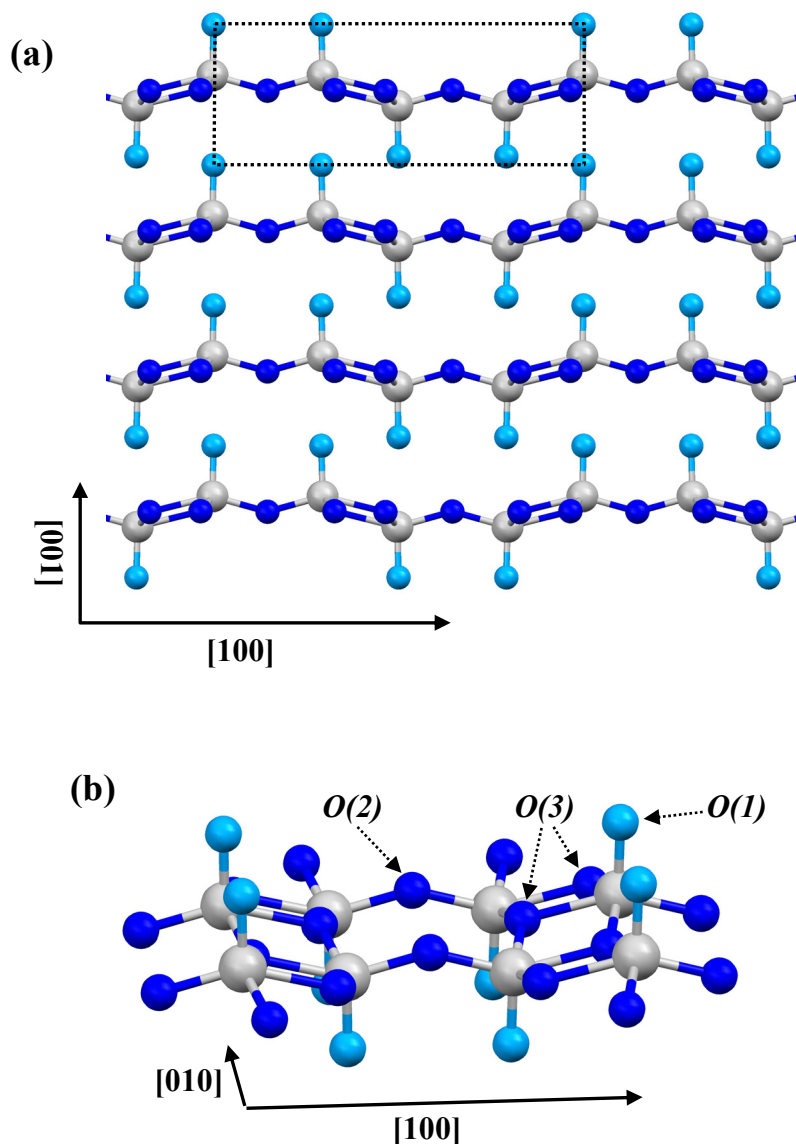


Figure 4.1. V₂O₅ geometric structure⁷⁸. (a): view of the structure along [010] showing the stacking of the layers in the [001] direction. (b): magnified and tilted view showing the structural details in a layer. Gray spheres indicate the position of the vanadium atoms while blues spheres pertain to oxygen atoms (the light blue indicating vanadyl O atoms). The elementary unit cell is shown in (a) and the non-equivalent oxygen centers, *O*(1, 2, 3), are labeled accordingly in (b).

The use of Au(111) as a substrate for the growth of V₂O₅ films might appear at first as an intriguing choice since there is no epitaxial match between this surface and any of the V₂O₅ crystalline planes. However, no other single crystalline substrate that would provide an

adequate epitaxial relation was found. The reasons that motivated the use of Au(111) as a substrate are its relative easy preparation and its inertness towards mbar pressures of oxygen (other metal surfaces could oxidize, reconstruct and form facets, etc).

4.2 Preparation Method

The films were grown by first evaporating a given quantity of metallic vanadium onto Au(111) in UHV and then transferring the sample into the high pressure cell to carry out the oxidation procedure. Vanadium was evaporated with an Omicron EFM3 electron beam evaporator while the Au(111) substrate was kept at room temperature. Different V amounts were deposited in order to vary the thickness of the resulting oxide films. The evaporation rate was calibrated in-situ with a quartz crystal microbalance (in both UHV systems) and with STM images taken after evaporation. The evaporation rate was typically $\sim 0.4 \text{ \AA}/\text{min}$ ($0.2 \text{ MLE}/\text{min}$). The deposited V thicknesses are reported here in monolayer equivalent (MLE), where 1 MLE contains the same number of V atoms as one layer of Au(111) ($\sim 1.39 \times 10^{15} \text{ atoms}/\text{cm}^2$). After the V evaporation, the sample was moved to the high pressure cell heating stage. The cell was then isolated from the rest of the UHV system and filled with 50 mbar of oxygen (99.999% purity, Linde). While maintaining the pressure constant, an O_2 flow was established in order to avoid a pile-up of contaminations originating from molecules desorbing from the heated surfaces. The sample was heated at 400°C for 10 minutes. The temperature was then allowed to cool-down to about 100°C before pumping down the high pressure cell and transferring the sample back to the main chamber. Initial XPS experiments on thicker V films indicated that these oxidation conditions (pressure, temperature and time) are sufficient to reach the full V^{5+} oxidation state. After oxidation of the films, no traces of surface contamination could be detected with XPS.

4.3 Results and discussion

Different surface structures were observed as a function of the thin film thickness. The oxidation of very low V amounts led to the formation of well-ordered overlayers with structures that do not correspond to any known bulk vanadium oxide crystal structures. The characterization of these “interface specific” layers is first described and discussed. This is followed by the description of the films formed at higher V thicknesses, which consist of $V_2O_5(001)$. The structure and the composition of the films have been investigated with STM, LEED, photoelectron spectroscopy and NEXAFS. In order to minimize the influence of X-ray or e-beam induced reduction processes, the films were always first probed with STM. The thermal stability of the films under UHV has been investigated with TDP and XPS, and the results are presented in section 4.3.3.

4.3.1 Structure of the first layers

Figure 4.2 (a) shows a $100 \times 100 \text{ nm}^2$ STM image obtained after the deposition of about 0.26 MLE V on Au(111) at room temperature. V islands periodically arranged in lines spaced by about 14 nm are seen on the surface. The spacing between the islands along the lines is on the average 7.2-7.5 nm. This arrangement corresponds to the periodicity of the well-known Au(111) herringbone reconstruction superlattice³². In the central part of the image, where the signal has been differentiated to enhance the contrast, one can indeed observe that the growing V islands mainly nucleate on the elbows of the herringbone reconstruction. These sites are situated at the boundary between two alternating domains of uniaxial contraction having a relative orientation of 120° . Within the domains, dislocation lines (seen as ridges in STM) arise from stacking transitions of the Au atoms induced by the contraction. The herringbone elbows are expected to be the most reactive sites at the surface of reconstructed Au(111) and the preferential nucleation of metals at these features was also previously reported for Ni and Mo, for instance⁷⁹⁻⁸¹. Although it is known that V and Au can form bulk alloys⁸², no evidence such as the appearance of serrated steps point towards surface alloying for the deposition conditions used here. Indeed, the Au(111) terraces are still well-ordered after the deposition and large scale STM images (not shown) reveal that the Au(111) step edges remain straight and regular.

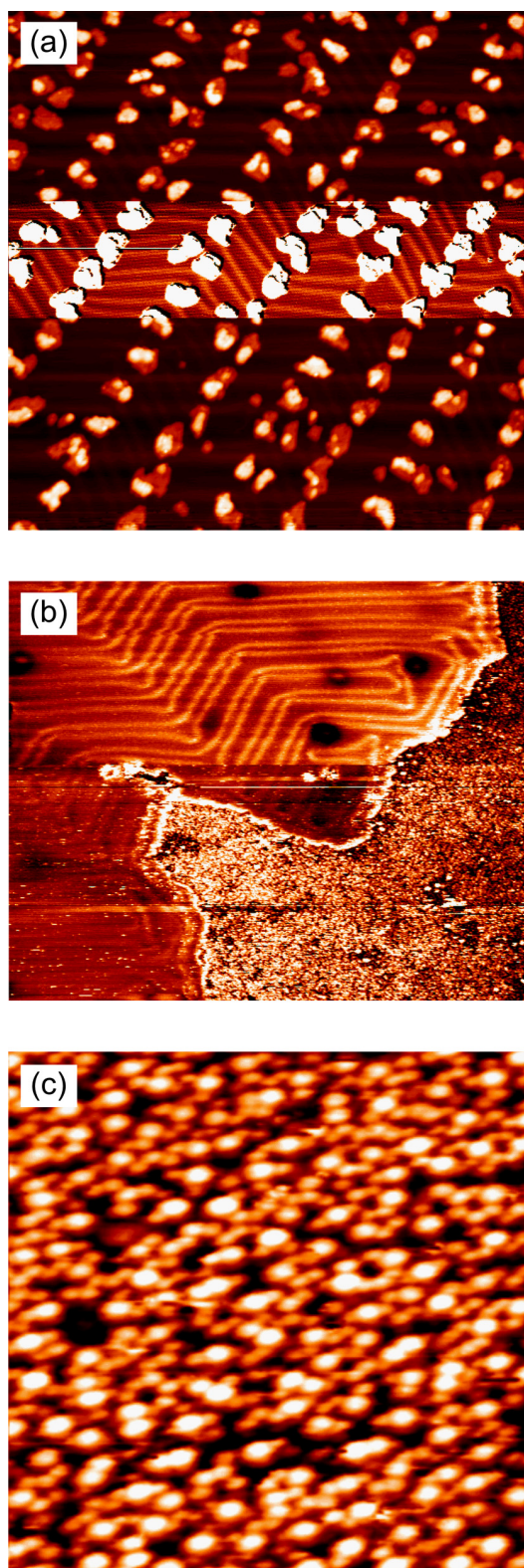


Figure 4.2. STM images of 0.26 MLE V/Au(111): (a) as deposited at room temperature (100 nm x 100 nm, 0.5 V, 1 nA; middle part of the image differentiated) and (b, c) after annealing in 50 mbar O₂ at 400°C for 10 minutes ((b): 100 nm x 83.6 nm, 2 V, 0.2 nA, (c): 10 nm x 10 nm, 1.5 V, 0.2 nA).

After the oxidation of the 0.26 MLE V/Au(111) film at 400°C, a disordered oxide monolayer covers a fraction of the substrate surface, as shown in Figure 4.2 (b). During the oxidation, it appears that 2D mass transport of VO_x species occurs on the surface of Au(111) and extended oxide monolayer patches grow. This is in contrast to a situation where oxide islands would form at the initial position of the V clusters and remain on the elbows of the herringbone reconstruction.

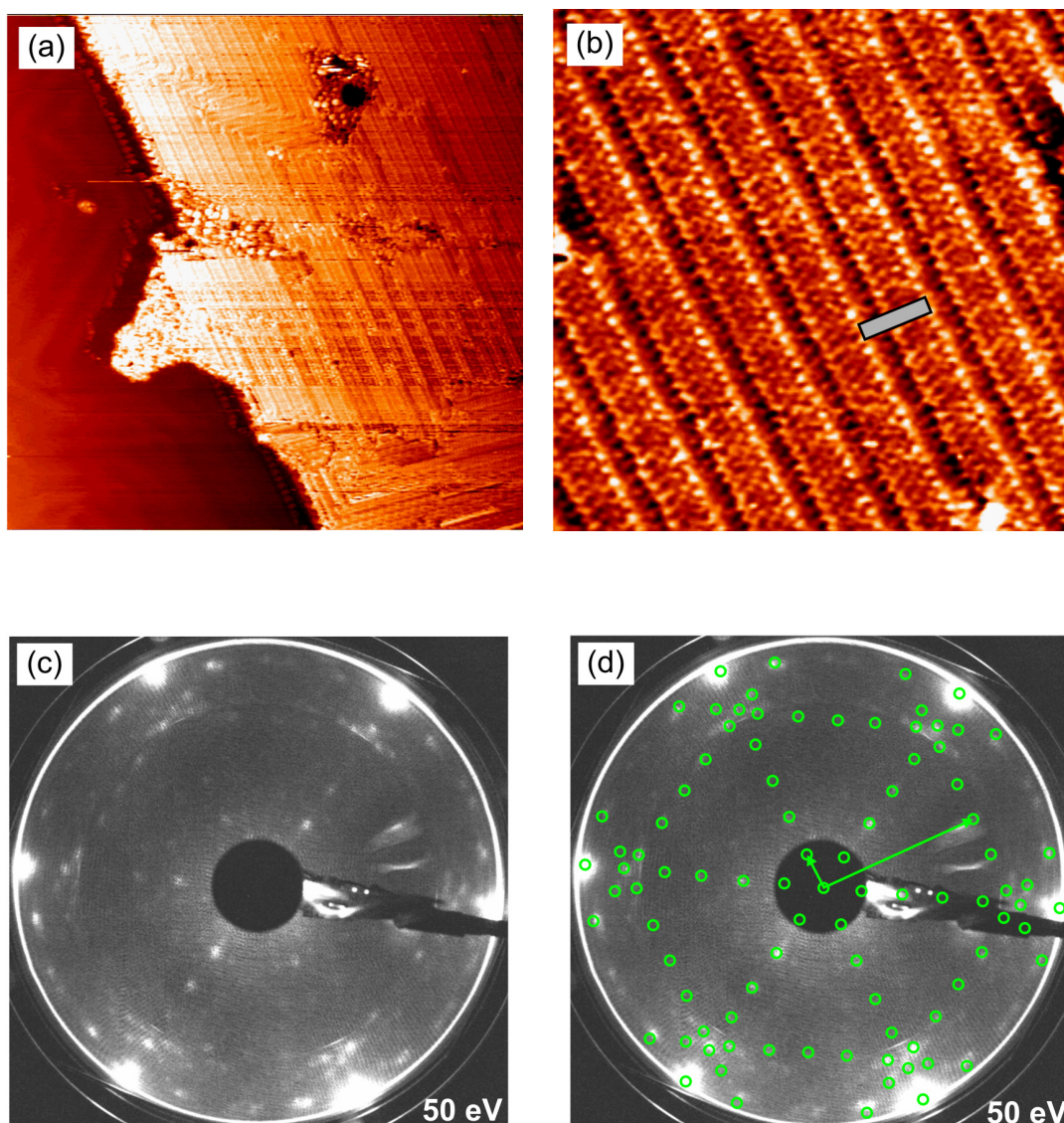


Figure 4.3. STM images ((a): 50 nm x 50 nm, 2.5 V, 0.2 nA, (b): 10 nm x 10 nm, 2.5 V, 0.2 nA) and LEED pattern (c) obtained after annealing a film formed by the oxidation of 0.26 MLE V/Au(111) (see Figure 4.2). (d): Reproduction of the LEED pattern using a 3.6 Å x 15 Å rectangular unit cell and taking into account the substrate 3-fold symmetry (the bright spots at the border of the screen are the Au(111) (10) spots).

Closer inspection of the oxide film's structure (Figure 4.2 (c)) allows the identification of several features, such as rings, zigzags and brighter protrusions. However, it is obvious that the film has no long range order. This is supported by LEED results (not shown), where mainly the Au(111) spots are observed, along with some background intensity and very weak and diffuse spots. Subsequent annealing in UHV was necessary to order the film. Figure 4.3 displays STM images and a LEED pattern obtained after annealing the film at 200°C for 5 min in UHV. STM images (Figure 4.3 (a) and (b)) show a rather well-ordered stripe structure, with a rectangular unit cell of about 3.6 Å x 15 Å (depicted as a grey rectangle in Figure 4.3 (b)). The LEED pattern of the film is shown in Figure 4.3 (c), while in Figure 4.3 (d) a reproduction of the LEED pattern using the unit cell identified from the STM images is superimposed on the recorded pattern (the substrate's three-fold symmetry is taken into account for the LEED evaluation, and three rotational domains of the rectangular unit cell are used). It can be seen that the measured LEED pattern corresponds rather well to the 3.6 Å x 15 Å rectangular unit cell mentioned above. With respect to Au(111), which has a 2.884 Å hexagonal unit cell⁸³, this V oxide overlayer unit cell can be described by the matrix (0, 1.25 | 6, 3). In turn, that corresponds to a (0, 5 | 6, 3) coincidence lattice having a 14.4 Å x 15 Å Moiré unit cell. This Moiré pattern can not be clearly distinguished in the STM image shown in Figure 4.3 (b); this might be due to a lack of resolution or to unfavorable tunneling conditions (bias, current). It is also possible that the Moiré pattern is not seen in the image because the interaction with the substrate is not strong enough. In that case, neighboring 3.6 Å x 15 Å unit cells of the oxide film would be structurally similar although the location of the substrate gold atoms below them is different. Careful inspection of Figure 4.3 (b) reveals some periodic features within the 3.6 Å x 15 Å unit cell. However, modeling the atomic structure within the unit cell would require better resolved images and the support of theoretical calculations (perhaps in combination with vibrational spectroscopy data). The observation that the films are disordered after their preparation at 400°C in 50 mbar O₂ and that they get ordered after annealing at lower temperature (200°C) in UHV is noteworthy. This indicates that the ordering processes occurring in 50 mbar O₂ and under UHV conditions are different and that the oxygen pressure plays an important role. A small oxygen loss during the UHV annealing would probably be enough to allow the thermally-induced rearrangement of supported VO_x units from ring and zigzag structures into a more extended ordered layer. However, the oxygen loss during UHV annealing up to 200°C must be rather small since the XPS O/V ratio and the V2p binding energy remain very similar before and after the UHV annealing procedure. Another possible explanation would be that the film could already lose a bit of oxygen at the end of the oxida-

tion procedure, when the high pressure cell is pumped-down while the sample temperature is still around 100°C. In other words, a structure with higher oxidation state could exist in 50 mbar O₂ but become unstable and lose oxygen during the transfer to UHV. The resulting reduced layer would then form an ordered structure if enough thermal energy is supplied to overcome the activation energy barrier for the ordering process (here, after annealing to 200°C). In any case, the oxygen loss must be rather small since, as will be shown below, the V atoms in the ordered film still have an oxidation state very close to 5+ (the highest oxidation state of vanadium).

For higher coverage of the first vanadium oxide layer, another ordered structure has been identified. Figure 4.4 shows STM and LEED data corresponding to a film obtained by the oxidation of 0.52 MLE V/Au(111), followed by annealing in UHV at 200°C for 5 minutes (to order the film). This coverage corresponds approximately to the formation of a full monolayer of the oxide. This is substantiated by the fact that large scale STM images (not shown) did not reveal any bare Au(111) patches and at the same time displayed only step heights equivalent to those characteristic of the underlying Au(111) substrate. Correspondingly, the LEED Au(111) reflexes are much weaker (compare Figures 4.3 (c) and (d) to Figures 4.4 (b) and (c)). As seen from the STM picture shown in Figure 4.4 (a), two different structures coexist in the layer: “broader” stripes that are spaced by about 15 Å or appear as isolated features, and “thinner” lines having a periodicity of 9 Å. The second structure seems to be predominant. Although no atomically-resolved STM images could be obtained for this film, it is tempting to assign the first structure to the one observed at lower coverage (with a 3.6 Å x 15 Å rectangular unit cell). Indeed, the lines observed in STM are spaced by 15 Å and a good fraction of the measured LEED diffraction spots is reproduced using this structure. The rest of the spots can be accounted for by using an additional structure having a (1.25x3.75) unit cell with respect to the substrate. This structure has a 3.6 Å x 10.8 Å ($\alpha = 60^\circ$) oblique unit cell. As depicted in Figure 4.4 (d), the vertical distance between the two short sides of this oblique lattice is equal to 9 Å, in very good agreement with the distance measured between the “thinner” lines observed with STM (assuming that the short unit cell vector is aligned along the lines). This structure also forms a (5x15) coincidence lattice, i.e. a 14.4 Å x 43.3 Å oblique Moiré net. It is possible that this explains some faint LEED spots that were not accounted for in Figure 4.4 (c).

The (1.25x3.75) structure is predominant for coverages approaching a complete monolayer whereas it was not observed at low coverage (see Figure 4.3). It is thus probably a more compact structure than the one having a 3.6 Å x 15 Å rectangular unit cell.

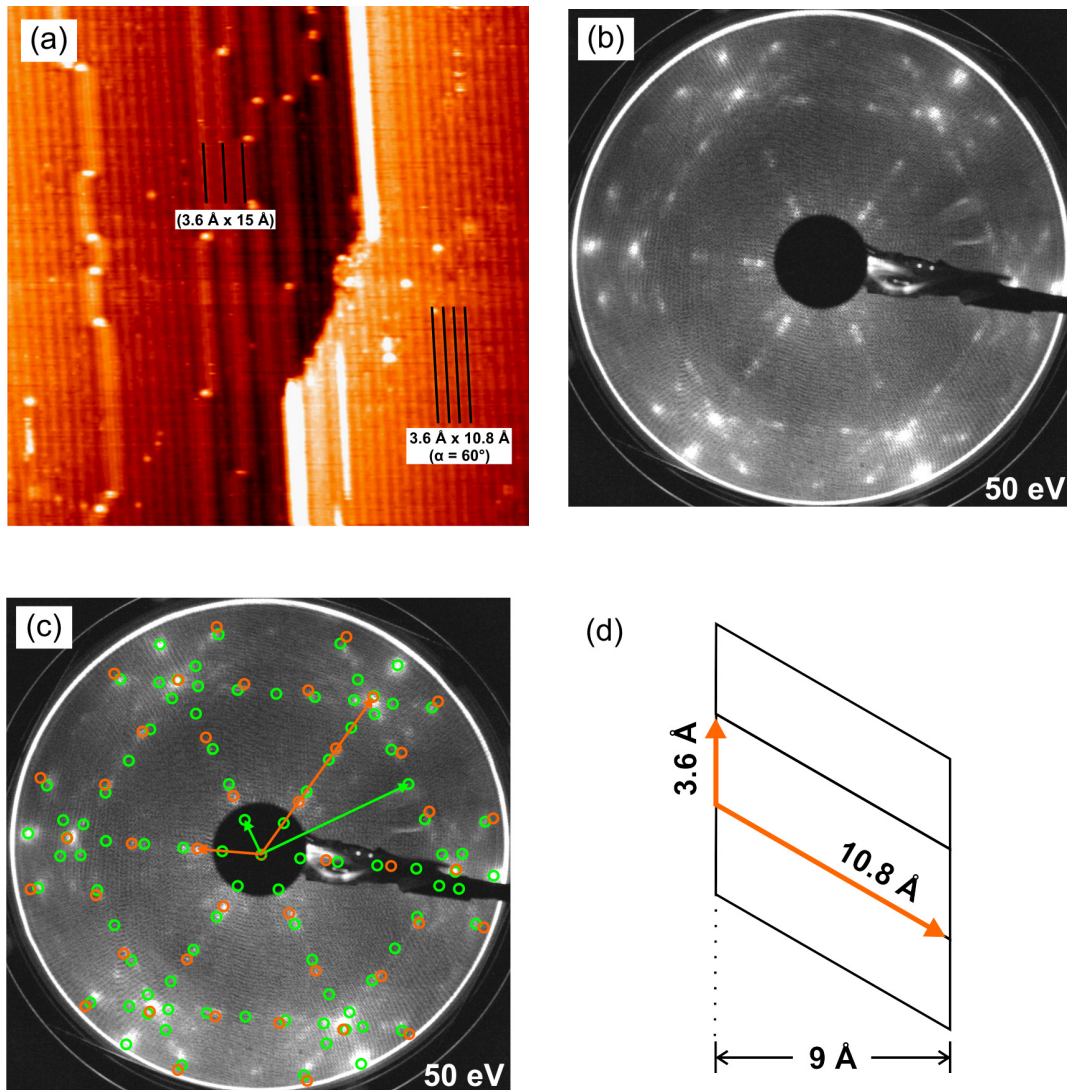


Figure 4.4. STM image (a) (40 nm x 40 nm, 2 V, 0.2 nA) and LEED pattern (b) of a film formed by the oxidation of 0.52 MLE V/Au(111). (c): Reproduction of the LEED pattern using $3.6 \text{ \AA} \times 15 \text{ \AA}$ rectangular and $3.6 \text{ \AA} \times 10.8 \text{ \AA}$ ($\alpha = 60^\circ$) oblique unit cells (green and orange spots, respectively). (d): Real space arrangement of the $3.6 \text{ \AA} \times 10.8 \text{ \AA}$ ($\alpha = 60^\circ$) oblique unit cells forming the rows spaced by 9 \AA observed in STM. Some contrast lines corresponding to the two different structures are indicated in (a).

Interestingly, both unit cells share a common short vector length of 3.6 \AA . This value is very similar to the one found along the $[010]$ direction of V_6O_{13} and V_2O_5 (respectively 3.68 \AA and 3.56 \AA)^{77,78,84}, where it corresponds to the distance between adjacent corner sharing distorted VO_6 octahedra, or in the case of a single layer, corner sharing distorted VO_5 square pyramids. By analogy to the case of vanadium oxide monolayer structures on Rh(111)⁸⁵, it is well possible that the monolayer films observed here on Au(111) are composed of VO_5 square pyra-

mid building blocks that are sharing corners and edges at their base. Depending on the coverage and on the precise oxygen content, different arrangements of these units resulting in more or less compact structures are then possible. The facile rearrangement of coordination polyhedra in vanadium oxides is well known. It is involved, for instance, in the series of shear-plane transitions occurring during the reduction of bulk V_2O_5 (to V_6O_{13} , for example)². The hypothesis that the films might be composed of VO_5 pyramids, a feature characteristic of V_2O_5 , is also supported by the fact that the oxidation state of the V cations in these films is close to 5+. This is revealed by the V2p and O1s XPS data shown in Figure 4.5. One can see in this graph that some changes in the peak positions occur as a function of the thickness of the films. As shown in section 4.3.2, the oxidation of thicker V films (spectrum d) results in the growth of $V_2O_5(001)$ and indeed the V2p_{3/2} signal of such layers has a binding energy of 517.15 eV. This value is similar to the ones reported in the literature for bulk V_2O_5 ^{21,40,47,86}. In the case of the monolayer films (spectra a and b), the V2p_{3/2} signal has a binding energy of about 516.5 eV, which would normally be attributed to a slightly lower oxidation state (of stoichiometry between VO_2 and V_2O_5). However, this is not necessarily the case since for thin layers the XPS final state core holes may be effectively screened by the Au(111) substrate electrons, an effect that would also lead to a reduced binding energy as compared to the thick film case. The observation that the V2p and O1s levels are shifted by about the same energy into the same direction may be viewed as an indication that the shift is mainly a final state effect since the O1s binding energy usually depends only weakly on the oxidation state^{40,47}. Similar final state effects were observed for $Nb_2O_5/Cu_3Au(100)$ ⁸⁷, $V_xO_y/Rh(111)$ ⁸⁵ and $V_2O_3/Pd(111)$ ⁵³ monolayer films. They are also observed for very thin $MoO_3/Au(111)$ films (see section 5.3.1). Still, the discussion on the ordering of the films in UHV at 200°C (see above) showed that it is probable that the vanadium atoms do not have the highest oxidation state possible (5+). One can thus conclude that the average V oxidation state in the monolayer films is 5+ or slightly below. As mentioned before, the layers might be composed of VO_5 square pyramid building blocks that share corners and edges at their base. The stoichiometry of the layer will vary to a small extent depending on how these building blocks are connected: the oxygen content will be higher if the square pyramids rather share corners and it will be lower when edges are shared. For instance, in the case of V_2O_5 each pyramid shares two edges and one corner in the (001) plane (see Figure 4.1)^{77,78}. It is possible that some of the VO_5 square pyramids composing the monolayer structures observed here share a higher number of edges, resulting in an overall stoichiometry slightly below V_2O_5 .

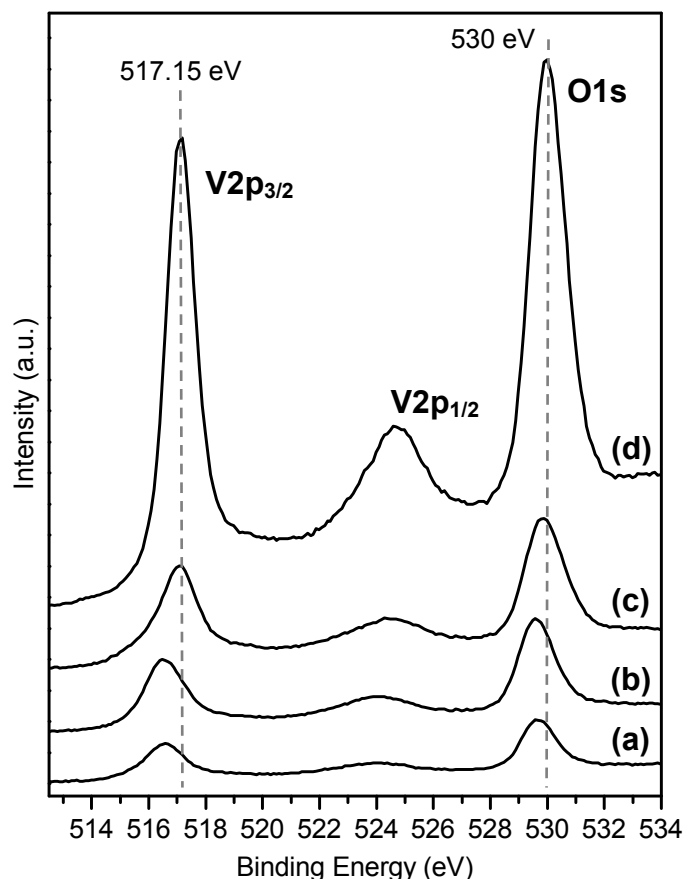


Figure 4.5. XPS spectra (V2p and O1s region) of $V_xO_y/Au(111)$ as a function of the V coverage initially deposited. (a): 0.26 MLE, (b): 0.52 MLE, (c): 1.04 MLE, (d): 7.8 MLE. In all cases, the intensity was normalized to the background signal at 500 eV (the spectra were afterwards shifted with respect to each other along the y axis for display). Mg $K\alpha$, $\theta = 70^\circ$.

The (1.25x3.75) monolayer film obtained after the oxidation of 0.52 MLE V/Au(111) has also been investigated with angle-resolved NEXAFS. In addition to information about the electronic structure of materials, this technique also gives insights into the geometry of the inter-atomic binding. Indeed, the transition matrix elements determining the NEXAFS absorption intensity are connected with the polarization of the exciting beam and the orientation of the molecular bonds. The film has been probed with two different incidence polar angles of the polarized light (α), 70° and 0° , and the resulting spectra are shown in Figure 4.6. The features situated between 515 and 529 eV are related to excitations from the V2p core levels into unoccupied or partially empty V3d orbitals, whereas the peaks in the 529 - 535 eV region pertain to the O K -edge and correspond to transitions from O1s levels to O2p states mixed with V3d levels in the conduction band ($O1s \rightarrow O2p + V3d$)^{43,48,88}. The O K absorption spectrum also contains some features between 537 and 550 eV that are associated to $O1s \rightarrow O2p$

+ V4sp excitations, but these will not be discussed here. In a first approximation, the two broad structures centered at ~ 519 and 525 eV can be assigned to the vanadium L_{III} -edge (V2p_{3/2}) and L_{II} -edge (V2p_{1/2}), respectively. The precise shape of the spectra is determined by intra-atomic electronic interactions, dipole selection rules and the structure of the unoccupied states above the Fermi level. In fact, it has been shown that both the transition energy and the lineshape of the V L -edge vary markedly for different vanadium oxides. According to the results published by Chen *et al*, the position of the V L_{III} -edge shifts from 515.5 eV for metallic V to 519 eV for V₂O₅, with a linear increase of about 0.7 eV per oxidation state⁸⁹. In Figure 4.6, the V L_{III} -edge is centered at a transition energy of about 519 eV, an observation which supports the conclusion that the V oxidation state in the monolayer film is close to 5+ (final state screening effects play a smaller role in the excitation of intra-molecular electronic transitions than they do in photoemission processes⁴³). However, the shape of the L -edge somewhat differs from the one observed in the spectra of V₂O₅(001) single crystals (see Figure 4.14). This is not surprising and it confirms that the structure of the film does not fully correspond to regular V₂O₅. On the other hand, many spectral features are similar, perhaps indicating that the monolayer film and V₂O₅ have some common structural elements. For instance, the angular dependence of the O K -edge between 529 eV and 535 eV is rather well reproduced. This region is composed of two peaks due to the crystal field splitting of the V3d bands^{48,88}. The sharp band observed at lower energy corresponds to transitions to t_{2g} type vanadium levels (pointing in between O ligands, forming weaker π antibonding combinations with O2p orbitals) and the upper broad band to e_g type levels (oriented towards the ligands, forming stronger σ antibonding combinations with O2p orbitals). In the case of V₂O₅, calculations made by Kolczewski *et al* showed that the lower energy peak is determined mainly by the oxygen atoms of the vanadyl groups (V=O)^{90,91}. This peak is most intense if the electric field vector of the X-rays is perpendicular to the V=O bonds (normal light incidence in Figure 4.14, $\alpha = 0^\circ$) and it gets less intense than the upper band when the E-vector gets parallel to them (grazing incidence in our case, $\alpha = 70^\circ$). The close reproduction of the features found for V₂O₅(001) in the NEXAFS spectra of the thin layer as shown in Figure 4.6 may be viewed as a hint that the thin layer and V₂O₅(001) contain similar structural elements including vanadyl groups pointing along the surface normal. In the case of V₂O₅(001) these are responsible for a significant part of the angular dependent intensity in the O K region. This would support the idea of a film composed of VO₅ square pyramids sharing edges or corners of their base at the interface and exposing apical vanadyl O atoms at the surface as also proposed by Schoiswohl *et al* for V oxide monolayers on Rh(111)⁸⁵. However, as mentioned above the details of

NEXAFS spectra depend on many factors and the support of calculations would be necessary to ascertain this model.

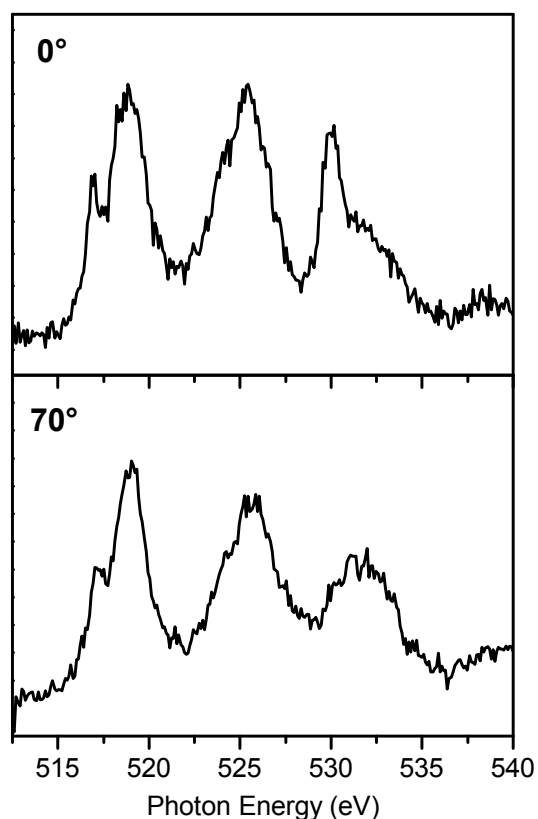


Figure 4.6. Angle-resolved NEXAFS spectra of a film formed by the oxidation of about 0.7 ML V/Au(111). The spectra were acquired at two different polar light incidence angle, 0° and 70° (0° is along to the surface normal). Partial yield detection used for the measurements.

None of the two monolayer structures could be assigned to a known bulk vanadium oxide structure. They are coincidence structures, which points towards a certain degree of interaction with the substrate. The stabilization of unusual oxide structures by metal surfaces is a rather well known phenomenon¹⁸. For films having a thickness of only a few atomic layers, the proximity to the metal surface perturbs the electronic structure of the oxide, leading to atomic arrangements specific to the interface. Although Au(111) might be expected to be rather unreactive, it has been shown before that it can stabilize special interfacial oxide structures: in the case of MoO_3 , which has a bulk *bilayer* structure, an epitaxial $c(2 \times 4)$ MoO_3 *monolayer* has been obtained on Au(111) (see refs.^{92,93} and section 5.3.1). Density functional theory predicts that the MoO_3 monolayer induces an electronic charge redistribution above the Au surface, thereby satisfying the local Mo bonding requirements and stabilizing the oxide film⁹⁴.

Figure 4.7 shows STM images and a LEED pattern obtained after the oxidation of 1.04 MLE V/Au(111), followed by annealing in UHV at 200°C for 5 minutes. The amount of deposited V is twice the quantity used in the case of the second monolayer film described above (see Figure 4.4), where about a full monolayer was obtained. The large scale STM image displayed in Figure 4.7 (a) shows that the film's topography is still very flat, with steps separating rather large terraces.

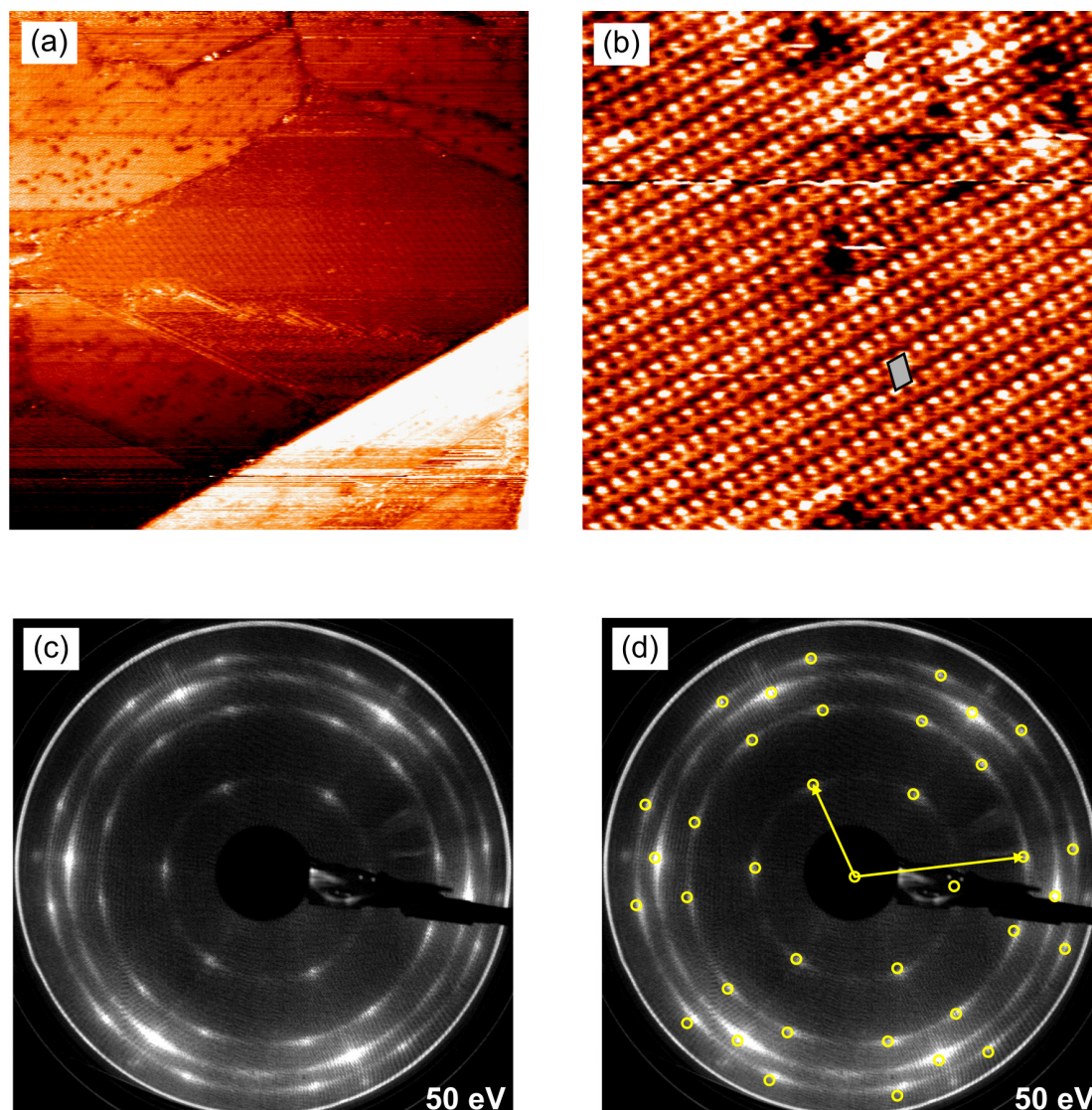


Figure 4.7. STM images ((a): 100 nm x 100 nm, 2 V, 0.2 nA, (b): 10 nm x 10 nm, 2 V, 0.2 nA) and LEED pattern (c) of a film formed by the oxidation of 1.04 MLE V/Au(111). (d): Reproduction of the LEED pattern using a 3.6 Å x 6 Å, $\alpha = 73^\circ$ oblique unit cell.

Atomic resolution STM images (Figures 4.7 (b) and 4.8 (a)) reveal a structure composed of double rows with neighboring double rows shifted by 50 % of the repeat distance within the rows with respect to each other (along the direction of the rows). This corresponds to a 3.6 Å

$\times 6 \text{ \AA}$, $\alpha = 73^\circ$ oblique surface unit cell as depicted by a grey parallelogram in Figure 4.7 (b). This unit cell has been successfully used to reproduce the measured LEED pattern of the film, as shown in Figures 4.7 (c) and (d). One can also observe that rings connect the LEED spots. This will be discussed later.

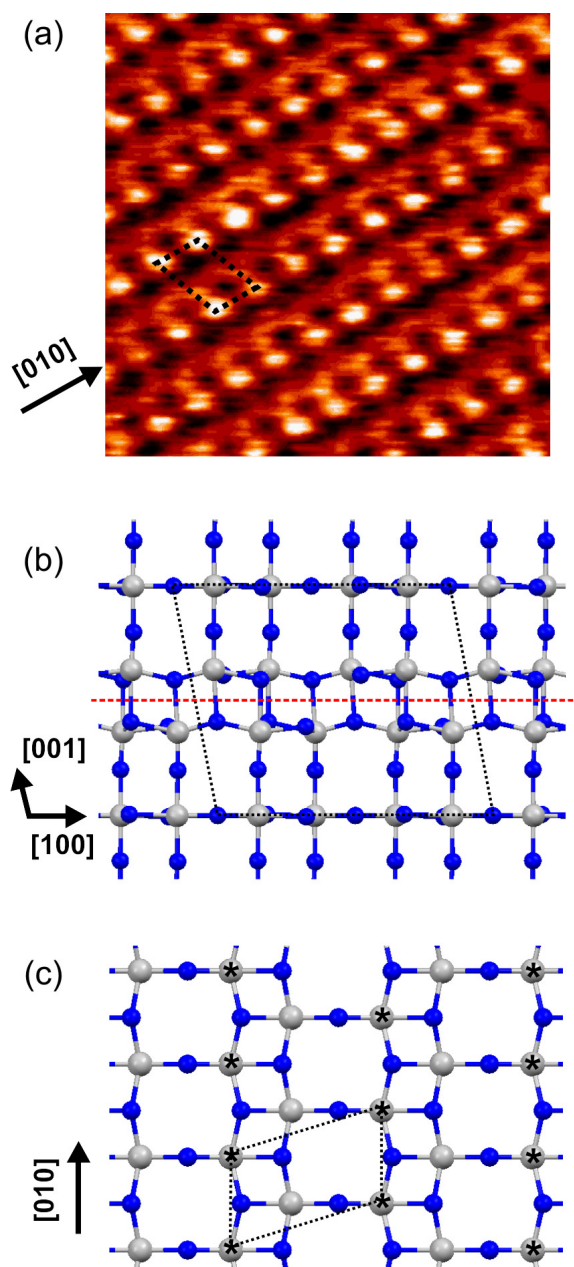


Figure 4.8. (a): STM image (3.4 nm x 3.4 nm, 2 V, 0.2 nA) of a film formed by the oxidation of 1.04 MLE V/Au(111). (b): V₆O₁₃ crystal structure projected along [010]⁸⁴. (c): (001) surface obtained after cleaving a V₆O₁₃ crystal along the plane indicated by a red line in (b). Unit cells are indicated by dotted lines. Blue and grey spheres correspond to O and V atoms, respectively.

A closer view of the surface structure observed with STM is given in Figure 4.8 (a), where the unit cell is indicated by a dotted parallelogram. This image corresponds rather well to the pictures obtained by Smith *et al* on a cleaved $V_6O_{13}(001)$ single crystal⁹⁵. These authors also reported some calculated partial electron density contour plots for different $V_6O_{13}(001)$ surfaces (obtained for various cleavage planes perpendicular to the [001] direction). To a first approximation such contour plots describe the contrast observed in STM images⁹⁶. Figure 4.8 (b) shows a projected view of the V_6O_{13} crystal structure along [010], while Figure 4.8 (c) displays the (001) surface obtained after cleaving along the red line shown in Figure 4.8 (b). Smith and coworkers have determined that this cleavage plane is the most favorable for V_6O_{13} , and that the resulting surface does not significantly relax. The contour plot calculated for this surface in ref.⁹⁵ corresponds well to the STM image shown in Figure 4.8 (a). The origin of the contrast difference between the two sides of the double rows probably stems from the fact that V_6O_{13} is a mixed-valence compound. Based on the different V-O bond lengths in the crystal, Wilhelmi *et al* estimated that some V cations have an oxidation state close to 5+, while others are closer to 4+⁸⁴. In the surface plane depicted in Figure 4.8 (c), two different cation sites coexist according to their prediction: the ones marked by an asterisk should be the closest to 5+ and the others have a slightly lower oxidation state (the two sites are characterized by slightly different V-O bond distances). Each cation type occupies one side of the V double rows and it is near at hand to attribute the observation of V rows with different intensities in Figure 4.8 (a) to this oxidation state difference. Recently, almost identical STM images have also been obtained for $V_6O_{13}(001)$ thin films produced at the surface of reduced $V_2O_5(001)$ single crystals⁹⁷.

The V2p and O1s XP spectrum obtained for this film is shown in Figure 4.5 (spectrum c). Compared to the spectra of the monolayer films (spectra a and b), it is noteworthy that the core levels are shifted towards higher binding energy. This indicates that the possible screening effects described earlier are effectively limited to the first oxide layer. The *maximum* of the V2p_{3/2} peak is now situated at a binding energy of about 517.1 eV. This value is very close to the one typical for V_2O_5 and deviates from the one obtained for V_6O_{13} bulk samples (516.5 eV)^{21,86}. However, it is clear that the peak is broadened towards lower binding energies. Part of this effect can be explained if the film indeed has a mixed-valence character. Additional broadening of the peaks may be due to the presence of a shoulder at lower binding energy, which could arise from the detection of photoelectrons originating from the first (screened) layer. As shown in Figure 4.9 (spectra (b)), this is supported by the fact that the shoulder becomes more intense with respect to the main peak when less surface sensitive XPS conditions

are employed (i.e. when the photoelectrons are collected normal to the surface, $\theta = 0^\circ$). In Figure 4.9, angular dependent XPS spectra corresponding to a monolayer film (oxidation of 0.52 MLE V) are also displayed for comparison (spectra (a)). In this case, the shape of the V2p peaks remains similar for both take-off angles.

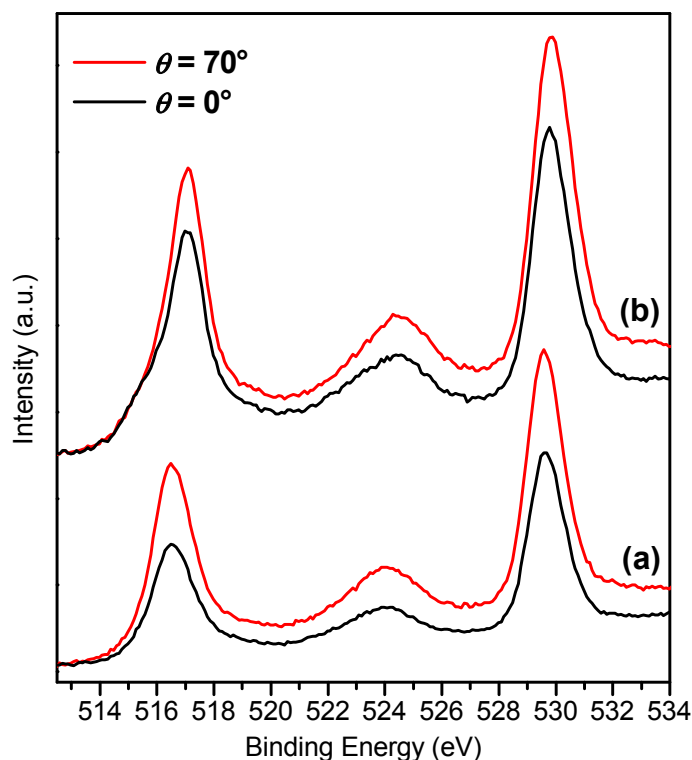


Figure 4.9. XPS spectra (V2p and O1s region) of films formed by the oxidation of (a) 0.52 MLE V/Au(111) and (b) 1.04 MLE V/Au(111). The spectra were acquired with two different electron take-off angles (θ), 0° and 70° . The intensity was normalized to the background signal at 500 eV for each film (the sets of spectra (a) and (b) are however shifted along the intensity scale with respect to each other).

One should note that the bulk unit cell of V_6O_{13} along [001] contains three layers (see Figure 4.8 (b)), whereas the thin film is only two layers thick. In that sense, the film is probably better described as “ $V_6O_{13}(001)$ -like”. In this context, it has to be mentioned that the unit cell measured here (determined from LEED), $3.6 \text{ \AA} \times 6 \text{ \AA}$, is slightly compressed with respect to the surface unit cell of $V_6O_{13}(001)$, which is $3.68 \text{ \AA} \times 6.26 \text{ \AA}$ ⁸⁴. It is also clear that although there is a very good agreement between the STM images shown here and the data measured/calculated by other authors, a completely unambiguous determination of the surface structure cannot be made at the moment. In that respect, it is not very surprising that the value of the V2p_{3/2} core level binding energy is different (by about 0.6 eV) for this ultra-thin film and bulk V_6O_{13} samples. On the other hand, very few studies have been reported for V_6O_{13}

surfaces and in most cases the surface preparation of the samples along with possible effects such as relaxation or reconstruction remain poorly documented.

As mentioned previously, the LEED pattern of this film shows rings connecting the diffraction spots. This means that the various domains in the $V_6O_{13}(001)$ -like film have somewhat random azimuthal orientations. However, as judged from the diffraction pattern it is clear that there is still a preferential orientation along the substrate's main crystallographic directions. It also seems that the azimuthal disorder is *slightly* smaller when the oxidation is carried-out at higher temperatures (~ 500 - 550°C , not shown here). The presence of azimuthal disorder probably stems from a rather weak interaction between the film and the substrate. During oxidation domains might grow rapidly in directions that depend only weakly on the interaction with the substrate since the interaction energy is expected to be small and likely does not depend very much on the azimuthal angle. As the domains get more extended, the thermal energy required to reorient them will increase. This is in contrast to the case of the monolayer films described previously, where the oxide structure is most likely determined and stabilized by the interaction between the film and the substrate.

4.3.2 Thicker films: $V_2O_5(001)$

The structure of the films has also been investigated for higher thicknesses. Figure 4.10 displays STM images obtained for a film prepared by the oxidation of about 1.56 MLE $V/Au(111)$, a thickness slightly larger than (~ 1.5 times) the one required for the formation of the $V_6O_{13}(001)$ -like thin film described above. The images have been differentiated to allow the visualization of the various topographic features without contrast saturation. It appears that some crystallites have grown on top of another oxide layer. Smaller scale images (not shown here) revealed that the layer between the crystallites has the same surface structure as the $V_6O_{13}(001)$ -like thin film. In the case of the crystallites, however, the distance between the bright contrast rows is $\sim 11.5 \text{ \AA}$, a value typical for $V_2O_5(001)$ surfaces⁹⁵. It thus seems that the $V_6O_{13}(001)$ -like film acts as an interface layer between the $Au(111)$ substrate and a growing $V_2O_5(001)$ film. The arrangement of $V_2O_5(001)$ is shown in Figure 4.11, where double rows of vanadyl O atoms are seen to extend along the $[010]$ direction. This surface has a $3.56 \text{ \AA} \times 11.52 \text{ \AA}$ rectangular unit cell. Careful inspection of the $V_2O_5(001)$ islands reveals that they grow with a preferential orientation with respect to the underlying interface. Indeed, the double row structures of the interface and the growing crystallites are generally aligned parallel to each other. This is shown in Figure 4.10 (b), where arrows indicate the $[010]$ direction (along the double rows) of the different domains. The relative orientation of the two layers

would correspond to a rather favorable epitaxial relationship. For the $V_6O_{13}(001)$ -like surface, a $3.6 \text{ \AA} \times 11.45 \text{ \AA}$ rectangular unit cell can be drawn by using the short unit vector of the primitive oblique unit cell and considering a longer unit vector going from one double row to the second nearest double row (which is not shifted with respect to the first one). A rather small misfit between the two layers can then be obtained for a parallel alignment of the double rows. Although this seems reasonable, the present data do not allow to exclude the possibility that the V_2O_5 crystallites extend to the Au(111) surface and that the V_6O_{13} -like structure would not subsist at the interface.

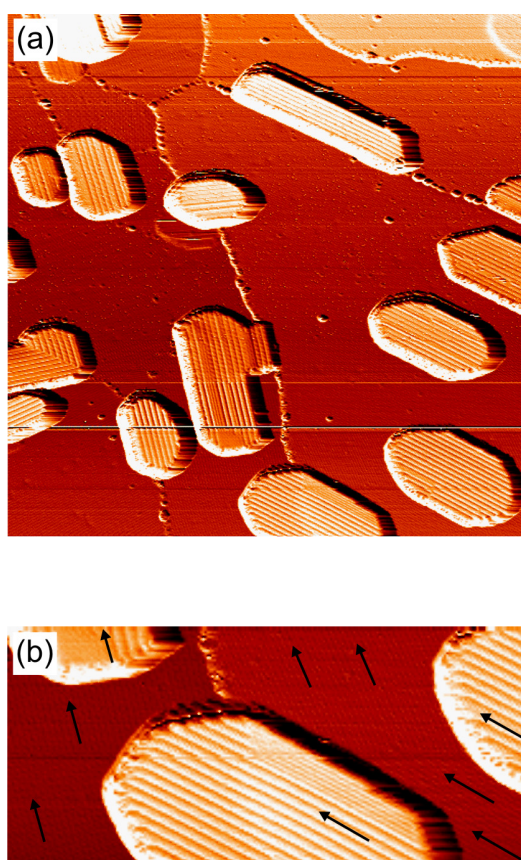


Figure 4.10. STM images ((a): $100 \text{ nm} \times 100 \text{ nm}$, 3 V , 0.2 nA , (b): $44 \text{ nm} \times 20 \text{ nm}$, 3 V , 0.2 nA) of a film formed by the oxidation of $1.56 \text{ MLE V/Au}(111)$ (differentiated images). In (b), arrows indicate the $[010]$ direction of the various domains (see text).

In Figure 4.10, it can also be observed that the crystallites have an elongated shape and that they seem to grow more favorably along their $[010]$ direction (along the vanadyl double rows). This preferential growth direction appears to be typical for V_2O_5 ; it was also found by Groult and coworkers, who observed the formation of $[010]$ -elongated nanocrystals (with AFM and XRD) after annealing amorphous vanadium pentoxide thin films on silicon in air⁷⁰. V_2O_5 single crystals prepared by melt-techniques are also known to be generally more ex-

tended in the [010] direction¹². Upon further growth (i.e. if a thicker V layer is oxidized), flat $V_2O_5(001)$ films containing a low number of point defects can be obtained.

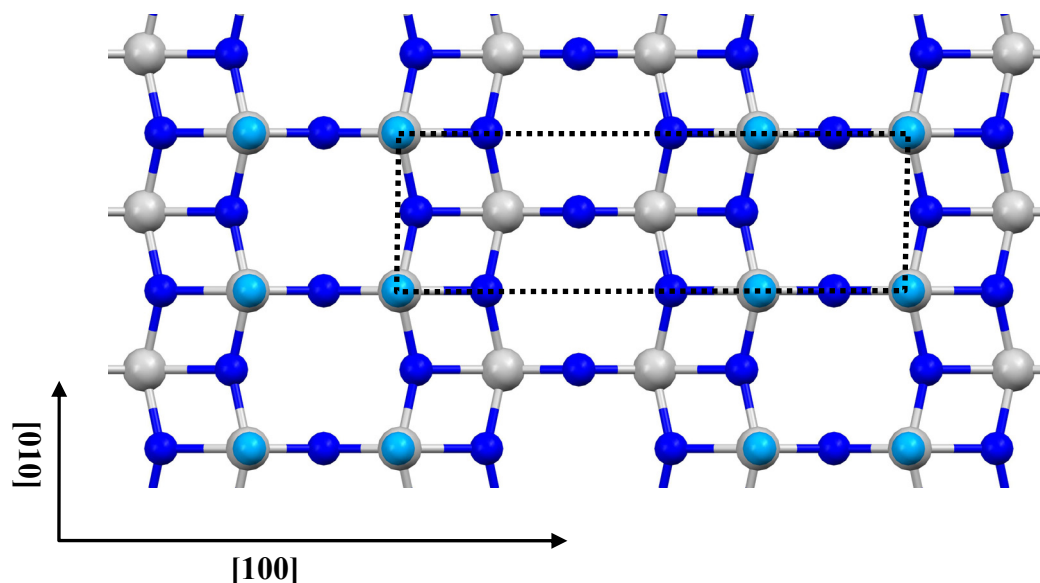


Figure 4.11. $V_2O_5(001)$ geometric structure⁷⁸. The unit cell is indicated by a dotted line. Gray spheres indicate the position of the vanadium atoms while blue spheres pertain to oxygen atoms. The vanadyl O atoms are represented by light blue spheres.

Figure 4.12 (a) displays a large scale STM picture of a film obtained by the oxidation of 5.2 MLE V/Au(111). The quantity of vanadium that is required to complete a $V_2O_5(001)$ single layer is equal to about 0.7 MLE, which means that the oxidation of 5.2 MLE V would result in a V_2O_5 film thickness of ~ 7.4 layers (3.2 nm), assuming the growth of a uniform and ordered $V_2O_5(001)$ film and assuming that sublimation does not occur during oxidation. From the image, one can see that the V_2O_5 islands have coalesced to some extent and that rather big crystallites have formed. Also, the STM image reveals large darker areas that are about 4 nm deep, where the surface structure of the $V_6O_{13}(001)$ -like interface could be resolved (Figure 4.12 (b)). As indicated in Figure 4.12 (b), this structure is characterized by an oblique unit cell ($3.6 \text{ \AA} \times 6 \text{ \AA}$, $\alpha = 73^\circ$). This observation means that the V_2O_5 film does not fully cover the interface layer. However, the surface of the crystallites displays a well-ordered $V_2O_5(001)$ structure containing a low number of point defects. The double row structure and the unit cell characterizing $V_2O_5(001)$ are clearly visible in the high resolution STM images shown in Figures 4.12 (c) and (d). Some line defects are also occasionally observed, as seen in the upper-right corner of Figure 4.12 (d).

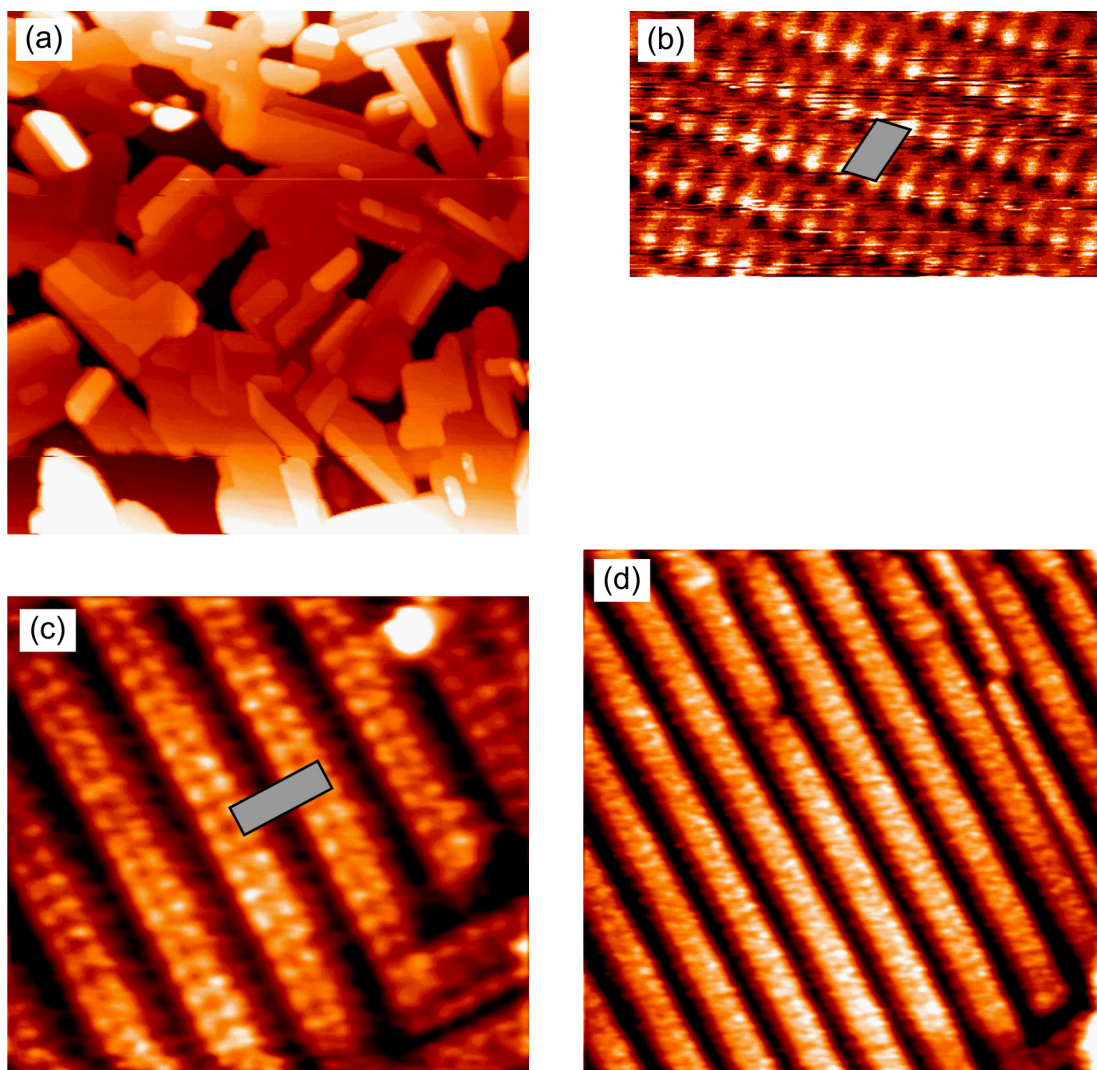


Figure 4.12. STM images of a film formed by the oxidation of 5.2 MLE V/Au(111) ((a): 300 nm x 300 nm, 3.5 V, 0.2 nA, (b): 5 nm x 2.8 nm, 3 V, 0.2 nA, (c): 6.3 nm x 5.8 nm, 2 V, 0.2 nA, (d): 10 nm x 10 nm, 2 V, 0.2 nA). Image (b) was acquired in one of the dark areas of (a), while images (c, d) are representative of the high features. In (b) and (c) the surface unit cells are indicate by grey parallelograms.

The origin of the contrast in the STM images of $V_2O_5(001)$ has been debated in the past^{95,98-100}. As can be seen in Figure 4.11, the surface exposes both double rows of vanadyl groups and vanadium atoms (the two alternate along [100]). Authors have expressed various opinions concerning which one of the two features is really imaged in STM (especially as a function of the bias). STM observations of transition metal oxides are often interpreted by assuming that the empty-state images are dominated by the more electropositive atoms (metal) and that the filled-state images are rather influenced by the electronegative atoms (oxygen). In the case of V_2O_5 , the valence and the conduction bands are indeed dominated by $O2p$ and $V3d$ states, respectively. Based on this, different groups assigned the features ob-

served in the positive bias (empty-states) STM images to the double rows of exposed vanadium atoms^{98,99}. Intuitively this might seem reasonable, but there are good arguments supporting the opposite. First, one has to consider that in V_2O_5 the conduction and valence bands are formed by *hybridized* O2p and V3d orbitals^{48,101}. Also, for the rather high biases used here the electrons tunnel in the upper part of the conduction band where the contribution of O2p states is relatively high¹⁰⁰. The main reason why the exposed V=O groups could be responsible for the STM contrast is actually a geometric argument: the vanadyl oxygen atoms stick out of the surface; the oxygen atoms of the vanadyl groups are about 2 Å higher than the vanadium atoms of the vanadium rows. Due to V3d+O2p hybridization there will be unoccupied density of states near to the position of the vanadyl oxygen cores and tunneling may occur into these states. Since these states stick out of the surface they may appear more prominent in the STM images than states related to the vanadium rows between the vanadyl double rows. In agreement with the calculations performed by Smith *et al*^{95,100} and with the observations made for $V_2O_3(0001)/Au(111)$ (Chapter 3), the bright protrusions in the STM images shown in Fig. 4.12 (c) and (d) are assigned to the vanadyl groups on the $V_2O_5(001)$ surface. Accordingly, occasional missing bright protrusions (see the middle-top part of Figure 4.12 (d)) are attributed to vanadyl O vacancy point defects.

The XPS spectrum corresponding to this film (oxidation of 5.2 MLE V) is displayed in Figure 4.13 (spectrum c). As expected for V_2O_5 , the $V2p_{3/2}$ peak appears at a binding energy of 517.15 eV^{21,40,47,86}. A small shoulder also seems to be present on the low binding energy side of the peak, suggesting the presence of some V atoms with a lower oxidation state in the film. This extra intensity might in part come from the surface areas where the interface layer is exposed (see spectrum a, which corresponds to the $V_6O_{13}(001)$ -like interface film). Indeed, for thinner $V_2O_5(001)$ layers a greater fraction of the interface is uncovered and the shoulder at lower binding energy is more prominent (see spectrum b). However, as discussed below some surface reduction during the XPS analysis cannot be excluded and probably also contributes to the intensity of the shoulder.

The V_2O_5 films were also characterized with angle-resolved NEXAFS. The results are shown in Figure 4.14 for a film produced by the oxidation of 2.6 MLE V/Au(111) together with $V_2O_5(001)$ single crystal data on the same graphs. The spectra are almost identical, confirming the attribution of the film structure to V_2O_5 . The fact that the intensity of the various bands has the same variation as a function of the light incidence polar angle then also proves that the film is indeed (001)-oriented. Small differences between the two sets of spectra can originate from contributions of the interface layer. Also, although the single crystal data were

recorded for a defined azimuthal orientation, those corresponding to the thin films are intrinsically acquired over an average of different azimuthal angles (this is due to some rotational disorder in the thin film, see below). This has probably an effect since some small variations in the NEXAFS spectra of $V_2O_5(001)$ single crystals are expected as a function of the azimuthal orientation ⁹¹.

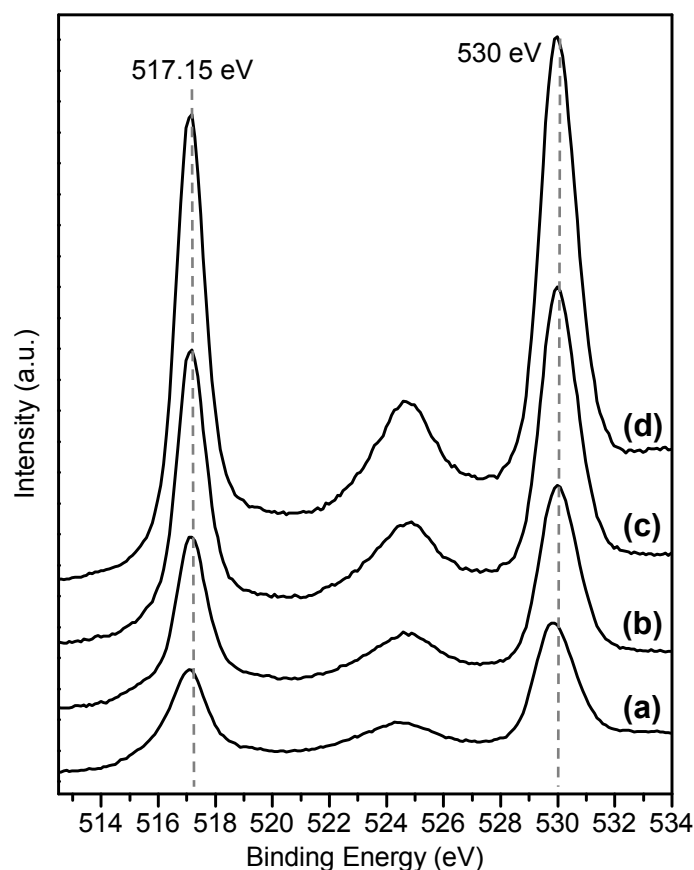


Figure 4.13. XPS spectra (V2p and O1s region) of $V_xO_y/Au(111)$ as a function of the V coverage initially deposited. (a): 1.04 MLE, (b): 2.08 MLE, (c): 5.2 MLE, (d): 3 successive deposition of 2.6 MLE V and oxidation cycles. In all cases, the intensity was normalized to the background signal at 500 eV (the spectra were afterwards shifted with respect to each other along the y axis for display). Mg $K\alpha$, $\theta = 70^\circ$.

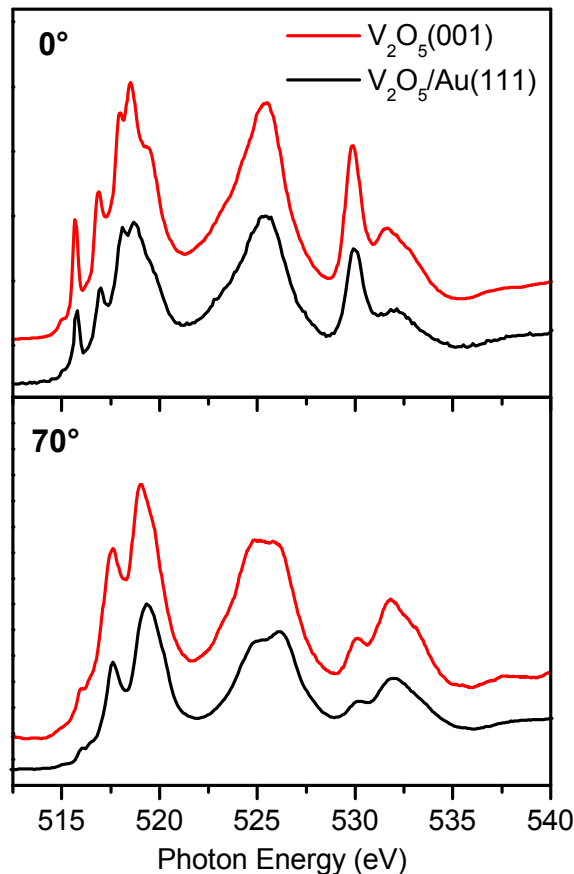


Figure 4.14. Comparison between the NEXAFS spectra obtained for a $V_2O_5(001)$ single crystal and for a film formed by the oxidation of about 2.6 MLE V/Au(111). The spectra were acquired at two different polar light incidence angles, 0° and 70° (0° is along to the surface normal). Total electron yield detection used for the measurements.

The fact that the thin films grow with their [001] crystallographic axis oriented parallel to the surface normal is not very surprising. Indeed, the weakly interacting layers constituting V_2O_5 are stacked along this direction and it is rather straightforward to see that the (001) plane is the surface with the lowest free energy of this crystal structure (a calculated value of 0.040 J/m^2 has been reported¹⁰²). This explains why V_2O_5 has a higher tendency to expose its (001) surface, an effect which is experimentally commonly observed for single crystals¹² and powder particles¹⁰³. As a matter of fact, it seems that V_2O_5 films have a tendency to grow with a preferred (001) orientation regardless of the nature of the substrate (this was for instance reported for amorphous glass⁷¹). Considering this, it would be tempting to describe the growth of $V_2O_5(001)$ thin films in terms of van der Waals epitaxy¹⁰⁴. This growth mode was observed for other compounds made of layers interacting by van der Waals forces like transition metal dichalcogenides (MoS_2 , $NbSe_2$, etc). In this case, ultrathin films can grow with

their own lattice constant on various (unreactive) substrates, even under the existence of very large lattice mismatch. The present case is however slightly different, as an interface layer with a dissimilar structure first grows on Au(111) before the regular $V_2O_5(001)$ sheets start to form. Very similar observations can be made for the growth of MoO_3 on Au(111), see Chapter 5. This is in contrast to the $MoS_2/Au(111)$ system, where a regular $MoS_2(0001)$ structure was observed for monolayer-thick nanocrystallites⁸⁰.

It has been mentioned before that very few oxygen vacancy point defects could be observed with STM. This conclusion was further evidenced with valence band photoemission spectroscopy. A spectrum is shown in Figure 4.15 for a film formed after the oxidation of 2.6 MLE V/Au(111). The broad features between ~ 3 and 9 eV are due to emission from oxygen and vanadium levels in the oxide band structure and their general shape corresponds rather well to the one observed for UHV-cleaved $V_2O_5(001)$ single crystals^{20,105}. The low abundance of not fully oxidized vanadium atoms can be judged from the nearly vanishing emission intensity in the binding energy range between the Fermi edge and 3 eV. The emission from the V3d levels of not fully oxidized vanadium atoms would show up in this spectral region⁴⁷. Obviously, in the present case only a very faint signal can be observed. It can even be argued that some of this intensity comes from radiation-induced reduction occurring during the acquisition of the spectrum.

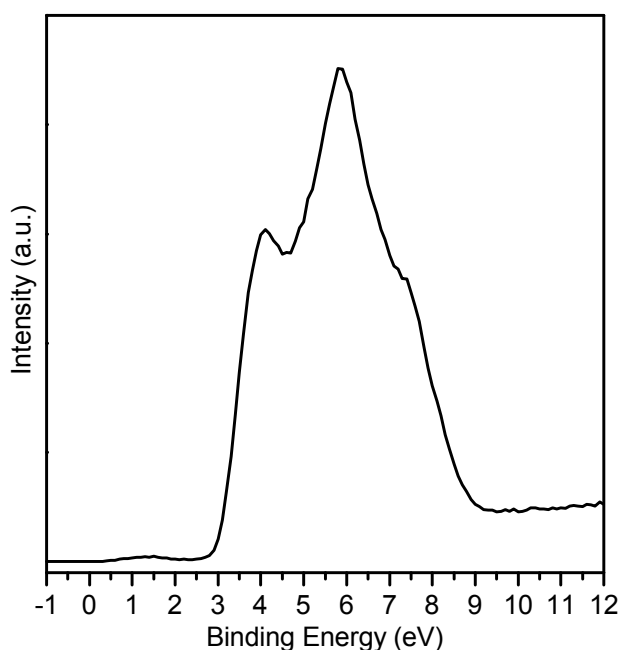


Figure 4.15. Valence band photoemission spectrum of a film formed by the oxidation of 2.6 MLE V/Au(111). 121 eV photon energy, $\theta = 70^\circ$.

The growth of “closed” $V_2O_5(001)$ films that do not expose interface areas is important for adsorption/reactivity studies. For such investigations it could otherwise be difficult to disentangle the spectroscopic signal coming from molecules adsorbed on the various surfaces: interface layer, surface and side facets of the $V_2O_5(001)$ crystallites. For films prepared by the oxidation of V layers with thicknesses ranging from 1.56 to 5.2 MLE, some interface area was always left uncovered. It also appeared that between 3.15 and 5.2 MLE V, this area stayed more or less constant and that mainly the height of the $V_2O_5(001)$ crystallites increased. This effect could be due to Ostwald ripening occurring during the oxidation process which would result in the growth of bigger crystals at the expense of the smaller ones. It was possible to avoid this problem by growing the films in multiple V evaporation/oxidation steps. Figure 4.16 (a) shows a large scale STM image corresponding to a film prepared by the sequential evaporation and oxidation of three 2.6 MLE V layers. The conditions used for the oxidation were the same as the ones used for the other films (400°C, 50 mbar O_2 , 10 minutes). Several of these large scale images could be recorded at various places on the sample surface and in all the cases no exposed interface was observed. The majority of steps seen in Figure 4.16 (a) has an apparent height corresponding to one $V_2O_5(001)$ layer ($\sim 4.4 \text{ \AA}$). As evidenced in Figure 4.16 (b), the surface also displays rather large single crystalline domains and very few point defects. However, the size of the domains is perhaps a bit smaller than in the case of the films grown in one evaporation/oxidation step, and a number of grain boundaries plus some occasional screw dislocations can be observed. Considering that ~ 0.7 MLE V is required to complete a $V_2O_5(001)$ single layer, this film is expected to have a thickness of about 11 layers, i.e. 4.8 nm (since the unit cell vector along [001] has a length of 4.37 \AA ⁷⁸, see Figure 4.1 (a)).

A possible reason why the morphology is different if the layer is grown in several steps would be that evaporated *metallic* V layers grow differently on top of an existing V oxide film and on gold. It may be assumed that metallic V on vanadium oxide is flatter and more dispersed than on Au due to a stronger interaction with the oxide surface (the evaporated metal atoms can interact with the oxygen atoms of the oxide and form chemical bonds). This would then provide a different starting point for the growth of crystallites via atomic rearrangement within crystallites, coalescence of crystallites and Ostwald ripening during the oxidation procedure at elevated temperature and could delay the formation of very big islands and uncovered interface areas. The fact that the films grown in multiple steps were always flatter was also confirmed by the higher damping of the substrate’s core levels signal observed in the XPS data.

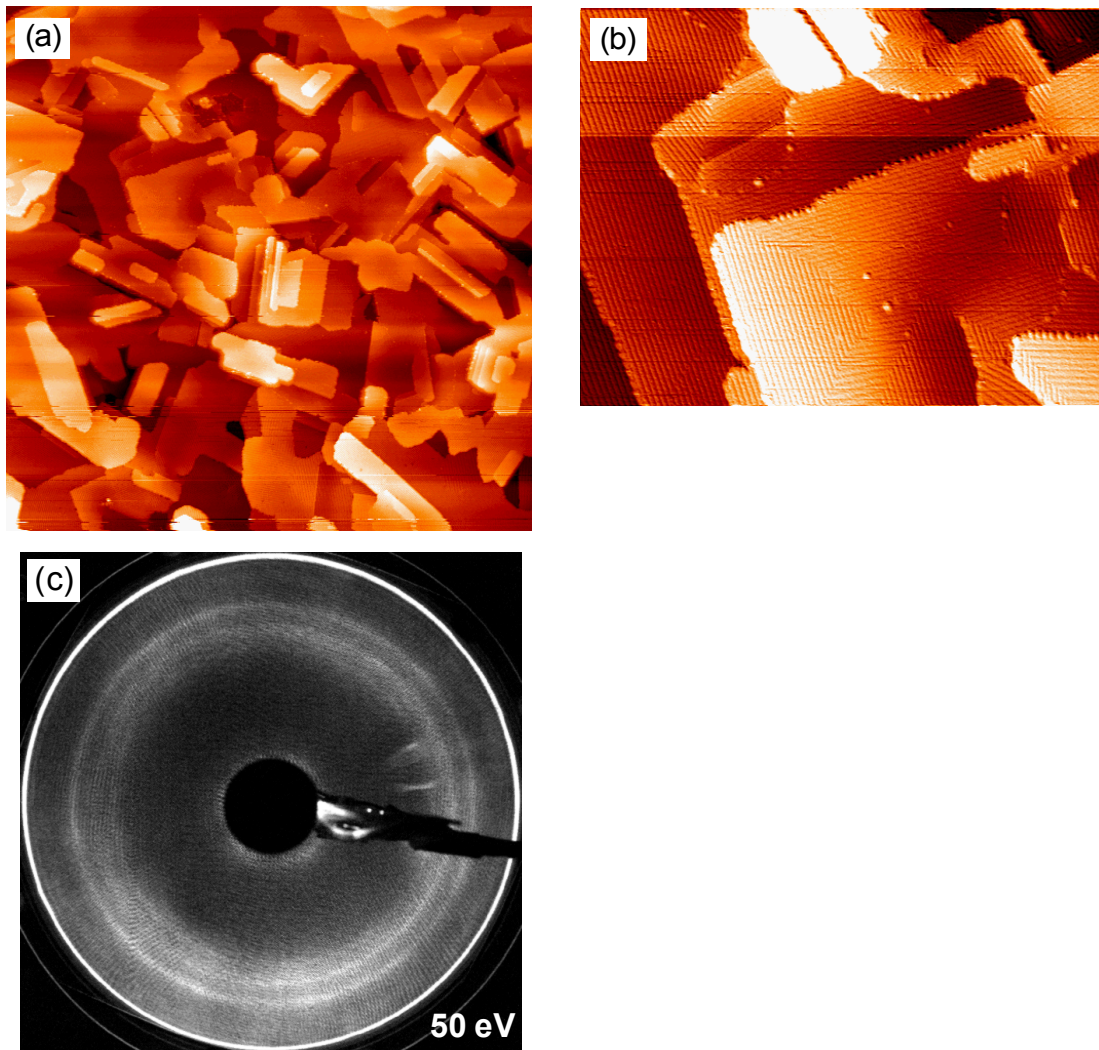


Figure 4.16. STM images ((a): 300 nm x 300 nm, 3.5 V, 0.2 nA, (b): 100 nm x 75.8 nm, 3 V, 0.2 nA (differentiated)) and LEED pattern (c) obtained for a film formed by three successive depositions of 2.6 MLE V and oxidation cycles.

The LEED patterns of the $V_2O_5(001)/Au(111)$ thin films show rings instead of spots (this is shown in Figure 4.16 (c) for a film formed by the deposition/oxidation of three 2.6 MLE V layers). Such an observation means that the [001]-oriented crystalline domains composing the film have random azimuthal orientations. This can also be observed in the STM image shown in Figure 4.16 (b). Rotational disorder was also observed for the interface layer and it has been attributed to a rather weak interaction between the growing film and the substrate. Since STM reveals well ordered surfaces, the background intensity in the diffraction pattern seen in Figure 4.16 (c) is mostly ascribed to electron beam-induced reduction of the film during the LEED experiment. In fact, it is well-known that V_2O_5 is sensitive to electron

beams^{13,14}. In the present case, this reduction was obvious as the LEED pattern would fade away in only a few seconds. The same observation was reported for V₂O₅ single crystals²⁰.

The closed films were also characterized with XPS. A spectrum corresponding to a film grown in three evaporation/oxidation steps (3 x 2.6 MLE V layers) is shown in Figure 4.13 (spectrum d). The spectrum displays rather sharp V2p_{3/2} and O1s peaks positioned at binding energies of 517.15 and 530 eV, respectively, and is very similar to spectra reported previously for V₂O₅ (see ref.⁴⁰, for instance). Nevertheless, the V2p peaks can not be fitted with only one component and an extra weak peak has to be accounted for on their lower binding energy side. In other words, a small fraction of reduced V species is present on the surface. This can likely be attributed for the most part to X-ray induced reduction taking place during the analysis. The reduction of V₂O₅ by X-ray exposure was investigated by Chenakin *et al*, who concluded that XPS recorded with parameters similar to the ones that we employed induces the rapid formation of a small fraction of V⁴⁺ species on the surface¹⁵. X-ray induced damage in oxides is believed to be mainly caused by electron-hole pair creation and Auger decay⁶¹. The multiple hole states created in the valence band by Auger decay can break bonds between V and O, leading to the reduction of vanadium atoms and to the desorption of oxygen. This damage is hard to avoid and the observation of small amounts of reduced V species at the surface of V₂O₅ with XPS is thus rather common^{14,20,40}. STM images taken after the XPS analysis of the film (Figure 4.17) clearly reveal this effect. During the analysis, the sample was exposed to Mg K α radiation for about 90 minutes, the X-ray source being operated at a power of 260 W. Compared to the pictures obtained for the same film before X-ray exposure (Figure 4.16), dark features are now distributed on the vanadyl oxygen double rows. The presence of significant amounts of C-containing adsorbates, OH or H₂O on this surface can be excluded based on the XPS results: no intensity could be detected in the C1s region (not shown here). Also, hydroxyl groups or adsorbed water molecules would give rise to O1s intensity in the binding energy range between 531 and 533 eV²³, which was not observed here (see Figure 4.13, spectrum d). Single missing bright protrusions (dark spots) in the STM images of as-prepared V₂O₅(001) thin films have already been attributed to missing vanadyl O atoms point defects (for reasons mentioned above). Similarly, the darker areas of the double rows in Figure 4.17 can be assigned to groups of missing vanadyl O atoms. The images clearly reveal that the vacancies are not distributed randomly on the surface and they mostly appear somewhat grouped together. Similar observations have been made by Smith *et al* for cleaved single crystals (which, in their experiments, apparently showed some degree of reduction)¹⁰⁰.

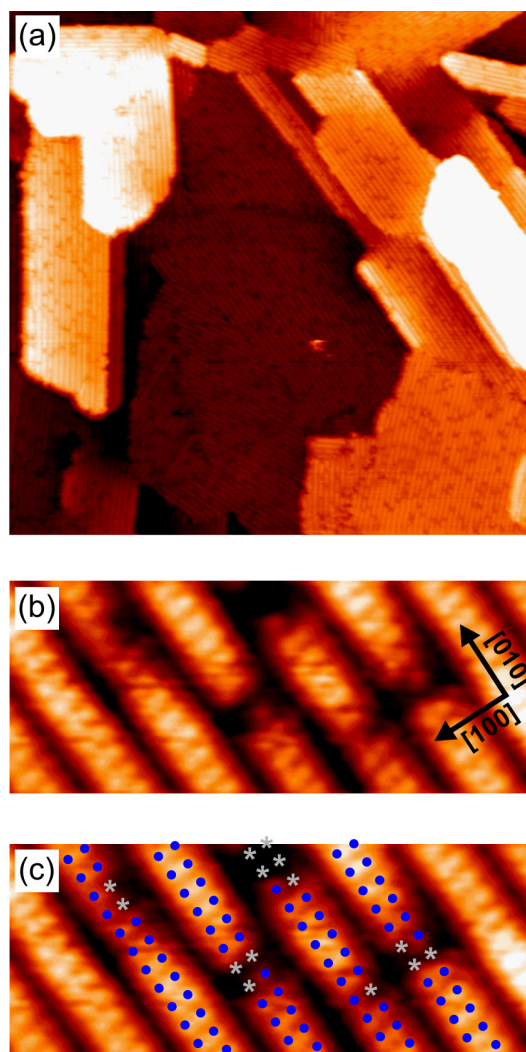


Figure 4.17. STM images ((a): 100 nm x 100 nm, 3 V, 0.2 nA, (b and c): 7.7 nm x 3.1 nm, 3 V, 0.2 nA) of a $V_2O_5(001)$ film exposed to Mg $K\alpha$ X-rays (film formed by 3 depositions/oxidation cycles of 2.6 MLE V). Image (c) is a copy of (b), where the missing and remaining vanadyl O atoms are respectively indicated with asterisks and circles.

In Figure 4.17 (c), the positions of the missing oxygen atoms seen in Figure 4.17 (b) are highlighted by grey asterisks (whereas the surrounding remaining vanadyl O are indicated by blue circles). Vacancies are seen to form pairs along $[100]$ and/or rows along $[010]$. The formation of oxygen vacancies at the surface of $V_2O_5(001)$ has been investigated with density functional theory by Ganduglia-Pirovano and Sauer¹⁰² and by Hermann *et al*¹⁰⁶. Their results show that the vacancy formation energy is much lower for vanadyl oxygen than for two- and threefold coordinated surface oxygen atoms. The calculations of Ganduglia-Pirovano and Sauer also predicted that the reduced V cations (resulting from the loss of the vanadyl O atom) are stabilized by relaxation: the cation moves downwards and forms a bond with a vanadyl oxygen of the layer underneath. This relaxation lowers the vacancy formation energy for the neighboring

surface V=O oxygen atoms, resulting in a concerted reduction of the surface. Their results indeed predict that upon reduction of the surface, missing rows along [010] will preferentially form. On the other hand, the calculations suggest that vacancy pairs along [100] (one vacancy on each side of a double row) would have a *higher* formation energy than single vacancies. Interestingly, for the experimental parameters used here such missing vanadyl O vacancy pairs appear to be very common.

4.3.3 Thermal stability

As mentioned previously, the thermal stability of the films under UHV has been investigated with TPD and XPS. Figure 4.18 shows data obtained for a closed $V_2O_5(001)$ film formed by 3 cycles of deposition and oxidation of 2.6 MLE V and Figure 4.19 exhibits data pertaining to a film formed by the oxidation of 5.2 MLE V (a $V_2O_5(001)$ film where some parts of the interface are exposed). Finally, Figure 4.20 shows the results corresponding to a film with a coverage of less than one oxide monolayer (formed by the oxidation of 0.26 MLE V). The two last sets of TPD curves (Figures 4.19 and 4.20) are mainly discussed to explain some of the features observed in the data obtained for the closed $V_2O_5(001)$ film. For clarity, in all cases the desorption curves have been plotted in two separate graphs (the curves were recorded in the same TPD run). Since the sensitivity of the mass spectrometer for the various gases was not calibrated, the absolute values of the partial pressure should not be given too much significance. However, the signal for each fragment can be compared to some extent from one experiment to the other.

The upper part of Figure 4.18 reveals that some vanadium oxide fragments are released into the gas phase upon heating a $V_2O_5(001)$ film in the temperature range between 500°C and 660°C. It thus appears that the oxide starts sublimating or decomposing at a temperature of about 500°C. The V_xO_y desorption spectrum is divided in three regions: a rather broad peak is first observed between 500°C and 610°C, with a maximum at ~ 585°C and a clear shoulder around 600°C. A second very sharp peak appears at a temperature of 616°C, and a last broad desorption region can be observed between 625°C and 660°C. Before discussing these features in more details, the reduction of the film, which should be accompanied by a release of oxygen, will be considered.

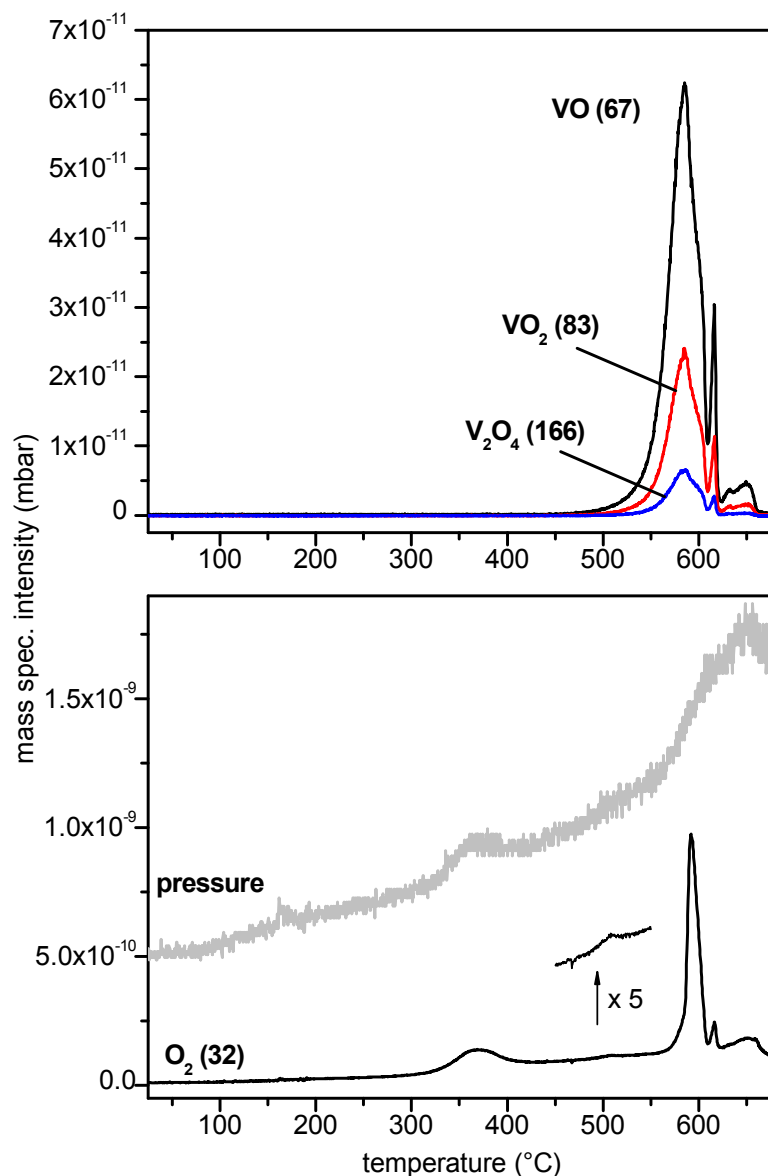


Figure 4.18. TPD of a V₂O₅(001) film formed by 3 depositions/oxidation cycles of 2.6 MLE V. The evolution of the main chamber pressure during the TPD run is displayed in the lower graph.

The O₂ desorption curve (lower part of Figure 4.18) contains several peaks. The first broad peak situated between 300°C and 420°C can be attributed to a release of oxygen from the Pt sample holder. In fact, the Pt parts surrounding the sample (see Chapter 2) are also exposed to 50 mbar O₂ during the oxidation procedure and they are expected to adsorb considerable amounts of oxygen. It is well known that O₂ adsorbs dissociatively at room temperature on Pt¹⁰⁷. The resulting surface O atoms are generally observed to recombine and desorb at temperatures around 300°C – 600°C (the exact temperature depends on the surface plane, the

coverage, the heating rate, etc) ^{107,108}. The position of the peak observed in our case corresponds quite well to the flash desorption data reported by P. R. Norton for Pt foils exposed to oxygen, where a broad desorption feature starts at about 300°C ¹⁰⁸. A further argument supporting this assignment comes from the fact that the intensity of the peak is almost the same in the TPD spectra of all the films, including the fractional coverage monolayer (compare Figures 4.18-4.20). If this O₂ desorption peak would originate from a reduction of the vanadium oxide layer, one would rather expect its intensity to scale somewhat with the thickness of the layer. The Feulner cup used in our experiments shields to some extent the mass spectrometer from the molecules emitted from the surrounding of the sample. However, a significant O₂ release from the sample holder augments the pressure in the UHV chamber and increases the quantity of O₂ molecules that can reach the mass spectrometer detector by passing through the small gap between the Feulner cup entrance and the sample surface (~ 1 mm).

The O₂ intensity does not fully go down at higher temperatures after the peak and continues increasing on a steady slope. This seems to follow the evolution of the main chamber's pressure. A gradual warm-up of the Pt parts that are further away from the sample and are not directly heated might contribute to the gradual O₂ desorption/pressure increase. In fact, XPS results indicate that no significant reduction of the films takes place at 450°C. This is evidenced in Figure 4.21, where spectra acquired after preparation and following heating at 450°C for 5 minutes are seen to be identical. The spectra have been slightly shifted along the ordinate axis; otherwise the two curves would be undistinguishable. There is a small O₂ desorption peak at about 500-510°C which is more clearly visible after magnification of the intensity scale (see Figure 4.18). This may be due to a slight oxygen loss of the oxide layer. However, this peak's intensity and desorption temperature varies somewhat from one preparation to the other, which means that it might also originate from the Pt sample holder.

In contrast to the other O₂ desorption features observed at lower temperatures, a very sharp and intense peak can be seen between 560°C and 610°C in Figure 4.18. The peak reaches a maximum at ~ 590°C and seems to coincide with the intensity decrease of the first V_xO_y desorption feature. As mentioned before, the latter has a high temperature shoulder at about 600°C. These observations could be interpreted as follows: until ~ 560°C the oxygen loss is negligible while V₂O₅ already starts to sublime at around 500°C. However, at ~ 590°C a significant loss of oxygen probably accompanied by a structural transition occurs, resulting in a sharp O₂ desorption peak. The resulting reduced phase sublimates/decomposes at a slightly higher temperature than V₂O₅, giving rise to the high temperature shoulder at 600°C. This phase might consist of V₆O₁₃, which would form via a lattice shear-plane

mechanism². Since the sublimation of the $V_2O_5(001)$ layer starts at a lower temperature than the structural transition, one can expect that for smaller thicknesses the sublimation of the $V_2O_5(001)$ layer will be complete before the transition can take place. This seems to be the case for the film produced from 5.2 MLE V. Indeed, as seen in Figure 4.19 the first broad V_xO_y desorption peak has already lost all its intensity at 600°C and does not have a clear high temperature shoulder. Concomitantly, the 590°C O_2 desorption peak is very weak.

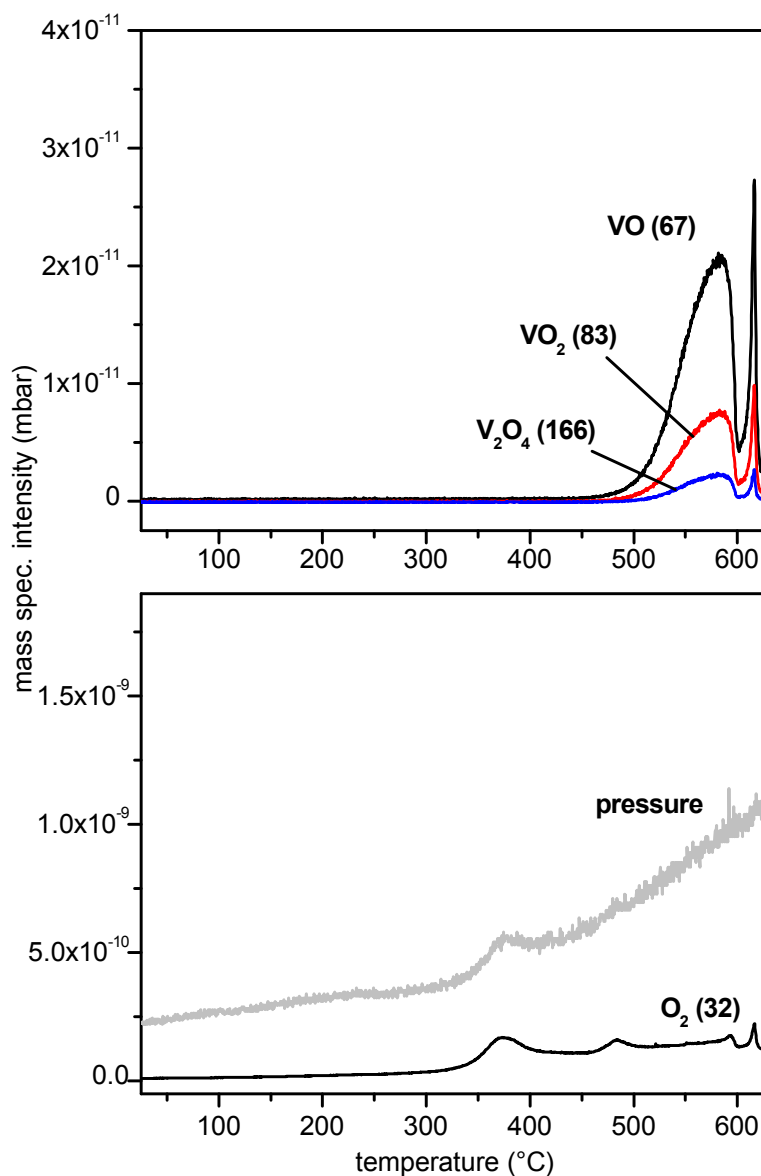


Figure 4.19. TPD of a $V_2O_5(001)$ film formed by the oxidation of 5.2 MLE V/Au(111). The evolution of the main chamber pressure during the TPD run is displayed in the lower graph.

The rest of the V_xO_y desorption peaks seen in Figure 4.18 (610°C – 660°C) can possibly be assigned to the decomposition/desorption of the interface film, which is an oxide double-

layer. This is supported to some extent by the *monolayer* film TDS shown in Figure 4.20 (film formed by the oxidation of 0.26 MLE V), which shows a single wide V_xO_y desorption peak at $\sim 645^\circ\text{C}$. This roughly corresponds to the position of the last peak observed in the V_xO_y desorption curves shown in Figure 4.18. The sharp desorption peak observed at 616°C might be related to the second layer. Reduced species formed during the oxygen release at 590°C can also contribute to some of the desorption intensity observed between 610°C and 660°C .

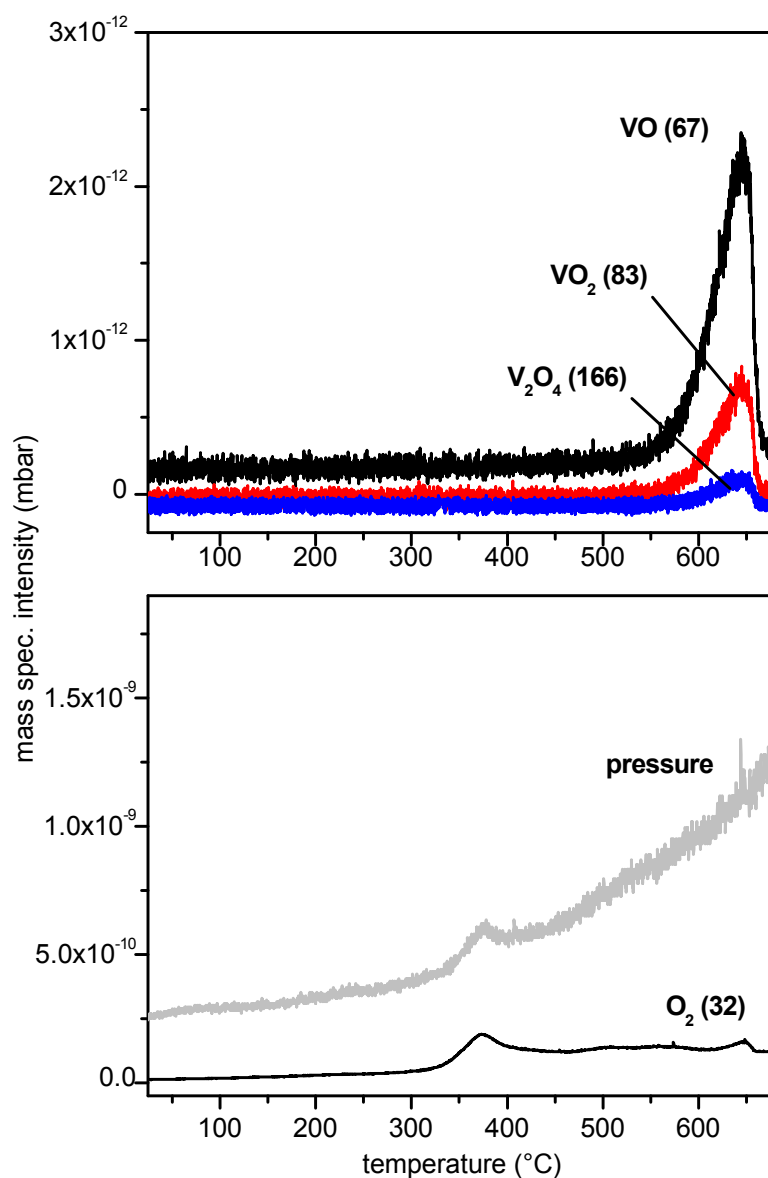


Figure 4.20. TPD of a film formed by the oxidation of 0.26 MLE V/Au(111). The evolution of the main chamber pressure during the TPD run is displayed in the lower graph.

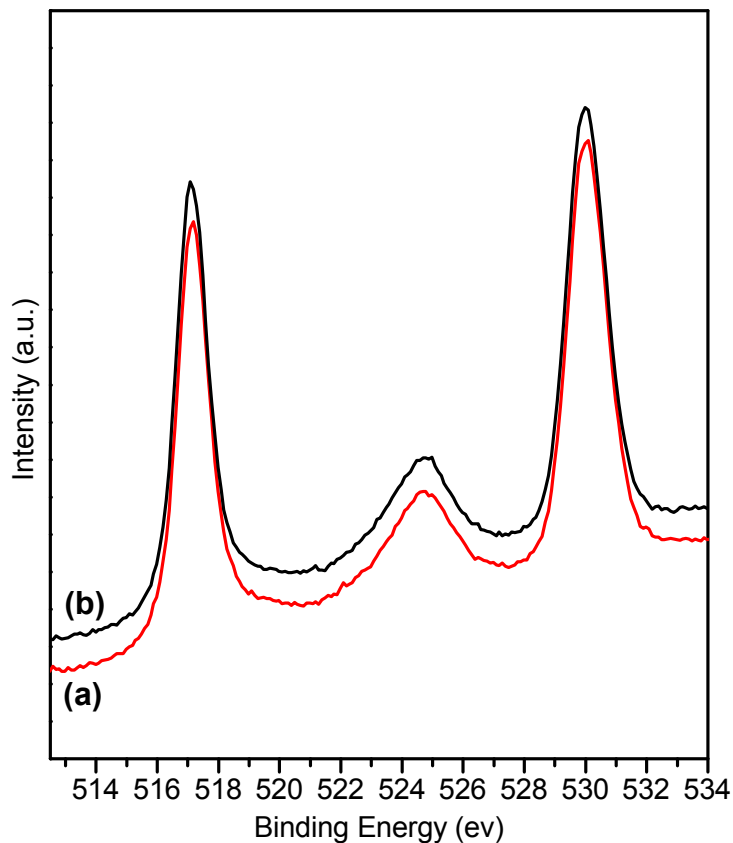


Figure 4.21. XP spectra (V2p and O1s region) obtained after preparation (a) and following 5 minutes of annealing in UHV at 450°C (b) for a film formed by 2 cycles of deposition and oxidation of 2.6 MLE V/Au(111). The spectra have been shifted with respect to each other in the y direction.

For all films, XPS revealed that after heating to 680°C no vanadium (or barely detectable quantities) remains on the Au(111) surface. This observation leads to the conclusion that no significant amount of V_2O_3 is formed during the desorption, since V_2O_3 is stable up to about 750°C in UHV²⁸ and would remain on the surface after TPD.

Concerning the removal of oxygen from the thick V_2O_5 films, our results correspond quite well to the TPD data reported by Dziembaj and by Lewis *et al*¹⁰⁹⁻¹¹¹. Dziembaj's experiments were carried on V_2O_5 powders that were previously degassed and re-oxidized *in-situ*, while Lewis *et al* investigated micron-sized V_2O_5 crystallites that were grown on a gold foil by V_2O_5 evaporation and subsequently fully oxidized in air. In both cases, the release of O_2 was observed to start *slowly* around 450°C – 500°C before an intense peak begins to appear at about 550°C. The observation that only slight oxygen loss takes place below 550°C – 560°C also corresponds to the findings of Colpaert and coworkers¹³. In their experiments on

V_2O_5 single crystals cleaved in-situ, they observed that after heating at 550°C for 24 hours the samples had lost some oxygen, but no structural transition to a lower oxidation state could be detected with either LEED or X-ray diffraction.

A number of studies have been reported on the reduction of V_2O_5 in UHV and, although the results of the investigations mentioned above agree very well with our findings, other studies came to various different conclusions. Actually, several authors reported that the reduction of V_2O_5 occurs at much lower temperatures. For instance, Heber and Grünert observed the formation of substantial amounts of V^{4+} species at the surface of polycrystalline V_2O_5 with XPS after annealing at temperatures as low as 200°C ¹¹². More recently, Wu *et al* also observed a partial surface reduction of evaporated V_2O_5 thin films to V^{4+} at 200°C ¹¹³. Their photoelectron spectra even revealed the formation of V^{3+} at 400°C . In both communications, no information concerning the possible formation of crystalline structures of lower oxidation states were reported. In another study, Devriendt and coworkers probed the surface of $V_2O_5(001)$ single crystals annealed at 500°C with LEED, XPS and X-ray photoelectron diffraction (XPD) ¹¹⁴. They concluded that $V_6O_{13}(001)$ forms at the surface under those conditions. Only V^{5+} and V^{4+} species were detected with XPS, excluding the presence of V^{3+} at the surface. The thermal reduction of V_2O_5 in UHV has also been investigated with transmission electron microscopy (TEM) by several groups. Su and Schlögl investigated tiny V_2O_5 flakes with TEM and electron energy-loss spectroscopy (EELS) ¹¹⁵. Their samples were already slightly reduced after heating to 200°C . The EELS spectra and the diffraction patterns indicated a phase transformation into V_2O_3 via VO_2 : VO_2 was observed at 400°C , a mixture of VO_2 and V_2O_3 was identified at 500°C , and only V_2O_3 remained at 600°C . Ramana *et al* did not observe the formation of reduced phases below temperatures of 450°C during their TEM investigation of thin films grown by evaporation of V_2O_5 ¹¹⁶. However, at 500°C they identified a phase containing mainly V_2O_5 and smaller amounts of V_2O_3 (V^{3+}) and V_4O_9 (a superstructure with O vacancies in the V_2O_5 lattice ²). After heating at 600°C , only V_2O_3 nanocrystals were seen to remain. However, the authors acknowledged that in their case the thermally-induced reduction process might have been aided by electron-beam induced reactions.

From the examples mentioned above, it is obvious that the results on the reduction of V_2O_5 (including both the reduction onset temperature and the observation of structural transitions) vary significantly from one study to the other. This might originate from several complications. First, the presence of surface contamination has been shown to have a critical influence on the reduction process ^{13,111}. Colpaert *et al* detected a significant quantity of carbon contamination at the surface of single crystals that were cleaved in air (not cleaved in the

UHV system)¹³. Reduction and a structural transition to V_6O_{13} was observed at the surface of these samples after annealing at 550°C, whereas the carbon-free surface of UHV-cleaved samples retained the V_2O_5 structure after the same thermal treatment (only a “homogeneous” oxygen loss was observed). The difference was attributed to a faster reduction rate at surfaces contaminated with carbon (likely through the formation and desorption of CO and CO₂). If this rate is high enough with respect to the bulk diffusion of O towards the surface, a critical concentration of vacancies can be reached, allowing the nucleation and the growth of V_6O_{13} at the surface through a shear-plane mechanism. Lewis and coworkers also evidenced the fact that the reduction of V_2O_5 is facilitated by the presence of hydrogen atoms or carbon-containing species¹¹¹. Oxygen loss through desorption of water was observed at about 150°C for surfaces dosed with activated hydrogen. After ethanol adsorption (which was only possible at relatively high exposures), CO and CO₂ were released upon heating around 400°C. Thus, the surface of contaminated samples will obviously get reduced at lower temperature. In some case, this effect might be even more pronounced since it is foreseeable that V_2O_5 powders and crystals might get bulk-contaminated depending on how they were produced, handled or stored. Indeed, V_2O_5 has a crystal structure containing rather large cavities and it is a material that displays good intercalation properties¹¹⁷, thereby possibly allowing the inclusion/diffusion of various impurities in its lattice.

Another factor that might partly explain the variance between some of the reduction studies is the marked susceptibility of V_2O_5 to beam damage. As mentioned before, both X-ray¹⁵ and electron beams¹³ have been shown to rapidly reduce vanadium pentoxide. In the case of TEM investigations, it thus seems that the contribution of electron beam-induced processes to the observed reduction behavior cannot be fully neglected. Similarly, studies where the samples were exposed to high X-ray doses should be considered with care. In fact, Chenakin *et al* showed that significant V^{4+} intensity appears in the V2p XPS signal of V_2O_5 after prolonged Mg K α exposure¹⁵.

Even though the reduction experiments mentioned above were carried out with considerably different annealing times, it seems that kinetic factors alone can not explain the divergence of the results. A clear example supporting this affirmation is the fact that Colpaert *et al* did not observe significant reduction after annealing 24 hours at 550°C, while Wu *et al* reported the formation of V^{3+} following only 1 hour of heating at 400°C.

The observation that V_2O_5 starts to sublime at about 500°C in UHV is an interesting result in itself (V_2O_5 has been reported to melt at about 670°C in ambient conditions^{118,119}). Details investigations about the sublimation of vanadium pentoxide in vacuum have not been

reported yet. Several V_xO_y -type molecules vaporizing from V_2O_5 heated in a Knudsen cell were detected by mass spectrometry by Berkowitz *et al*¹²⁰. However, the authors did not report at which temperature the material was heated in the Knudsen cell. Farber and coworkers also performed an effusive-mass spectrometric study of the gaseous vanadium compounds evolving from V_2O_5 , but their investigated temperature range was limited to 730°C – 930°C¹²¹. One also has to mention that the sublimation of V_2O_5 was not taken into account in any of the studies on the thermal stability mentioned previously. A conclusion that can be drawn from the results presented here is the fact that V_2O_5 can sublime before substantial reduction takes place (provided of course that low temperature reduction due to contamination is avoided). This means that in principle, near-stoichiometric films could be grown by the evaporation of V_2O_5 under vacuum. Of course, the evaporation temperature must be kept below the limit where significant reduction occurs ($\sim 560^\circ\text{C}$), a condition that most probably severely restrains the achievable evaporation rate. In previous works, much higher evaporation temperatures were sometimes used (for example, 670°C ¹¹³ and 840°C ⁶⁶). In these cases, it is not very surprising that the resulting films were not fully oxidized and contained some V^{4+} species.

4.4 Summary

The results presented in this chapter show that well-ordered V_2O_5 films can be formed on Au(111) by the oxidation of vanadium in 50 mbar O_2 . At very low V coverage, the oxidation leads to a spreading of the material on the Au(111) substrate and to the formation of monolayer structures with a V^{5+} oxidation state. Two well-ordered coincidence layers that do not correspond to any known bulk structures have been observed. These results evidence the fact that due to the easy rearrangement of VO_5 units in V^{5+} oxides, a complicated range of interface-mediated monolayer structures can be obtained. It can be predicted that if monolayers form on other substrates like SiO_2 , Al_2O_3 , TiO_2 , etc under similar preparation conditions, they will adopt rather different structures for every substrate. This goes along with the findings of Gao *et al* who investigated the growth of vanadium oxide on the (101) and (001) surfaces of anatase^{122,123}. On the two surfaces, they have obtained different epitaxial V^{5+} oxide monolayers. Obviously, the structural dependence of vanadium oxide monolayers on the supporting material should be taken into account when comparing, for instance, the reactivity of thin films supported on various oxides.

The results also show that a two layers-thick wetting film having a structure different from that of bulk V_2O_5 can be grown under preparation conditions (temperature, O_2 pressure) suitable for the formation of V_2O_5 . This finding is rather interesting because it is in contrast with a rather generally accepted idea in the catalysis literature, where V_2O_5 crystallites are often assumed to start forming as soon as a monolayer is completed⁴. The onset of V_2O_5 crystallites formation as a function of loading is often detected with Raman spectroscopy (monitoring bands pertaining to crystalline V_2O_5), and the result is used to calculate the monolayer coverage in VO_x units per nm^2 . Doing so, the possibility that thicker films might form before V_2O_5 crystallizes is disregarded. Our results suggest that such analyses should be considered with more caution.

Well-ordered $V_2O_5(001)$ thin films containing a low density of point defects can be grown on Au(111) by the oxidation of thicker vanadium layers in 50 mbar O_2 . Although the films display some azimuthal disorder their surface shows rather large (~ 20 nm) single crystalline domains and a low density of steps (i.e. the films are “flat”). The growth of such well-ordered $V_2O_5(001)$ thin films with a rather simple technique is interesting and of considerable advantage for the undertaking of model reactivity studies.

The $V_2O_5(001)$ films sublime at temperatures above $500^\circ C$, whereas significant reduction does not take place until $560^\circ C$ and no oxygen loss was detected below $450^\circ C$. Surface contamination appears to drastically influence the thermal reduction of V_2O_5 . Considering that V_2O_5 is used as a catalyst because of its ability to transfer oxygen to adsorbed molecules, this is not very surprising.

The susceptibility of V_2O_5 towards X-ray or electron irradiation has also been evidenced in the course of the present investigations. The creation of surface vanadyl oxygen vacancies after exposure to X-rays has been probed with STM. The results confirm theoretical predictions¹⁰² that the reduction occurs in a concerted way, the vacancies preferentially appearing in groups (forming rows along [010] and/or pairs along [100]).

5 Growth of MoO₃ thin films

5.1 Introduction

Following the success obtained in the preparation of well-ordered V₂O₅ thin films (Chapter 4), the high pressure oxidation approach was applied to the formation of thin films of another transition metal oxide, MoO₃. Molybdenum trioxide is the compound with the highest Mo oxidation state in the Mo – O system. Interesting comparisons can be made between vanadium pentoxide and molybdenum trioxide because these two compounds are characterized by similar structure and reactivity. Not surprisingly, their fields of application are also comparable. Like V₂O₅, MoO₃ is an oxide of high industrial relevance.

Molybdenum trioxide is extensively used as a key component in mixed oxide catalysts (see for instance refs. ^{1,3}). Very good examples are iron-molybdate catalysts, which are industrially used (beside, or in combination with silver-based catalysts) for the selective oxidation of methanol to formaldehyde ³. Formaldehyde is a very important building block for the chemical industry (for instance, for the production of thermosetting resins). As for vanadium-oxide based catalysts, important questions regarding the nature of the active sites and the reaction mechanisms at the surface of iron-molybdate catalysts are not clearly answered yet. However, many evidences point toward the fact that Mo plays the major role in the relevant catalytic reactions occurring on these compounds ³. This is in part substantiated by the observations that MoO₃ alone shows a rather good activity for several reactions, including the oxidation of methanol to formaldehyde ¹²⁴ and the partial oxidation of propene ¹²⁵. Well defined molybdenum oxide surfaces are therefore relevant models for investigating reaction steps that might occur on the technical mixed oxide catalysts and such surfaces have been receiving substantial attention in the past (see ref. ¹ and references therein). Like in the case of V₂O₅, the possibility of growing well-ordered MoO₃ thin films would have some practical advantages over the use of single crystals and this was investigated in this study.

Beside their relevance to catalysis, MoO₃ thin films have also other rather promising potential applications. Similar to V₂O₅, the possible intercalation of alkali ions in the orthorhombic crystal structure of MoO₃ (see below) makes this material a good candidate for the production of micro-batteries and electrochromic materials (stoichiometric and intercalated MoO₃ being transparent and colored, respectively) ^{126,127}. Specifically, the intercalation process can be controllable and reversible and MoO₃ has a relatively high stability in air. MoO₃ also has interesting photochromic properties and shows a reversible UV radiation induced

color change: Mo^{6+} species are partially reduced to Mo^{5+} under UV irradiation and the material is reoxidized upon exposure to the atmosphere¹²⁸.

The most common polymorph of MoO_3 is the orthorhombic α -phase¹, with unit cell parameters $a = 3.9628$, $b = 13.855$ and $c = 3.6964$ Å¹²⁹. A monoclinic β -phase was also observed at high pressure¹, but this polymorph is rather uncommon and will not be described here. The atomistic structure of α - MoO_3 is depicted in Figure 5.1. It consists of weakly interacting bilayer sheets that are aligned parallel to the (010) plane. Each bilayer is built-up by two interleaved planes of corner-sharing MoO_6 octahedra. The octahedra of the two adjacent planes are sharing edges. The octahedral MoO_6 building unit is severely distorted and the metal-oxygen bond lengths vary between 1.68 Å and 2.33 Å. The longest bond length refers to the oxygen centers that are shared by neighboring octahedra of the two adjacent planes ($O3$ in Figure 5.1 (b)) and the shortest corresponds to the terminal oxygen atoms at the top and the bottom of the bilayers ($O1$ in Figure 5.1 (b)). As indicated in Figure 5.1 (b), α - MoO_3 contains three structurally different oxygen sites^{1,10,11}: terminal oxygen coordinated to only one Mo center ($O1$) and bridging oxygen atoms coordinated to two ($O2$) or three ($O3$) Mo centers. The terminal oxygen can be considered to form a double bond with its adjacent Mo center. This molybdenyl group ($\text{Mo}=\text{O}$) is a structural element characteristic of MoO_3 . The interatomic binding in MoO_3 has both ionic and sizeable covalent contributions^{1,11}. Indeed, the valence and conduction bands of MoO_3 have contributions from both oxygen 2p and molybdenum 4d levels. Also, the calculated Mo charge (between $2.23+$ ¹¹ and $2.59+$ ¹⁰, depending on the calculation methodology) is much smaller than the formal charge expected for pure ionic binding (6+). Since the adjacent bilayers along [010] are linked only by weak van der Waals forces, (010) is the easiest cleavage plane for α - MoO_3 .

Obviously, the structure of α - MoO_3 has many features in common with V_2O_5 (e.g. the arrangement of corner- and edge-sharing MO_6 octahedra and the weakly interacting layers that expose molybdenyl groups). Another notable similarity is the formation of mixed valence oxides and crystallographic shear planes upon the successive reduction of MoO_3 (to MoO_2)¹. These crystallographic transformations involve a connectivity shift of the MoO_6 octahedra (from corner-sharing to edge-sharing) and result in the homologous series $\text{Mo}_n\text{O}_{3n-1}$ and $\text{Mo}_n\text{O}_{3n-2}$. Like for V_2O_5 , the catalytic activity of MoO_3 is often described by a redox mechanism of the Mars-van Krevelen type¹⁹, where the catalyst acts as a renewable oxygen source. Here, the relative “open” crystal structures of V_2O_5 and MoO_3 most probably play a favorable role in facilitating oxygen diffusion, both from the bulk volume to the surface to annihilate vacancies and from the gas phase to the bulk to replenish the overall O content.

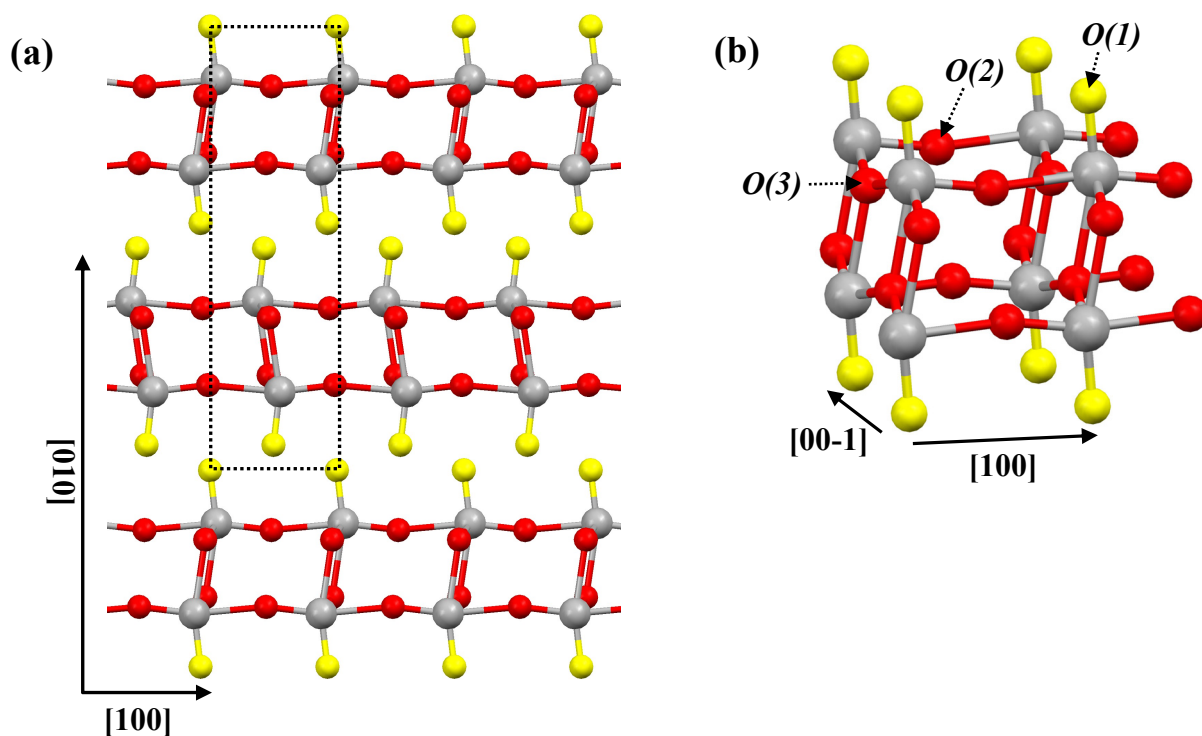


Figure 5.1. α - MoO_3 geometric structure¹²⁹. (a): view of the structure along $[001]$ showing the stacking of the double layers in the $[010]$ direction. (b): magnified and tilted view showing the structural details in a double layer. Gray spheres indicate the position of the molybdenum atoms while yellow and red spheres pertain to oxygen atoms (yellow indicating molybdenyl O atoms). The elementary unit cell is shown in (a) and the non-equivalent oxygen centers, $O(1, 2, 3)$, are labeled accordingly in (b).

The formation of molybdenum trioxide thin films was investigated for a broad range of deposition methods, including thermal evaporation of MoO_3 ^{127,130}, reactive pulsed laser deposition¹³¹, spin coating using peroxo-molybdc precursors¹³² and hot filament metal oxide deposition¹²⁶. Most of these studies were focused on growing micrometer- or sub micrometer thick MoO_3 films suitable for intercalation devices (e.g. micro-batteries or electrochromic applications), an application where the precise control of the surface structure does not play a big role or at least was not considered as being very important. Reports reveal that the MoO_3 thin films deposited at low substrate temperatures ($T < 100^\circ\text{C}$) are usually amorphous. In these cases, post-deposition annealing in O_2 atmosphere at $T > 250^\circ\text{C}$ was necessary to crystallize the films. Julien *et al*¹²⁷ and Gaigneaux *et al*¹³² also reported that the crystallites obtained after annealing preferentially expose (010) basal faces, which are mainly aligned parallel to the substrate surface. Unfortunately, the characterization of the films in the above-mentioned studies were almost always carried-out *ex-situ* and involved exposing the sample to air prior to (or during) the analysis. This certainly prevents a clear determination of the thin

film stoichiometry right after deposition (i.e. *in-situ*, under reduced pressure), since exposure to air can increase the oxidation of the film and heal O-vacancies¹³³. This particularly applies to the determination of the film oxidation state using surface sensitive techniques like XPS. In the case of model systems used to study catalytic processes, where the surface should be controlled at the atomic scale, it is desirable to avoid contact to air in order to prevent the adsorption of adventitious contaminations like hydrocarbons or water. The adsorption of water on MoO₃ thin films exposed to air, possibly accompanied by the formation of hydroxyl groups, was reported by Moraes and coworkers¹²⁶, for instance. To avoid this effect, a possible approach could be to prepare the films directly in the UHV system where the surface and reactivity studies will be carried-out. However, the oxidation of bulk molybdenum under UHV-compatible O₂ pressures ($< 10^{-3}$ - 10^{-4} mbar) rather typically results in the formation of MoO₂ surface layers¹³⁴⁻¹³⁷. The presence of higher oxidation states is also sometimes reported after extensive annealing in O₂ partial pressure, but these species (perhaps polymolybdates) are disordered and occur in rather small quantities^{134,135}. Indeed, it is believed that MoO₃ more or less desorbs as it is formed under these UHV-compatible oxidation conditions (the necessary oxidation temperature being higher than the temperature at which MoO₃ sublimates)¹³⁴. S. Bourgeois, B. Domenichini and coworkers investigated the possibility of oxidizing very thin layers of Mo deposited on TiO₂(110) by subsequent annealing in UHV (see ref.¹³⁸ and references therein). Their work shows that oxygen atoms from the TiO₂ substrate can diffuse to the Mo thin layer and produce MoO₂ thin films or clusters. They have also observed that if the annealing is carried out at higher temperature, MoO₃ can be formed and it then immediately sublimates.

Under these circumstances, it appears that the high pressure cell oxidation method described in section 2.1.3. and used successfully for the preparation of V₂O₅ thin films (see Chapter 4) could also be appropriate for the preparation of MoO₃ thin films. Similar to the investigations presented in Chapter 4, various amounts of Mo were oxidized in order to study the formation of MoO₃ films of different thicknesses.

5.2 Preparation Method

The films were prepared by first evaporating Mo on Au(111) and then transferring the sample in the high pressure cell attached to the UHV chamber for oxidation. Mo was evaporated with an Omicron EFM3 e-beam evaporator at a rate of about 0.4 Å/min (0.2 MLE/min) while the substrate was held at room temperature. Different Mo amounts were deposited in order to vary the thickness of the resulting oxide films. Mo thicknesses are reported here in monolayer equivalents (MLE), where 1 MLE contains the same number of Mo atoms as one layer of Au(111) ($\sim 1.39 \times 10^{15}$ atoms/cm²). The evaporated Mo layers were oxidized by heating the sample under an oxygen flow at a constant pressure of 50 mbar in the high pressure cell. The sample temperature was allowed to cool down to about 100 °C before pumping down the high pressure cell and transferring the sample back to the main chamber. After oxidation of the films, no traces of surface contamination could be detected with XPS.

Initial experiments were done to determine at which temperature the Mo films are fully oxidized to MoO₃ under these conditions (for a reasonable annealing time, i.e. less than 1 hour). Some of the results obtained during these tests are summarized in Figure 5.2. The graphs show a series of Mo3d XPS spectra obtained for a relatively thick film annealed in the high pressure cell at different temperatures under 50 mbar O₂. The annealing steps were done in a sequence, starting at 150°C and going up to 500°C. The series of spectra is separated in two graphs for clarity. The film was initially prepared by evaporating 45 Å Mo (~ 20 MLE) in 5×10^{-6} mbar O₂ (this was initially done in an attempt to grow a MoO₂ thin film). The corresponding Mo3d spectrum is displayed as the black curve in the left panel of Figure 5.2. It shows two distinct peaks at 229.2 eV and 232.3 eV, which roughly correspond to the Mo3d_{5/2} and Mo3d_{3/2} levels observed for MoO₂, respectively^{136,139}. The spectrum also reveals a clear shoulder at about 234.4 eV, indicative of the presence of some higher oxidation state species at the surface. These observations correspond very well with the findings of other groups for the oxidation of Mo in oxygen partial pressures in the 10⁻⁶ mbar range^{134,135}. After the annealing steps at 150°C, 250°C and 300°C the overall Mo3d envelope is gradually shifted towards higher binding energy as the average oxidation state of the film increases. A peak structure characteristic of pure MoO₃ - with a Mo3d_{5/2} binding energy of ~ 232.65 eV and a spin-orbit splitting of ~ 3.2 eV¹³⁹ - is however only reached after the annealing step at 350°C. One can then conclude that an annealing temperature higher than 300°C is necessary to fully oxidize the thin films. The XPS spectrum did not change after the subsequent annealing step at 400°C (the two curves are actually almost undistinguishable). Some Mo3d intensity was lost after annealing at 450°C and a drastic decrease of the peak area is observed after the 500°C step.

This would point toward an evaporation of the MoO₃ film at 450°C and temperatures above in the high pressure cell. This conclusion is supported by the TPD data presented below (section 5.3.3) and corresponds well to the results reported in the literature¹⁴⁰. In light of these results, an annealing temperature of 400°C was used for most of the preparations. This makes sure that the film is fully oxidized (for the Mo thicknesses used here) and avoids losses due to evaporation of the material. Interestingly, a residual but constant Mo3d intensity was detected after extended annealing at 500°C. The presence of this residual MoO₃ layer was accompanied by a well-defined c(4x2) LEED pattern and it is attributed to a molybdenum oxide single layer on the Au(111) substrate (see below), a layer that apparently has a higher evaporation temperature than the rest of the film.

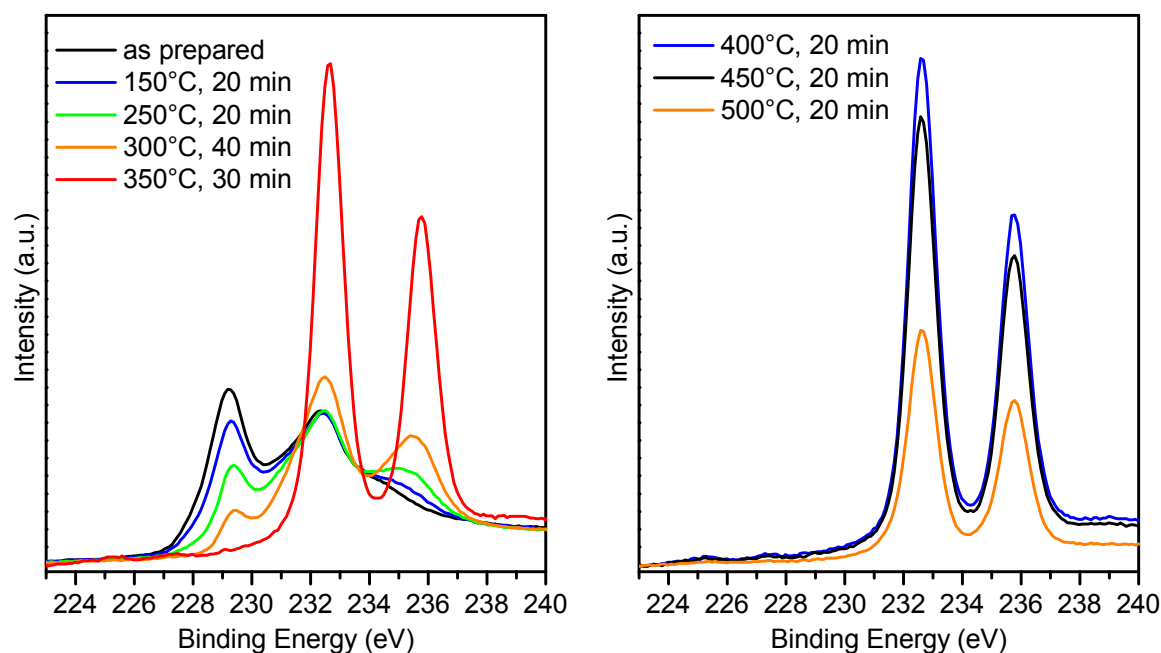


Figure 5.2. Mo3d XPS spectra of a MoO_x film obtained after several annealing steps in 50 mbar O₂. Annealing steps are done sequentially, going from 150°C up to 500°C. Film prepared by evaporating 45 Å Mo in 5×10^{-6} mbar O₂. The XPS intensity was normalized to the background intensity at 210 eV for all spectra. Mg K α , $\theta = 0^\circ$.

5.3 Results and discussion

Similar to growth of V₂O₅ on Au(111) (see Chapter 4), different surface structures were observed as a function of the thin film thickness for the oxidation of Mo on Au(111). Whereas α -MoO₃ was obtained for thicker films, the oxidation of very low amounts of Mo led to the

formation of well-ordered overlayers with structures that do not correspond to any known bulk molybdenum oxide crystal structures. Like in Chapter 4, the characterization of these “interface specific” layers is first described and discussed. This is then followed by the description of the thicker films and by a discussion on the thermal stability of the films under UHV.

5.3.1 Structure of the first layers

The oxidation of molybdenum deposits with a thickness up to about 0.5 MLE in 50 mbar O₂ at 400°C resulted in the formation of a flat film with a c(4x2) unit cell. STM and LEED results corresponding to a film formed by the oxidation of 0.46 MLE Mo are shown in Figure 5.3. The large area (300 nm x 300 nm) STM image shown in (a) clearly indicates that the oxide forms a smooth, uniform film on the Au(111) substrate. A similar observation was made for the very thin V₂O₅ layers (c.f. section 4.3.1.), where the V nanoclusters present on the Au(111) surface after V evaporation were transformed into an extended oxide monolayer after oxidation. This likely implies the transport of MoO_x species on the substrate’s surface during the oxidation procedure. As for the V₂O₅ layers, factors influencing the spreading of the oxide and the formation of a monolayer include: the easy rearrangement of coordination units in molybdenum oxides, electronic interaction with the substrate and the surface free energy difference between Au(111) and MoO₃, the latter being almost two orders of magnitude lower⁹². Areas where the substrate surface is still exposed are marked with an asterisk on the picture. These generally appear smoother and they are easily identified by the observation of the Au(111) herringbone reconstruction zigzag pattern at higher resolution. One can observe that most of the substrate is covered by the film (also from other images taken at various places on the sample surface). High resolution STM pictures like the one shown in Figure 5.3 (b) reveal a well-ordered structure with a 5.8 Å x 5 Å rectangular unit cell (indicated by the grey rectangle on the image). Only a limited number of point defects could be observed with STM. However, it should be mentioned that the STM imaging of the Mo oxide thin films was particularly difficult and rather few atomically-resolved pictures could be obtained. This is probably due to the insulating nature of the oxide; see the discussion for the thicker films below. Nevertheless, judging from the sharpness of the spots in the LEED pattern shown in Figure 5.3 (c), the film must have a rather good long-range order. The LEED pattern could be successfully reproduced using a 5.77 Å x 5 Å rectangular unit cell and using three rotational domains to take the substrate’s 3-fold symmetry into account. With respect to the Au(111) substrate, this corresponds to a c(4x2) overlayer (see Figure 5.4.).

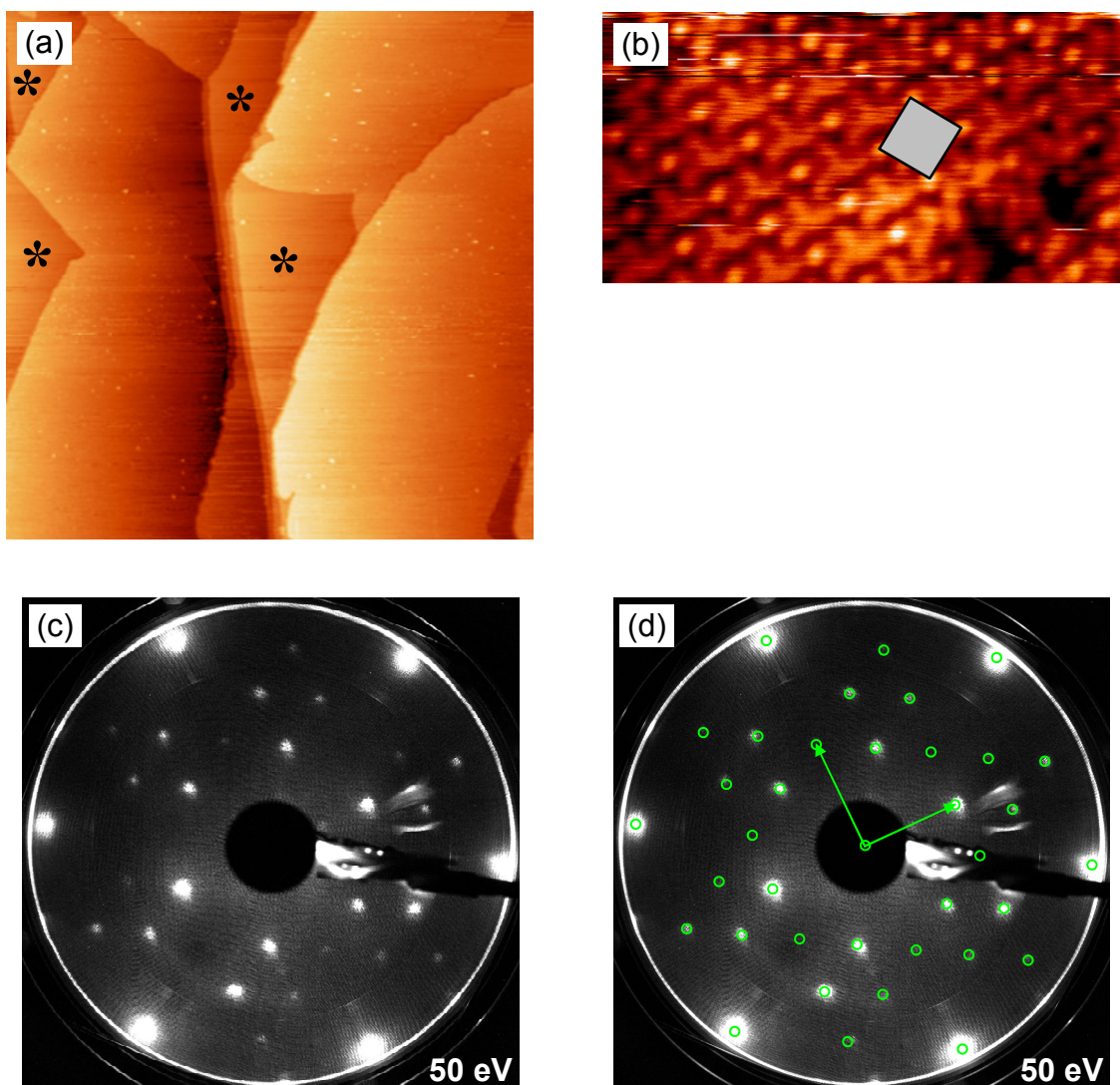


Figure 5.3. STM images ((a): 300 nm x 300 nm, 2.5 V, 0.2 nA, (b): 5 nm x 2.56 nm, 2.5 V, 0.2 nA) and LEED pattern (c) obtained after annealing 0.46 MLE Mo/Au(111) in 50 mbar O₂ at 400°C for 10 minutes. (d): Reproduction of the LEED pattern using a 5.77 Å x 5 Å rectangular unit cell and taking into account the substrate 3-fold symmetry (the bright spots at the border of the screen also correspond to the Au(111) (10) spots). Exposed Au(111) areas are marked with * in (a).

The same $c(4 \times 2)$ superlattice on Au(111) has been observed by Biener and coworkers after the oxidation of Mo nanoclusters (deposited either by CVD of Mo(CO)₆ or Mo evaporation) with NO₂^{92,141}. This structure was investigated in details and an atomistic model was proposed based on DFT calculations⁹⁴. This model is reproduced in Figure 5.5. The film is a MoO₃ monolayer composed of MoO₅ squared pyramids. These coordination pyramids share the corners of their base (which lies on the substrate) and are tilting alternatively forwards and backwards relative to the surface normal (see Figure 5.5 (b)). The terminal oxygen atoms located at the apices of the pyramids (labeled O_{t1} and O_{t2}) form molybdenyl groups with the Mo

centers (Mo=O). Actually, the structure of the monolayer is rather similar to the one encountered in both layers forming the α -MoO₃ bilayers. Likewise, the monolayer surface is structurally not very different from MoO₃(010). However, in the monolayer the bond distances and angles are modified/distorted to fit the Au lattice. Bond angles differ as much as 11° from the bulk α -MoO₃ values. According to the calculations, the oxide monolayer polarizes the electron gas at the MoO₃/Au(111) interface, which leads to a charge redistribution. The Au surface then somehow serves as the other half of the bilayer and stabilizes the monolayer structure.

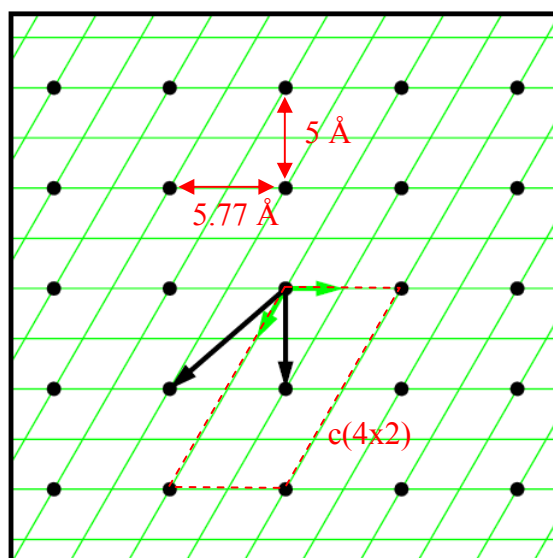


Figure 5.4. Real space representation of the c(4x2) structure. The green lines and the black dots correspond to the Au(111) substrate and the molybdenum oxide overlayer lattices, respectively. Image generated with the LEEDpat21 software¹⁴².

The Mo surface atom density in the c(4x2) monolayer is $\sim 0.7 \times 10^{15}$ atoms/cm², which means that an initial Mo coverage of about 0.5 MLE is in principle required to obtain a full monolayer. This is reflected to a good extent by the experimental results. Large area STM images obtained after the oxidation of 0.46 MLE Mo (Figure 5.3 (a)) indeed show that most of the substrate is covered by the oxide monolayer. The presence of defects in the film and of some residual disordered MoO_x species on top of the film (seen as bright spots on top of the oxide patches in Figure 5.3 (a)) could account for a slightly lower c(4x2) coverage than expected from the initial quantity of evaporated Mo. Also, the sublimation of a small amount of material during the oxidation cannot be totally ruled out.

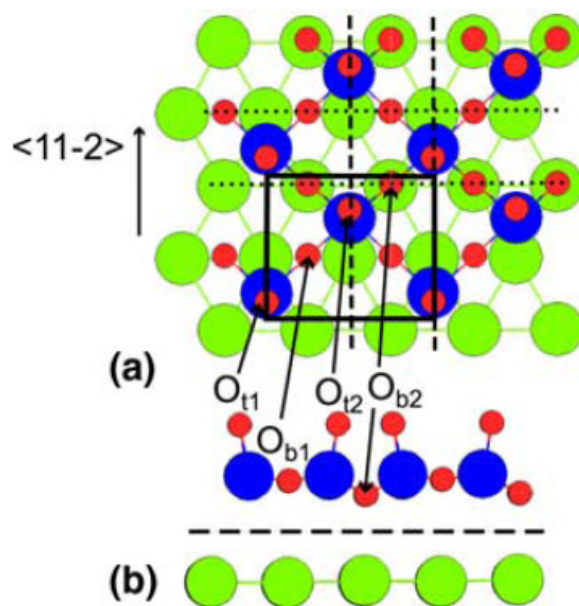


Figure 5.5. Atomistic model of the $c(4 \times 2)$ $\text{MoO}_3/\text{Au}(111)$ monolayer. (a) top view, (b) side view. The Mo, O and Au atoms are represented by blue, red and green circles, respectively. The $5.77 \text{ \AA} \times 5 \text{ \AA}$ rectangular unit cell in indicated by a black rectangle in (a). Image taken from ref. ⁹⁴.

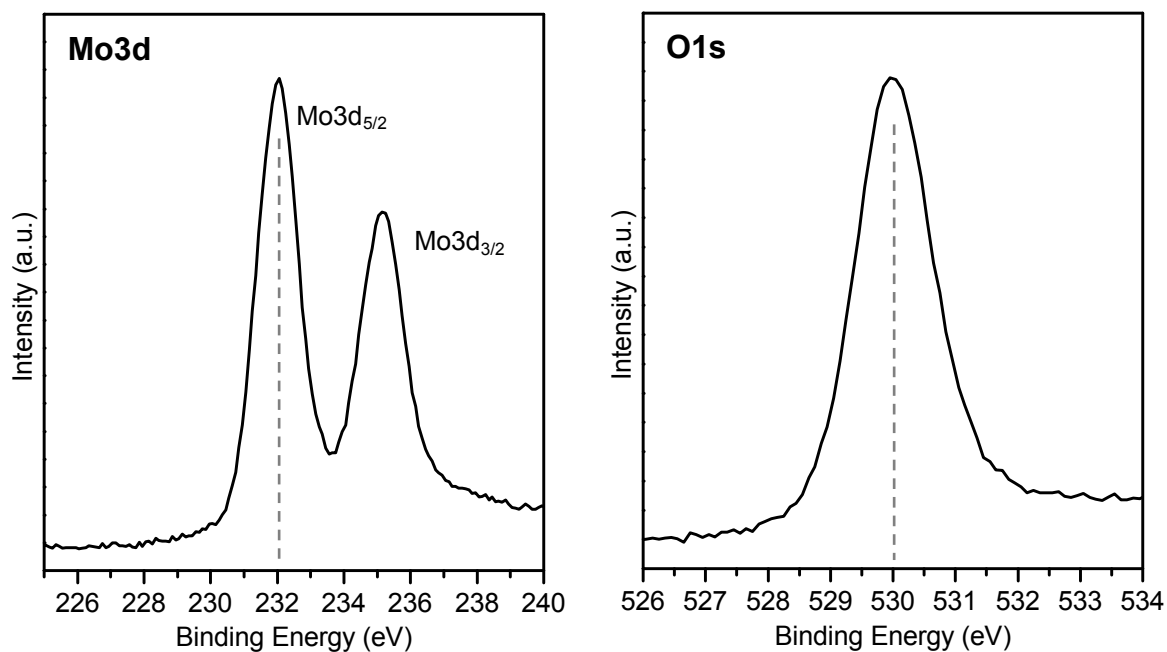


Figure 5.6. Mo3d and O1s XPS spectra of a $c(4 \times 2)$ monolayer obtained after annealing 0.46 MLE Mo/Au(111) in 50 mbar O_2 at 400°C for 10 minutes. Mg $K\alpha$, $\theta = 0^\circ$.

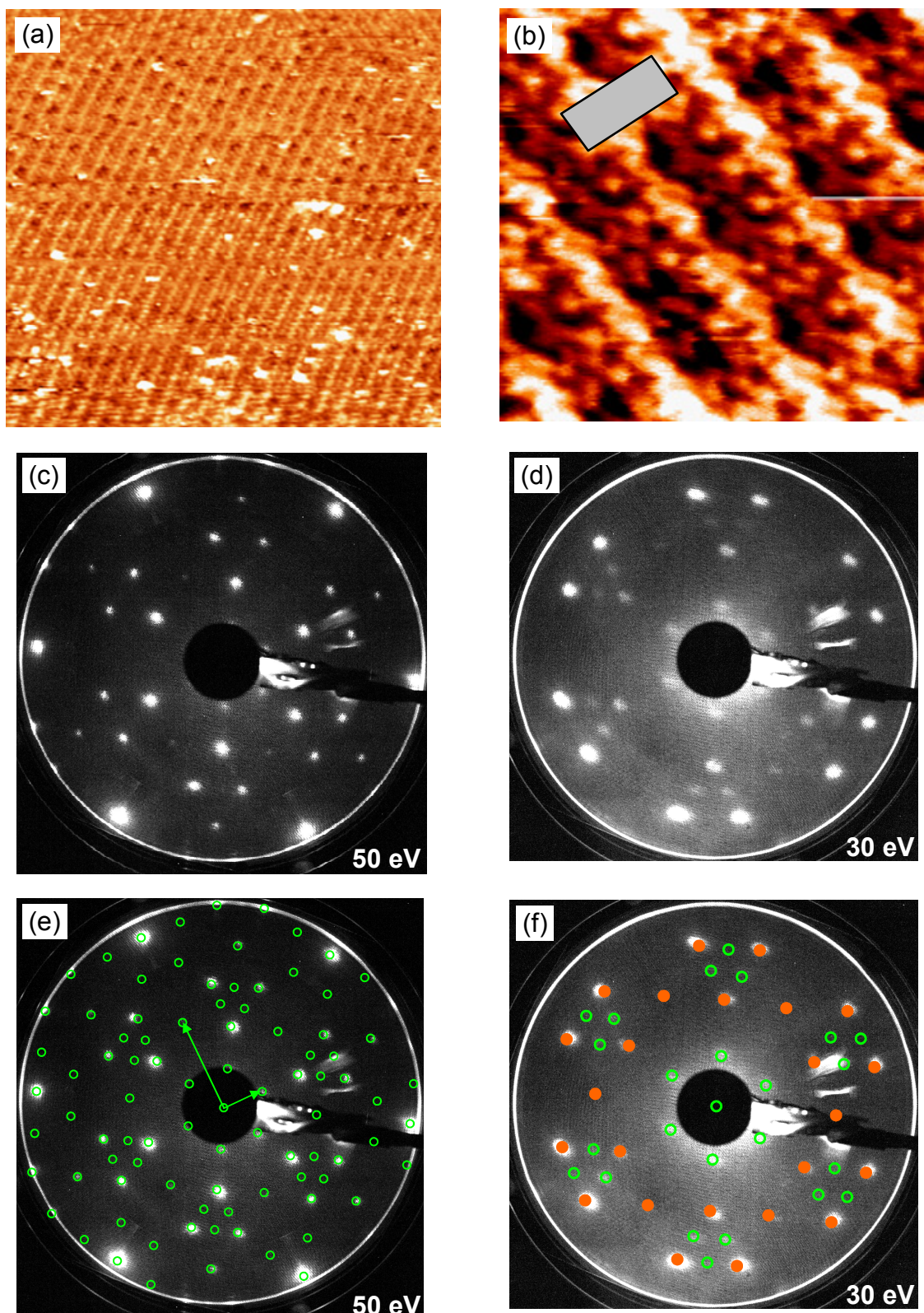


Figure 5.7. STM images ((a): 27 nm x 26.7 nm, 2.5 V, 0.2 nA, (b): 4.1 nm x 4.1 nm, 2.5 V, 0.2 nA) and LEED patterns (c, d) obtained after annealing 0.92 MLE Mo/Au(111) in 50 mbar O₂ at 400°C for 10 minutes. (e, f): Reproduction of the LEED patterns shown in (c, d) using a 11.6 Å x 5 Å rectangular unit cell and taking into account the substrate 3-fold symmetry.

Mo3d and O1s XPS spectra representative of the c(4x2) oxide monolayer are presented in Figure 5.6. The Mo3d_{5/2} and O1s peaks appear at binding energies of 232 eV and 530 eV, respectively. In comparison to α -MoO₃ (see ref. ¹³⁹ and section 5.3.2), both spectra are shifted by about 0.7 eV toward lower binding energy. Like for the V₂O₅ monolayer structures described in section 4.3.1, this shift can be attributed to a screening of the XPS final state core holes by the Au(111) electrons. Interestingly, about the same shift is observed for the monolayer of both oxides.

A surface structure with a larger unit cell was observed for the oxidation of slightly higher Mo thicknesses (between 0.69 MLE and 1.15 MLE). STM images and LEED patterns obtained after the oxidation of 0.92 MLE Mo (400°C, 50 mbar O₂, 10 minutes) are shown in Figure 5.7. Corrugation lines are observed in the large scale STM image shown in (a). Higher resolution images, although relatively noisy, also reveal a $\sim 11.5 \text{ \AA} \times 5 \text{ \AA}$ rectangular unit cell (see image (b)). Accordingly, the LEED patterns can be well reproduced by using a $11.6 \text{ \AA} \times 5 \text{ \AA}$ rectangular unit cell. The short unit cell vector of this surface structure has the same length as the one pertaining to the c(4x2) structure described above ($5.77 \text{ \AA} \times 5 \text{ \AA}$ unit cell), while the long unit cell vector has twice the length. As a result, the LEED patterns for the larger unit cell display the same reflexes as for the c(4x2) structure plus some extra spots. Comparing Figures 5.7 (c) and (e), it is obvious that not all the expected spots are present in the pattern recorded at 50 eV. Some of the spots appear and disappear as a function of the electron beam energy. As shown in Figures 5.7 (d) and (f), most of the expected spots can be observed at 30 eV. In Figure 5.7 (f), the spots that are also observed for the c(4x2) structure are identified with orange circles.

The XPS Mo3d and O1s spectra corresponding to this film (oxidation of 0.92 MLE Mo) are displayed in Figure 5.8. The binding energy of both peaks (Mo3d_{5/2}: 232.3 eV, O1s: 530.3 eV) is about 0.4 eV lower than those obtained for α -MoO₃. The difference between the XPS spectra obtained for this film and the c(4x2) monolayer is reminiscent of the observations made for the V₂O₅ thin films (Chapter 4). In this case, a shift to lower binding energy attributed to screening was observed for the monolayer while upon the formation of a second oxide layer the V2p_{3/2} and O1s peak maxima were found at positions much closer of those characteristic of bulk V₂O₅. It was then concluded that the screening effects are rather limited to the first oxide layer. It seems that the same phenomenon occurs for the thin MoO₃ layers, which is an indication that the observed $11.6 \text{ \AA} \times 5 \text{ \AA}$ rectangular unit cell is related to the formation of a second layer of MoO₃. This assumption is also motivated by the fact that 0.92 MLE is about twice the amount of Mo required to complete a full c(4x2) monolayer, see above. Aside

from these observations, the data presented here are not enough to determine more precisely and unambiguously the structure of this film. STM images with a better resolution, perhaps supported by some DFT calculations, would be required for this purpose. It is worth mentioning that a $c(4 \times 2)$ monolayer can be obtained if this thicker layer is annealed at substantially higher temperature in the high pressure cell. This is shown in Figure 5.9, where LEED and Mo3d XPS data are compared for 0.92 MLE Mo after a first oxidation step at 400°C (results taken from Figures 5.7 and 5.8) and a subsequent step at 500°C. The data obtained after the second annealing step correspond to a $c(4 \times 2)$ monolayer: the extra LEED spots corresponding to the $11.6 \text{ \AA} \times 5 \text{ \AA}$ unit cell have disappeared and the Mo3d peaks are shifted towards lower binding energy. This observation is consistent with results of the initial oxidation experiments (section 5.2) and it can be interpreted by considering that during the oxidation at 500°C the MoO₃ overlayers sublime (including the “second layer”), leaving behind a $c(4 \times 2)$ monolayer which is stable at this annealing temperature.

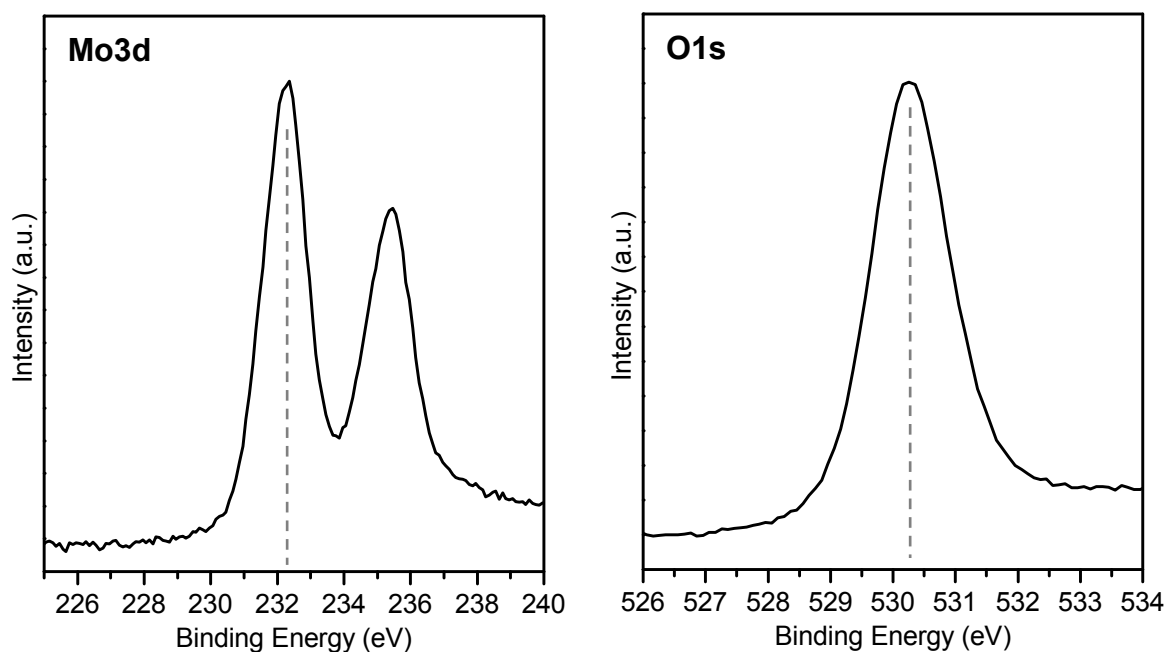


Figure 5.8. Mo3d and O1s XPS spectra of a film obtained after annealing 0.92 MLE Mo/Au(111) in 50 mbar O₂ at 400°C for 10 minutes. Mg K α , $\theta = 0^\circ$.

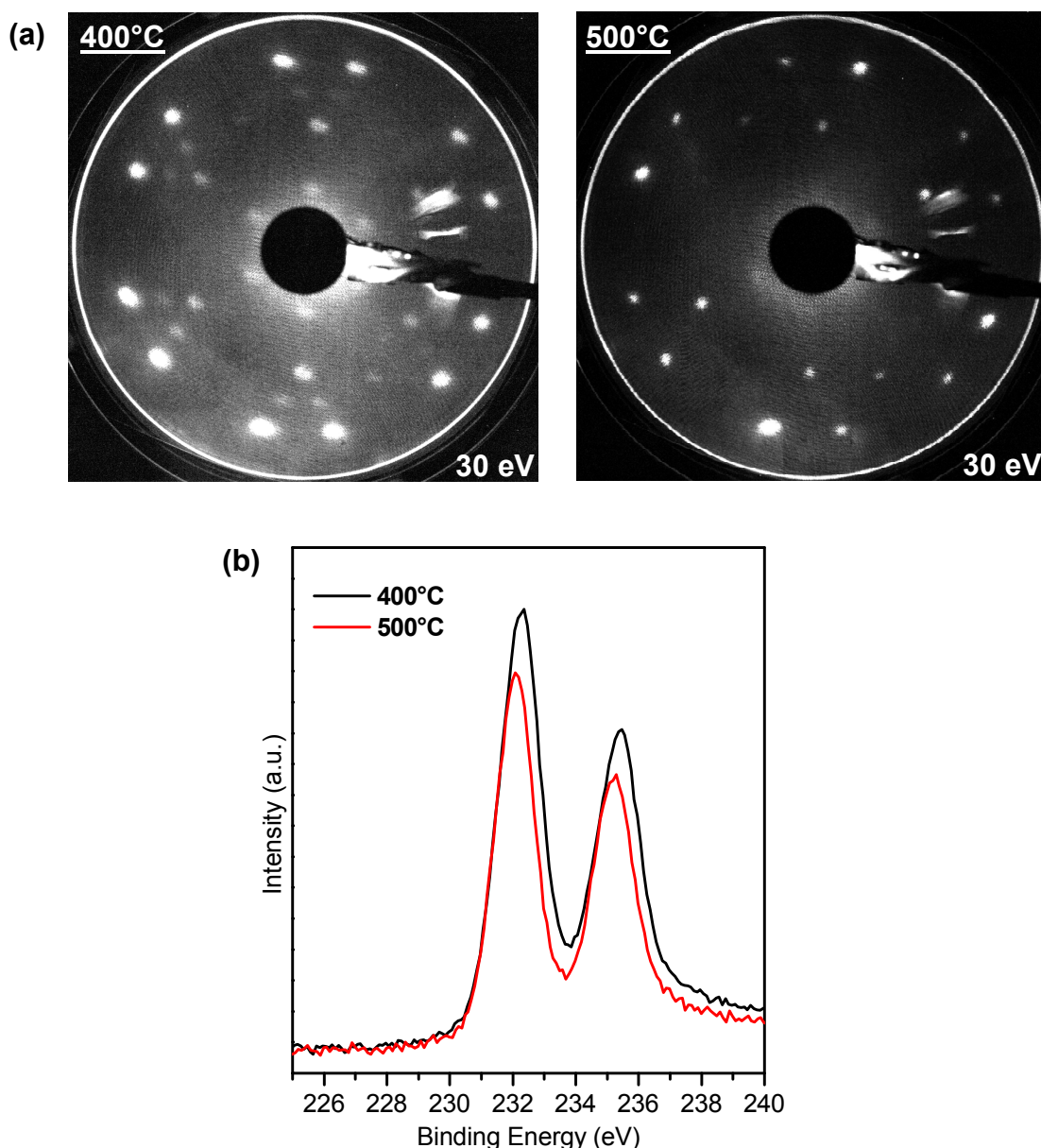


Figure 5.9. Comparison between the films obtained after annealing 0.92 MLE Mo/Au(111) at 400°C for 10 minutes in 50 mbar O₂ and after a subsequent annealing step at 500°C for 25 minutes in 50 mbar O₂. (a) LEED patterns and (b) Mo3d XPS spectra (Mg K α , $\theta = 0^\circ$, intensity normalized to the background intensity at 215 eV).

O 1s NEXAFS data (O K-edge) were acquired for both the c(4x2) monolayer and the thicker film with a 11.6 Å x 5 Å rectangular surface unit cell. The spectra are displayed in Figure 5.10 as a function of the polar angle of the incident linearly polarized X-ray beam (0° is defined as parallel to the surface normal). The films were both prepared by the oxidation of 0.92 MLE Mo in 50 mbar O₂, at a temperature of 400°C for the thicker film and at 500°C for the c(4x2) monolayer. The spectra were acquired by monitoring the electrons emitted from the sample surface with a partial yield detector as a function of the beam energy. The most interesting part of the spectra is the energy region between 529 eV and 537 eV, which is

dominated by two peaks that arise from the excitation of O1s core electrons into unoccupied orbitals with antibonding O2p + Mo4d character¹⁴³. The peak at lower energy (maximum at 530.2 eV) can be ascribed to the antibonding orbitals where the O2p admixture points *perpendicular* to the corresponding O-Mo bond. The other peak appears at about 534 eV and refers to orbitals with O2p admixture pointing *along* the O-Mo bond. The higher antibonding character of this orbital explains the occurrence of the corresponding peak at a higher energy. The spectra are similar for both thin films to some extent. Particularly, the angular dependence of the various features is well comparable. This is indicative of rather similar bonding geometry around the Mo centers and analogous orientation of the coordination units for both films.

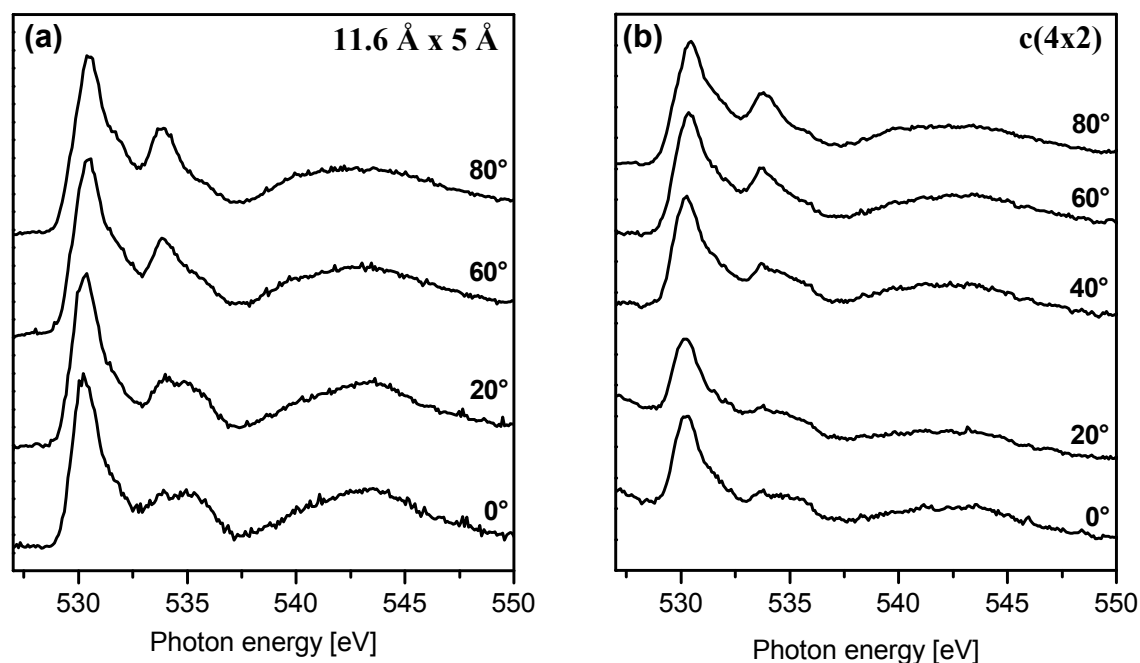


Figure 5.10. Angle-resolved O1s NEXAFS spectra (O *K*-edge) for - (a) a film with a 11.6 Å x 5 Å rectangular surface unit cell and (b) a c(4x2) monolayer - obtained by the oxidation of 0.92 MLE Mo/Au(111) in 50 mbar O₂ at 400 °C and 500 °C, respectively. In both cases the polar incidence angle of the photon beam was varied between 0° and 80°, 0° being along the surface normal. Spectra recorded using partial yield detection.

The angular dependence of the high energy peak intensity is particularly interesting, as it roughly follows the trend observed for MoO₃(010) (see Figure 5.17 and ref.¹⁴⁴). The contribution of the O1s core excitation at the various oxygen sites in MoO₃(010) as a function of the photon incidence angle was investigated in details with DFT by Cavalleri *et al*¹⁴³. According to the results of this study, the electronic excitation at the molybdenyl oxygen atoms

(01 in Figure 5.1) is mainly responsible for the observed angular intensity dependence of the high energy peak (534 eV). Since the Mo=O bond is aligned with only a small angle from the $\text{MoO}_3(010)$ surface normal, the intensity of the high energy peak (corresponding to final state orbitals pointing along the bond) will be highest when the photon incidence angle is close to 90° , i.e. when the electric field vector of the X-rays is almost parallel to the surface normal. Likewise, the high energy peak loses intensity when the photon incidence angle decreases. These considerations would therefore support the idea that both the $c(4 \times 2)$ monolayer and the $11.6 \text{ \AA} \times 5 \text{ \AA}$ surface unit cell film contain molybdenyl groups that are oriented at an angle close to the surface normal. Nevertheless, the support of calculations would be necessary to ascertain this assignment.

5.3.2 Thicker films: $\text{MoO}_3(010)$

The oxidation of thicker Mo layers leads to the growth of (010) -oriented $\alpha\text{-MoO}_3$ crystallites, which eventually coalesce to some extent as they get larger. The formation of these crystallites was observed to start after the oxidation of a Mo thickness between 0.92 MLE and 1.15 MLE. Figure 5.11 shows STM images and LEED patterns of a film formed by the oxidation of 1.15 MLE Mo. The LEED patterns correspond well to the ones presented in Figure 5.7 for a film with a $11.6 \text{ \AA} \times 5 \text{ \AA}$ rectangular unit cell, with the addition of faint rings. Depending of the electron beam energy, two rings with a very slightly different diameter can be observed. The larger is observed in (c) (appearing at the outer side of the nearby $11.6 \text{ \AA} \times 5 \text{ \AA}$ spots), while the smaller can be seen in (d) (appearing at the inner side of the nearby $11.6 \text{ \AA} \times 5 \text{ \AA}$ spots). The radiuses of the two rings correspond very well to the lengths of the two unit cell vectors of $\text{MoO}_3(010)$, as depicted in (c). The (010) surface of $\alpha\text{-MoO}_3$ does not relax significantly with respect to the bulk structure and it has a $3.7 \text{ \AA} \times 3.96 \text{ \AA}$ rectangular unit cell^{1,145} (see Figure 5.12). Similar to $\text{V}_2\text{O}_5(001)$, this surface is terminated by molybdenyl O atoms and it exposes three differently coordinated oxygen ions. However, molybdenum ions as such are not exposed on the $\text{MoO}_3(010)$ surface. As mentioned in Chapter 4, the existence of rings in the LEED patterns can be attributed to azimuthal disorder. The LEED patterns therefore indicate the coexistence of domains of the $11.6 \text{ \AA} \times 5 \text{ \AA}$ structure and of $\text{MoO}_3(010)$, the latter having random azimuthal orientations. The STM results complement this observation. Large scale images display a flat film and some crystallites having an apparent height of about 0.7-1.3 nm (Figure 5.11 (a)). Higher resolution images acquired on the top of these crystallites reveal a $\text{MoO}_3(010)$ unit cell (see (b)). Altogether, these results indicate that $\text{MoO}_3(010)$ crystallites start growing after the completion of the film with a $11.6 \text{ \AA} \times 5 \text{ \AA}$ rectangular surface

unit cell, which is probably a two oxide layers-thick film. It is interesting to note that for both vanadium pentoxide and for molybdenum trioxide the film growth on Au(111) starts with the completion of a monolayer and a second layer that have different structures than their bulk counterparts, which is then followed by the growth of bulk-like crystallites. This is most probably related to the fact that both oxides have similar structure and reactivity.

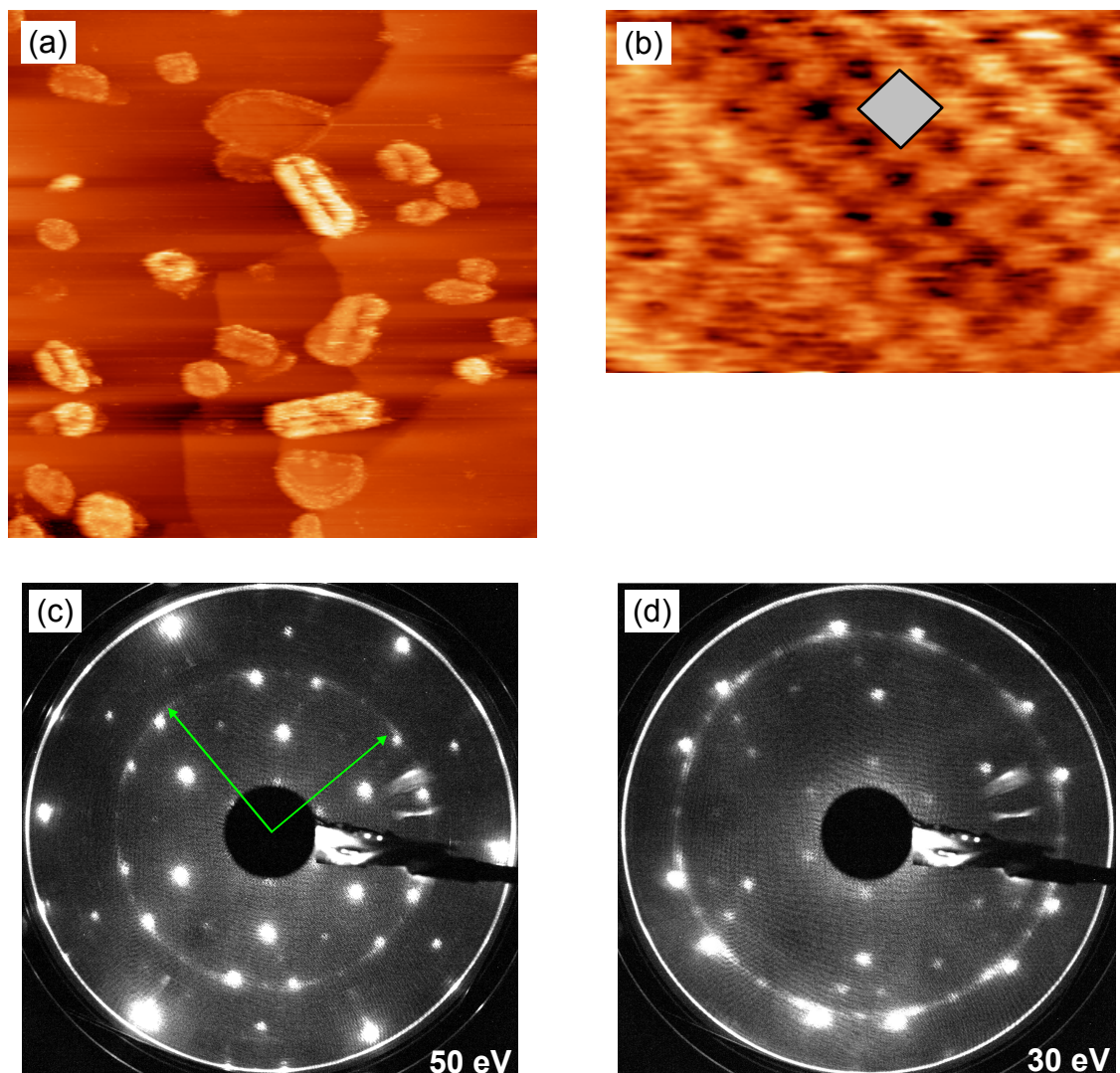


Figure 5.11. STM images ((a): 300 nm x 300 nm, 2.5 V, 0.2 nA, (b): 3.2 nm x 2.2 nm, 2.5 V, 0.2 nA) and LEED patterns (c, d) obtained after annealing 1.15 MLE Mo/Au(111) in 50 mbar O₂ at 400°C for 10 minutes. Image (b) was acquired on one of the brighter areas observed in (a). The reciprocal space unit cell vectors of MoO₃(010) are shown in (c).

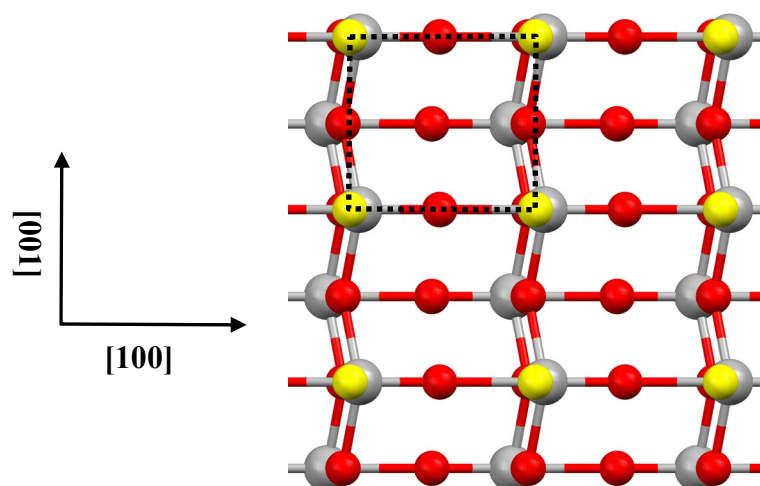


Figure 5.12. α -MoO₃(010) geometric structure¹²⁹. Gray spheres indicate the position of the molybdenum atoms while yellow and red spheres pertain to oxygen atoms (yellow indicating molybdenyl O atoms). The unit cell is indicated by a dotted line.

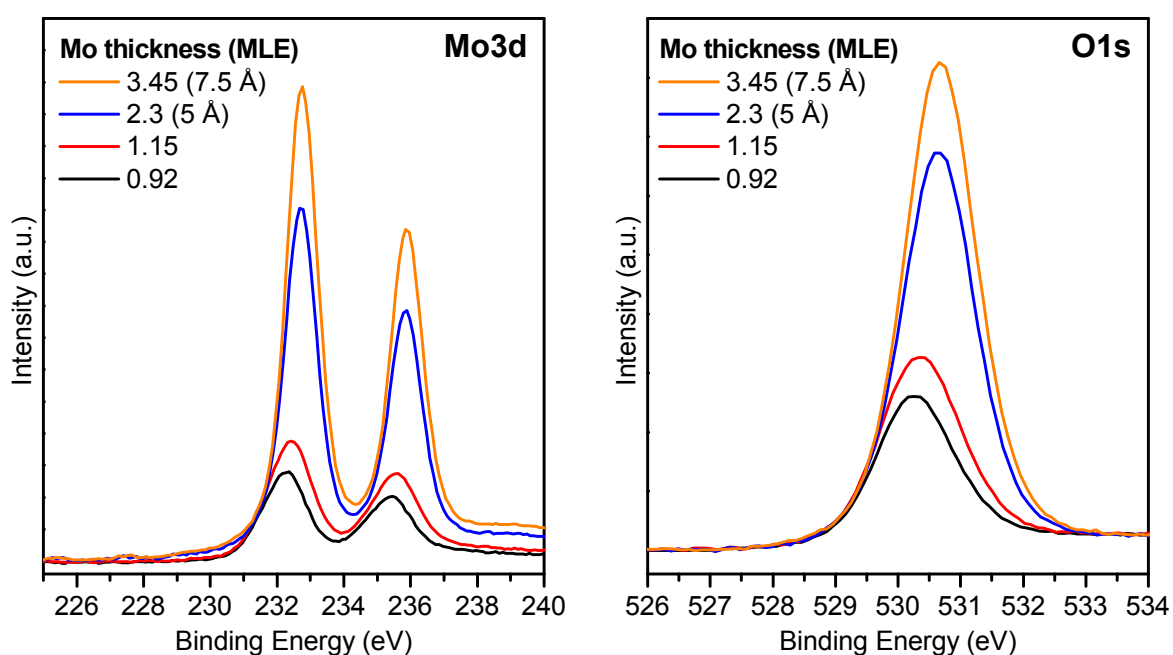


Figure 5.13. Comparison of the Mo3d and O1s XPS spectra for films obtained after the oxidation of different Mo thicknesses on Au(111) (50 mbar O₂ at 400°C for 10 minutes). Mg K α , $\theta = 0^\circ$, intensity normalized to the background intensity at 215 eV and 525 eV for the Mo3d and O1s spectra, respectively.

The XPS Mo3d and O1s spectra of the 1.15 MLE Mo oxide film described above are compared with spectra obtained for thinner and thicker films in Figure 5.13. In contrast to the spectra of the film with a 11.6 Å x 5 Å rectangular surface unit cell (0.92 MLE Mo), the peaks

are shifted towards higher binding energy and are closer to the positions observed for the thicker films (232.7 eV and 530.65 eV for the Mo3d_{5/2} and O1s, respectively). Their full width at half maximum (FWHM, 1.66 eV for Mo3d_{5/2}) is also larger than the one observed for both the thinner (0.92 MLE Mo: 1.61 eV for Mo3d_{5/2}) and the thicker films (2.3 MLE Mo: 1.25 eV; 3.45 MLE Mo: 1.2 eV for Mo3d_{5/2}). This is due to a spectral contribution of both the “interface” film with a 11.6 Å x 5 Å rectangular surface unit cell and the bulk MoO₃(010) crystallites. As the films get thicker, the contribution of the “interface” layer gradually diminishes and the position of the XPS peaks corresponds well to the one observed for bulk MoO₃

139

STM and LEED results corresponding to a film obtained after the oxidation of 2.3 MLE (~ 5 Å) Mo are shown in Figure 5.14. The imaging of the film surface with STM proved to be quite difficult and very few good pictures could be recorded. Strong tip-surface interaction and frequent crashes were generally observed during imaging. This is due to the fact that MoO₃, being a small band gap insulator (band gap ~ 3.1 eV^{127,131}), is not conductive enough to allow a stable imaging with STM. As a comparison, V₂O₅ has a band gap of about 2.3 eV¹ and could be imaged relatively easily (section 4.3.2). Nevertheless, a few images could still be obtained, some of them at rather high resolution. This could have been facilitated by the presence of a very small amount of oxygen vacancies in the film or the intercalation of traces of H (in the UHV chamber, atomic H is known to be generated at W filaments from residual H₂ and MoO₃ readily dissolves H¹⁹). However, the limited thickness of the film (about 5 oxide atomic layers at most) is probably the decisive factor that allowed imaging with STM in the present case and one can expect that the investigation of thicker films of stoichiometric MoO₃ will not be possible with this method. For instance, such an observation was reported by Smith and Rohrer for MoO₃ single crystals¹⁴⁵ (where atomic force microscopy had to be used instead of STM). A large scale image is displayed in Figure 5.14 (a). Although the picture is rather noisy, it points toward the presence of rather large crystallites (~ 50 nm laterally) and a few holes. Atomically-resolved images acquired on the crystallites like those displayed in (b) and (c) clearly reveal the MoO₃(010) 3.7 Å x 3.96 Å rectangular unit cell (note that the images are slightly deformed due to a drift of the piezo elements). These images also show that the surface of the crystallites has very few point defects.

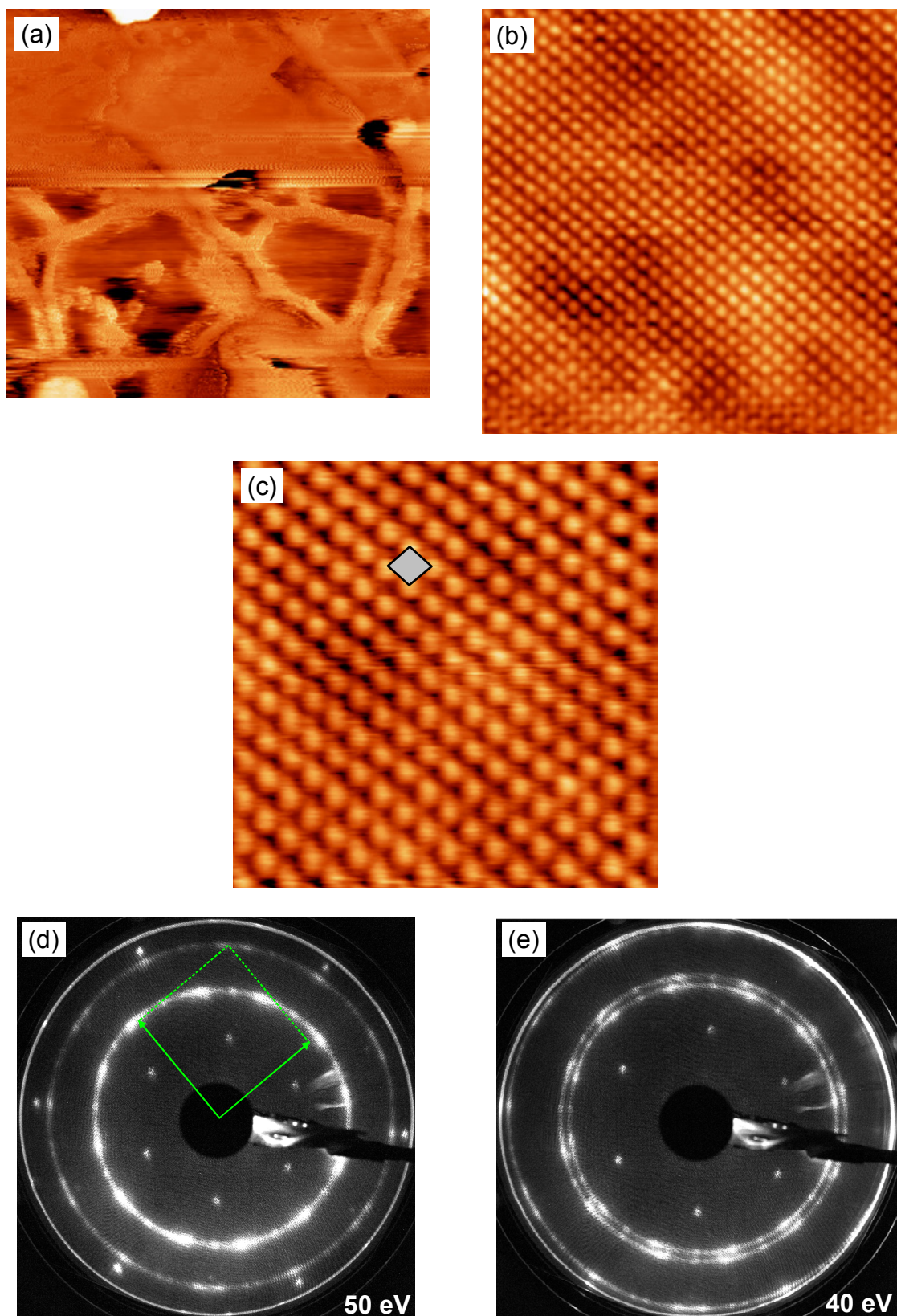


Figure 5.14. STM images ((a): 300 nm x 274.8 nm, 3 V, 0.7 nA, (b): 10 nm x 10 nm, 2.5 V, 0.7 nA, (c): 5 nm x 5 nm, 2.5 V, 0.7 nA) and LEED patterns (d, e) obtained after annealing 2.3 MLE Mo/Au(111) in 50 mbar O₂ at 400°C for 10 minutes. The reciprocal space unit cell vectors of MoO₃(010) are shown in (d).

Due to the random azimuthal orientation of the crystallites, rings are observed in the LEED patterns as seen in Figures 5.14 (d) and (e). As shown in (d), the rings can all be related to $\text{MoO}_3(010)$ spots which are rotated about the (00) spot (directly reflected beam). As observed for the 1.15 MLE Mo oxide film, some rings can appear or disappear as a function of the precise beam energy (compare (d) and (e)). The most intense spots of the $11.6 \text{ \AA} \times 5 \text{ \AA}$ unit cell surface structure can still be detected, which is an indication that some areas of the “interface” are still exposed. These areas probably correspond to the holes observed between some of the crystallites in the large scale STM images. In an attempt to grow “closed” films where the interface layer is not exposed, a thicker film was grown in three successive Mo deposition and oxidation steps (3×1.15 MLE Mo). This approach was tried here since it gave good results for the V_2O_5 thin films (see section 4.3.2). A LEED pattern of this film is displayed in Figure 5.15. Compared to the LEED pattern shown in Figure 5.14 (d), it can be seen that although the diffraction spots related to the interface layer are still present, they are much weaker. They are actually only discernible when the contrast of the image is strongly enhanced (as is the case in Figure 5.15). It therefore seems possible to obtain smooth, well-ordered and “closed” $\text{MoO}_3(010)$ films with this preparation method. Unfortunately, it was not possible to obtain any usable STM images for this film (probably for the reasons mentioned above, the film being thicker).

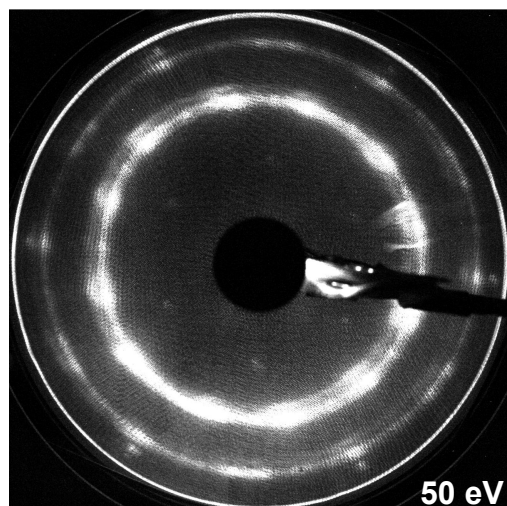


Figure 5.15. LEED patterns obtained for a film formed by three successive steps of 1.15 MLE Mo deposition and oxidation in 50 mbar O_2 at 400°C for 10 minutes (total of 3.45 MLE Mo).

A valence band photoemission spectrum acquired for a film obtained after the oxidation of 2.3 MLE ($\sim 5 \text{ \AA}$) Mo is shown in Figure 5.16. The valence band extends from about 3 eV to 10 eV in the binding energy scale. Its intensity is dominated by O2sp contributions, with a small admixture of Mo4d contributions for the higher binding energy part ^{11,144}. The lowest unoccupied molecular orbital (LUMO) of MoO₃ can be characterized by molybdenum 4d contributions. An increase of the Mo4d occupation due to adsorbate-induced charge transfer or chemical reduction typically results in an increase of intensity between the Fermi edge and 3 eV ^{11,139,144}. The absence of intensity below 3 eV in Figure 5.16 is therefore a strong indication that the MoO₃(010) thin films prepared with the method used in this study contain very few oxygen vacancies.

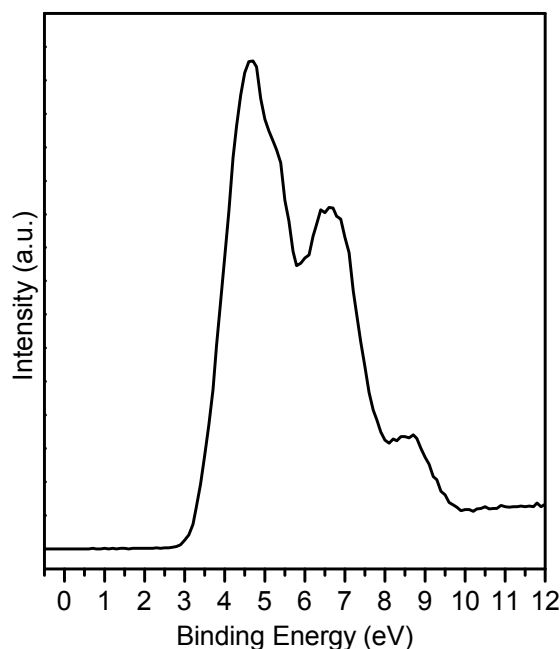


Figure 5.16. Valence band photoemission spectrum of a film formed by the oxidation of 2.3 MLE Mo/Au(111) (50 mbar O₂ at 400°C for 10 minutes). 121 eV photon energy, $\theta = 70^\circ$.

The same film (oxidation of 2.3 MLE Mo) was also investigated with angle-resolved NEXAFS. The spectra were acquired by measuring the current flowing between the sample and ground potential (total electron yield). The Mo $M_{2,3}$ edges and O K -edge spectra are shown in Figure 5.17 for two different photon incidence polar angles. The spectra correspond very well to those obtained on the (010) surface of MoO₃ single crystals ¹⁴⁴, confirming the attribution of the film to MoO₃(010). In contrast to the Mo $M_{2,3}$ spectra, multiplet configurations play no role for the O K -edge (excitonic effects are also believed to be negligible).

Therefore, the spectra can be more directly related to the delocalized band structure as expressed in the partial density of unoccupied states and they are more easily compared to the results of DFT-based calculations. Angle-resolved O1s NEXAFS spectra were calculated by Cavalleri and Hermann for the MoO₃(010) surface and they were found to correspond rather well to our results¹⁴³. As mentioned in section 5.3.1, the peaks below the ionization threshold (< 537 eV) arise from O1s → O2p + Mo4d transitions. The features found at photon energy between 529 eV and 533 eV correspond to transitions to hybridized O2p_π and Mo4d_{t_{2g}} states (π* orbitals, pointing perpendicular to the Mo-O bond). Accordingly, the peaks at higher photon energy, between 533 eV and 536 eV correspond to hybridized O2p_{πσ} and Mo4d_{e_g} states (σ* orbitals, pointing along the Mo-O bond)^{143,144}. The intensity variation of the various peaks as a function of the photon polar angle is predicted to be substantially different for the three types of oxygen centers contained in α-MoO₃. Therefore, the comparison between measured and calculated angle resolved O1s NEXAFS spectra for reduced/defective MoO₃ could give valuable information about the nature of the oxygen vacancies¹⁴³.

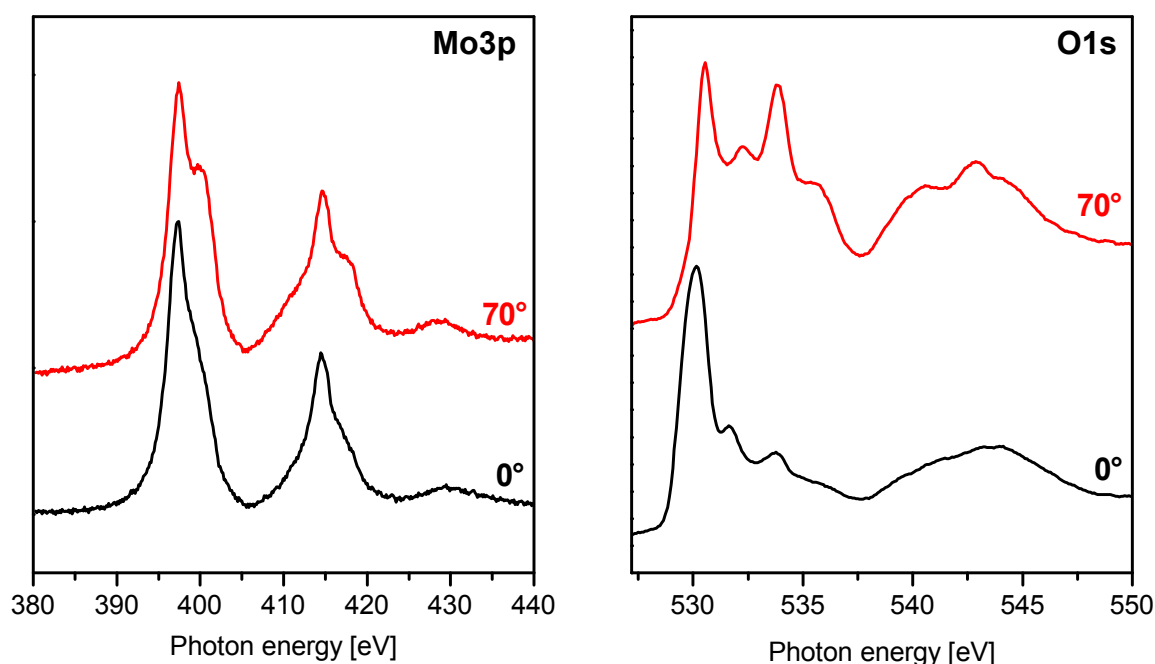


Figure 5.17. Angle-resolved Mo3p (Mo $M_{2,3}$ edges) and O1s (O K -edge) NEXAFS spectra for a film formed by the oxidation of 2.3 MLE Mo/Au(111) (50 mbar O₂ at 400°C for 10 minutes). Photon beam polar incidence angles of 0° and 70°, 0° being along the surface normal. Spectra recorded using total electron yield detection.

The fact that the MoO₃ thin films grow with a [010] orientation is not very surprising and it is due to the fact that (010) is the plane of lowest free energy in α-MoO₃. The growth of

crystallites exposing preferentially their (010) face was also reported by Julien *et al*¹²⁷ and Gaigneaux *et al*¹³² for the deposition of MoO₃ on other substrates.

5.3.3 Thermal stability

Like for vanadium pentoxide thin films (c.f. section 4.3.3), the thermal stability of the MoO₃ layers under UHV conditions is a very important factor in regard to eventual reactivity studies. The possible occurrence of thermal reduction or sublimation of the oxide film itself in the temperature range relevant to catalytic reactions would have a strong influence on the observation of adsorbing and desorbing molecules. For that reason, the MoO₃(010)/Au(111) thin films were investigated with temperature programmed desorption (TPD). A reduction of the film is expected to be accompanied by the emission of O₂ (due to the formation of oxygen vacancies followed by the recombination of O atoms to form O₂ at the surface). Figures 5.18 and 5.19 show the TPD curves obtained for MoO₃(010) films formed by the oxidation of a total of 3.45 MLE Mo and 2.3 MLE Mo, respectively. In both figures, the evolution of the chamber pressure and the O₂ QMS signal ($m/z = 32$) are shown in the lower graph. The upper graphs display the most intense MoO_x mass spectrometer signals, which correspond to MoO₂, MoO and MoO₃ fragments. One should note that these species most probably arise from the fragmentation of larger Mo_xO_y clusters in the electron impact ionization cell of the quadrupole mass spectrometer. Indeed, detailed mass spectrometric studies revealed that Mo_xO_{3x} (with $3 \leq x \leq 5$) are the primary products of the volatilization of MoO₃ in vacuum¹⁴⁶.

The MoO_x desorption curves contain three features between 400°C and 500°C: a rather broad peak centered at about 447°C, a sharp peak at 460°C and some very faint intensity between 470°C and 500°C. The feature centered at 447°C might be attributed to the sublimation of the MoO₃(010) crystallites, while the other peaks observed at higher temperature are probably related to the interface layer. Compared to the V_xO_y TPD signals obtained for the V₂O₅(001) films (c.f. section 4.3.3), the MoO_x curves are qualitatively similar and they also show a broad feature, a sharp peak and finally a broad signal with less intensity as a function of the increasing temperature. Since both films have an analogous structure consisting of bulk-like crystallites lying on top of an interface-specific, two oxide layers-thick film, it is tempting to draw parallels between the sublimation of the two oxides. For the two oxide films, the occurrence of desorption peaks at higher temperature for the interface layer with respect to the bulk-like overlayers could be explained by structural and interlayer adhesion energy differences: the layers (bilayers for MoO₃) in the bulk-like crystals are bound by weak forces (~ van der Waals), whereas the interface layer might be bound more strongly to the

substrate. For instance, the model proposed by Quek *et al*⁹⁴ for the first MoO₃ layer (c.f. section 5.3.1.) describes a polar O-Mo-O oxide film (three atomic layers) that has electronic interaction with the surface atoms of the Au(111) substrate. As postulated for other systems, this oxygen-metal-oxygen interface structure can lead to a relatively high adhesion energy (orders of magnitude higher than nonpolar interfaces), mainly due to the macroscopic Coulomb interaction between the ions in the oxide and the image charges in the metal¹³⁷. Like for V₂O₅, the sharp MoO_x desorption peak observed at 460°C is probably related to the decomposition/sublimation of the second oxide layer. This observation is supported to some extent by the fact that the relative intensity of this peak with respect to the lower temperature “MoO₃(010) overlayers” broad desorption feature increases for thinner films (comparing Figures 5.18 and 5.19). As for the V₂O₅ thin films, the contribution of reduced species to the MoO_x desorption features at higher temperature should not be completely neglected. Nevertheless, the O₂ TPD curve does not show any defined desorption peak that could be related to the film reduction at temperatures up to about 470°C. The broad O₂ desorption peak between 300°C and 420°C is assigned to oxygen desorption from the platinum sample holder (see section 4.3.3). The fact that the same peak is observed for all V₂O₅ and MoO₃ films further supports this assignment. On the other hand, an O₂ desorption peak is clearly observed at 470°C in both Figure 5.18 and 5.19. In the MoO_x desorption curves, the position of this O₂ peak coincides approximately with the beginning of the broad feature that follows the sharp peak. This O₂ desorption peak probably corresponds to the reduction of a remaining MoO₃ monolayer. The thermal reduction of a MoO₃ monolayer on Au(111) in UHV has been investigated by Deng and coworkers¹⁴⁷. The authors found that the reduction of the oxide c(4x2) overlayer occurs through the formation of extended one-dimensional shear plane defects. Although they reported that the reduction occurs at about 375°C, they acknowledged that the actual temperature during their annealing experiment was probably higher since they also observed a partial oxide loss due to sublimation. It is therefore possible that for the films investigated here, a remaining MoO₃ monolayer sublimates and undergoes partial reduction in the temperature range between ~ 470°C and 500°C. No additional desorption features are observed above 500°C, and no traces of molybdenum or oxygen could be detected at the surface of the Au(111) substrate with XPS after the TPD annealing ramp up to 700°C. These observations apparently point toward the fact that most of the film is evaporated after annealing up to 500°C in UHV. It is interesting to note that the c(4x2) MoO₃ monolayer subsists on the substrate even after an extended period of annealing at 500°C in 50 mbar O₂.

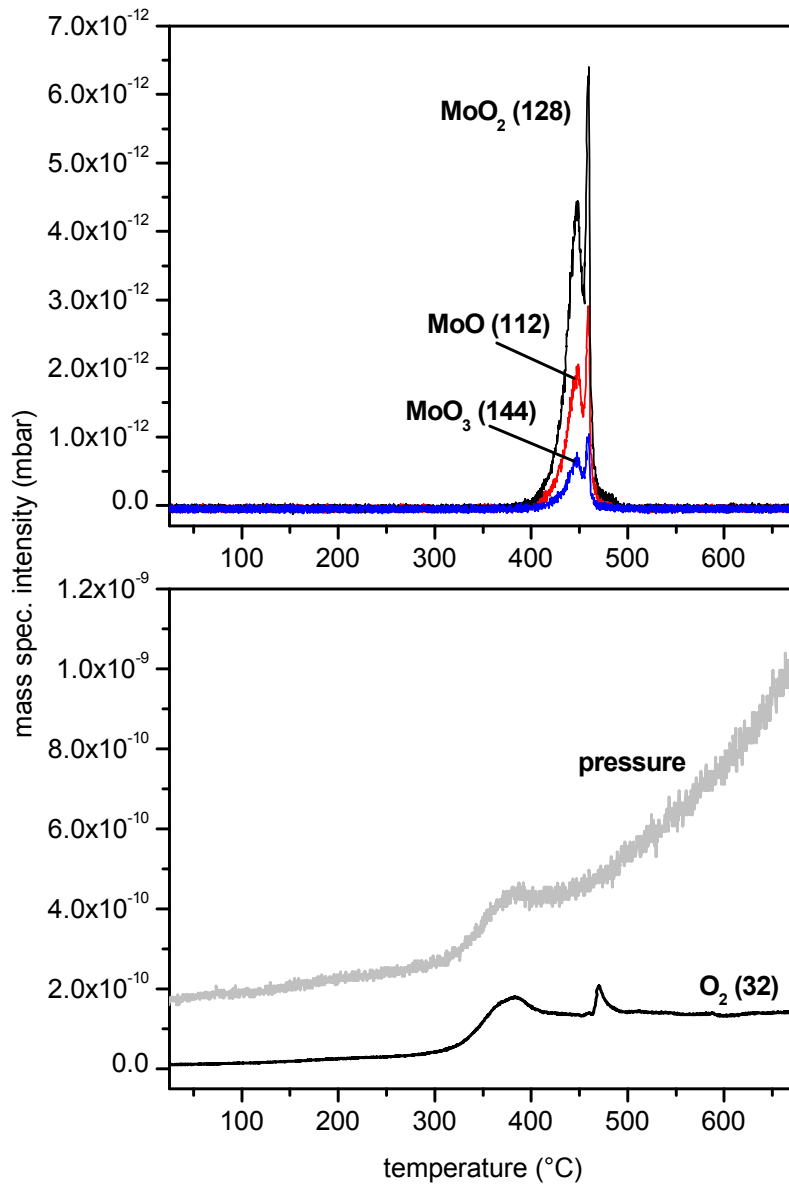


Figure 5.18. TPD of a $\text{MoO}_3(010)$ film formed by three successive steps of 1.15 MLE Mo deposition and oxidation in 50 mbar O_2 at 400°C for 10 minutes (total of 3.45 MLE Mo). The evolution of the main chamber pressure during the TPD run is displayed in the lower graph.

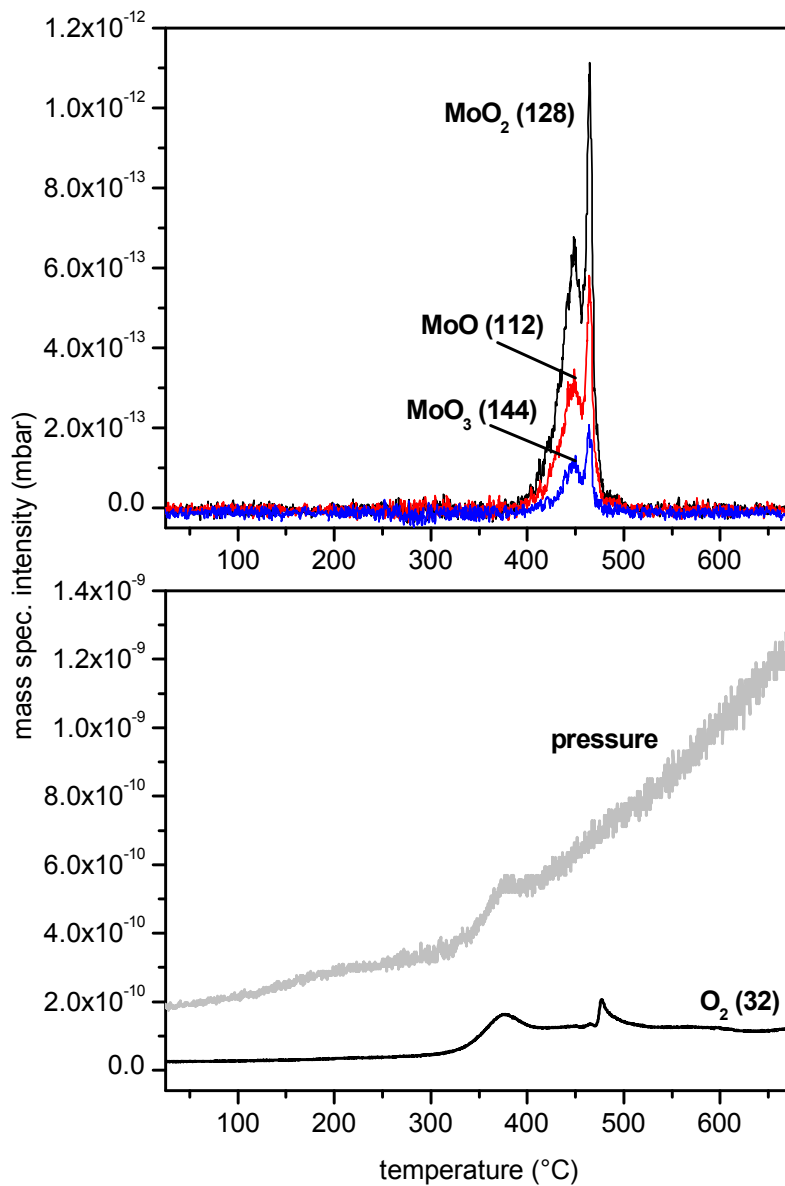


Figure 5.19. TPD of a $\text{MoO}_3(010)$ film formed by the oxidation of 2.3 MLE Mo/Au(111) (50 mbar O_2 at 400°C for 10 minutes). The evolution of the main chamber pressure during the TPD run is displayed in the lower graph.

5.4 Summary

The results presented in this chapter show that well-ordered MoO₃ films can be formed on Au(111) by the oxidation of molybdenum in 50 mbar O₂. At very low Mo coverage, the oxidation leads to a spreading of the material on the Au(111) substrate and to the formation of a c(4x2) MoO₃ monolayer structure. The oxidation of slightly higher Mo coverage apparently results in a 2 layers-thick MoO₃ film with a 11.6 Å x 5 Å rectangular unit cell. These films are interface-specific and they cannot be related to any known bulk structures. These findings are similar to the observations made for V₂O₅ (c.f. Chapter 4) and they highlight the influence of the Au(111) surface on the growth of the thin film. The formation of such interface-specific structures is also most probably facilitated by the easy rearrangement of coordination units in Mo⁶⁺ oxides, and different interface structures are expected to form on other substrates under similar preparation conditions.

Well-ordered MoO₃(010) films containing very few point defects could be prepared for higher thicknesses. Due to the insulating nature of MoO₃, the possibility of investigating the films with STM is rather limited, especially for thicker layers. In that respect, it would be advantageous to use atomic force microscopy (AFM) instead of STM to investigate the surface structure of the films¹⁴⁵.

The films are apparently stable in UHV up to a temperature of about 400°C, above which MoO₃(010) starts sublimating. Also, the TDS data strongly suggest that no substantial reduction occurs until about 470°C. However, this conclusion should be confirmed by post-annealing XPS analysis. The morphological stability of the film under UHV annealing also still needs to be carefully investigated.

It would be quite interesting to study the partial reduction of the MoO₃(010)/Au(111) films with electron irradiation (similar to the investigation done for V₂O₃(0001), presented in Chapter 3). This could shed more light on the open questions regarding the formation of oxygen vacancies at the surface of molybdenum trioxide. Angle-resolved NEXAFS spectra of partially reduced surfaces could be compared to the spectra calculated by Cavalleri *et al* for vacancies at specific oxygen sites¹⁴³. According to their calculations, the creation of oxygen vacancies is most favourable at *O1* and *O2* oxygen sites (see Figure 5.1 (b)). Their models also predict that after relaxation, the formation of either *O1* or *O2* vacancies results in an equivalent *O1** specie (with a bond orientation tilted in between the original *O1* and *O2* positions). The calculations of Coquet and Willock¹⁰ lead to a different conclusion, and experiments could be helpful in resolving this discrepancy.

6 Conclusions and outlook

In the path towards the understanding of the complex reaction mechanisms occurring at the surface of heterogeneous catalysts, the use of model systems is of great advantage and it is often even necessary. These systems are simpler, better defined and allow the investigation of elementary reaction steps. Some suitable models are the surfaces of single crystals and of epitaxial thin films. Such surfaces can be studied at the molecular level using the range of surface science techniques that are nowadays available. Preparing and characterizing model surfaces is a very important step preceding the execution of model reactivity studies. In the present study, the growth and the surface structure of well-ordered V_2O_3 , V_2O_5 and MoO_3 thin films have been investigated.

It is shown that well-ordered $V_2O_3(0001)$ thin films can be prepared on $Au(111)$. The surface structure of the films and the presence of point defects were carefully investigated. The results indicate that oxygen-rich point defects are invariably present on the as-prepared vanadyl-terminated surface. These defects are thermodynamically stable and their quantity can only be limited by careful surface reduction and reoxidation at low temperature and low oxygen partial pressure.

The surface reduction of the vanadyl-terminated $V_2O_3(0001)/Au(111)$ thin films has been investigated with XPS and STM. The assumption made in the previously reported work^{22,23,26} is confirmed: electron irradiation specifically removes the oxygen atoms of the vanadyl groups and results in a V-terminated surface consisting of 3-fold O coordinated V ions. It is possible to control the quantity of removed vanadyl oxygen atoms by using an appropriate electron irradiation dose. This allows the preparation of $V_2O_3(0001)$ surfaces exposing defined densities of vanadyl groups (4-fold coordinated V ions) and 3-fold coordinated V ions. Such surfaces are very interesting, as they potentially constitute suitable models to probe the relative role of both the vanadyl groups and the undercoordinated V ions at the surface of the vanadia catalysts. Reactivity studies using these surfaces are currently in progress^{58,148}.

The preparation of well-ordered $V_2O_5(001)$ and $MoO_3(010)$ thin films is reported here for the first time. These films were grown on $Au(111)$ with a relatively simple method, which consists in oxidizing deposited V or Mo layers under 50 mbar O_2 in a dedicated high pressure cell. Both the simplicity of the preparation method and the fact that the films are well-ordered and contain a low quantity of point defects provide a considerable advantage for the undertaking of model reactivity studies. The thermal stability of these films in UHV has been investigated. The $V_2O_5(001)$ and $MoO_3(010)$ films were found to start sublimating at temperatures

of 500°C and 400°C, respectively. In both cases, no thermal reduction could be observed below the sublimation temperature. A detailed comparison of the results with the published reports on the thermal reduction of V_2O_5 highlights the influence of radiation (photons, electrons) and, more importantly, surface contamination on the observed reduction behavior. This stresses the importance of preparing the surfaces under controlled conditions. At this point, examining the reduction of the $V_2O_5(001)$ and $MoO_3(010)$ films with electron irradiation would be quite interesting.

The formation of interface-specific V_2O_5 and MoO_3 monolayer structures on the Au(111) substrate was observed after the oxidation of low coverages of V and Mo. These layers are found to form coincidence lattices with the Au(111) surface, and they do not correspond to any bulk structure known for vanadium and molybdenum oxides. They are most probably stabilized by the interface with the metal, which perturbs the electronic structure of the oxide¹⁸. The formation of these interface-mediated structures is also made possible due to the fact that both oxides can easily adopt different structures (and oxidation states) through the rearrangement of their coordination units. The growth of V_2O_5 and MoO_3 single layers on other substrates, including other surface planes of Au or crystalline thin films of other oxides for instance, would surely be worth investigating.

It is interesting to note that for both oxides, the formation of a second layer apparently precedes the growth of bulk-like crystallites. In the case of vanadia, this is particularly interesting since it is commonly assumed that V_2O_5 crystals start to grow as soon as a monolayer is completed during the preparation of the so-called “supported monolayer catalysts”⁴.

The high pressure oxidation preparation method used in the present study could potentially be applied to other high oxygen content oxide systems, including TiO_2 , WO_3 , Fe_2O_3 , etc. The preparation of mixed oxides like iron molybdates³ or V_2O_5 - MoO_3 (vanadia-molybdena catalyst¹⁴⁹) could also be of great interest. Nevertheless, one must note that the growth of well-ordered $V_2O_5(001)$ and $MoO_3(010)$ films was facilitated here by the fact that both oxides have a structure consisting of weakly interacting layers and therefore have a strong tendency to expose the low energy surface of these planes. For other oxides, finding a suitable substrate for a defined (epitaxial) crystalline growth direction of the film might be more critical.

References

- (1) Hermann, K.; Witko, M. Theory of physical and chemical behavior of transition metal oxides: vanadium and molybdenum oxides. In *The chemical physics of solid surfaces*; Woodruff, D. P., Ed.; Elsevier Science: Amsterdam, 2001; Vol. 9, Oxide Surfaces (Chapter 4).
- (2) Haber, J.; Witko, M.; Tokarz, R. *Appl. Catal. A* **1997**, *157*, 3.
- (3) Soares, A. P. V.; Portela, M. F.; Kiennemann, A. *Catal. Reviews* **2004**, *47*, 125.
- (4) Wachs, I. E.; Weckhuysen, B. M. *Appl. Catal. A* **1997**, *157*, 67.
- (5) Weckhuysen, B. M.; Keller, D. E. *Catal. Today* **2003**, *78*, 25.
- (6) Grzybowska-Swierkosz, B. *Appl. Catal. A* **1997**, *157*, 263.
- (7) Wachs, I. E. *Catal. Today* **1996**, *27*, 437.
- (8) Deo, G.; Wachs, I. E. *J. Catal.* **1991**, *129*, 307.
- (9) Magg, N.; Immaraporn, B.; Giorgi, J. B.; Schroeder, T.; Bäumer, M.; Döbler, J.; Wu, Z.; Kondratenko, E.; Cherian, M.; Baerns, M.; Stair, P. C.; Sauer, J.; Freund, H.-J. *J. Catal.* **2004**, *226*, 88.
- (10) Coquet, R.; Willock, D. J. *Phys. Chem. Chem. Phys.* **2005**, *7*, 3819.
- (11) Tokarz-Sobieraj, R.; Hermann, K.; Witko, M.; Blume, A.; Mestl, G.; Schlögl, R. *Surf. Sci.* **2001**, *489*, 107.
- (12) Jachmann, F.; Hucho, C. *Solid State Commun.* **2005**, *135*, 440.
- (13) Colpaert, M. N.; Clauws, P.; Fiermans, L.; Vennik, J. *Surf. Sci.* **1973**, *36*, 513.
- (14) Zhang, Z.; Henrich, V. E. *Surf. Sci.* **1994**, *321*, 133.
- (15) Chenakin, S. P.; Silvy, R. Prada; Kruse, N. *J. Phys. Chem. B* **2005**, *109*, 14611.
- (16) Franchy, R. *Surf. Sci. Rep.* **2000**, *38*, 195.
- (17) Street, S. C.; Xu, C.; Goodman, D. W. *Annu. Rev. Phys. Chem.* **1997**, *48*, 43.
- (18) Netzer, F. P. *Surf. Rev. Lett.* **2002**, *9*, 1553.
- (19) Smith, R. L.; Rohrer, G. S. *J. Catal* **1998**, *173*, 219.
- (20) Tepper, B.; Richter, B.; Dupuis, A.-C.; Kuhlenbeck, H.; Hucho, C.; Schilbe, P.; Yarmo, M. A. bin; Freund, H.-J. *Surf. Sci.* **2002**, *496*, 64.
- (21) Mendialdúa, J.; Casanova, R.; Barbaux, Y. *J. Electron Spectrosc. Relat. Phenom.* **1995**, *71*, 249.

- (22) Abu-Haija, M.; Guimond, S.; Romanyshyn, Y.; Uhl, A.; Kuhlenbeck, H.; Todorova, T. K.; Ganduglia-Pirovano, M. V.; Döbler, J.; Sauer, J.; Freund, H. -*J. Surf. Sci.* **2006**, *600*, 1497.
- (23) Abu-Haija, M.; Guimond, S.; Uhl, A.; Kuhlenbeck, H.; Freund, H. -*J. Surf. Sci.* **2005**, *600*, 1040.
- (24) Bandara, A.; Abu-Haija, M.; Höbel, F.; Kuhlenbeck, H.; Rupprechter, G.; Freund, H. -*J. Topics Catal.* **2007**, *46*, 223.
- (25) Czekaj, I.; Hermann, K.; Witko, M. *Surf. Sci.* **2003**, *545*, 85.
- (26) Dupuis, A.-C.; Haija, M. Abu; Richter, B.; Kuhlenbeck, H.; Freund, H.-*J. Surf. Sci.* **2003**, *539*, 99.
- (27) Kresse, G.; Surnev, S.; Schoiswohl, J.; Netzer, F. P. *Surf. Sci.* **2004**, *555*, 118.
- (28) Schoiswohl, J.; Sock, M.; Surnev, S.; Ramsey, M. G.; Netzer, F. P.; Kresse, G.; Andersen, J. N. *Surf. Sci.* **2004**, *555*, 101.
- (29) Todorova, T. K.; Ganduglia-Pirovano, M. V.; Sauer, J. *J. Phys. Chem. B* **2005**, *109*, 23523.
- (30) Feulner, P.; Menzel, D. *J. Vac. Sci. Technol.* **1980**, *17*, 662.
- (31) Wöll, Ch.; Chiang, S.; Wilson, R. J.; Lippel, P. H. *Phys. Rev. B* **1989**, 7988.
- (32) Barth, J. V.; Brune, H.; Ertl, G.; Behm, R. J. *Phys. Rev. B* **1990**, *42*, 9307.
- (33) Ertl, G.; Kupperts, J. *Low energy electrons and surface chemistry*, 2 ed.; Wiley-VCH, 1986.
- (34) Woodruff, D. P.; Delchar, T. A. *Modern Techniques of Surface Science*, 2 ed.; Cambridge University Press, 1994.
- (35) *Scanning tunneling microscopy III: theory of STM and related scanning probe methods*; 2 ed.; Wiesendanger, R.; Guntherodt, H. J., Eds.; Springer-Verlag: New York, 1997.
- (36) Hofer, W. A.; Foster, A. S.; Shluger, A. L. *Rev. Mod. Phys.* **2003**, *75*, 1287.
- (37) Bonnell, D. A. *Prog. Surf. Sci.* **1998**, *57*, 187.
- (38) Horcas, I.; Fernandez, R.; Gomez-Rodriguez, J. M.; Colchero, J.; Gomez-Herrero, J.; Baro, A. M. *Rev. Sci. Instrum.* **2007**, *78*, 013705.
- (39) Hufner, S. *Photoelectron spectroscopy, principles and applications*; 3 ed.; Springer-Verlag: New York, 2003.
- (40) Silversmit, G.; Depla, D.; Poelman, H.; Marin, G. B.; Gryse, R. De. *J. Electron Spectrosc. Relat. Phenom.* **2004**, *135*, 167.

- (41) Moulder, J. F.; Stickle, W. F.; Sobol, P. E.; Bomben, K. D. *Handbook of X-ray Photoelectron Spectroscopy*; Physical Electronics Division, Perkin-Elmer Corporation: Eden Prairie (USA), 1992.
- (42) Fairley, N. CasaXPS version 2.3.10; Casa Software Ltd, 1999-2005.
- (43) Chen, J. G. *Surf. Sci. Rep.* **1997**, *30*, 1.
- (44) Pfuner, F.; Schoiswohl, J.; Sock, M.; Surnev, S.; Ramsey, M. G.; Netzer, F. P. *J. Phys.: Condens. Matter* **2005**, *17*, 4035.
- (45) Dernier, P. D. *J. Phys. Chem. Solids* **1970**, *31*, 2569.
- (46) Czekaj, I.; Witko, M.; Hermann, K. *Surf. Sci.* **2003**, *525*, 46.
- (47) Sawatzky, G. A.; Post, D. *Phys. Rev. B* **1979**, *20*, 1546.
- (48) Zimmermann, R.; Claessen, R.; Reinert, F.; Steiner, P.; Hüfner, S. *J. Phys.: Condens. Matter* **1998**, *10*, 5697.
- (49) Lewis, K. B.; Oyama, S. T.; Somorjai, G. A. *Surf. Sci.* **1990**, *233*, 75.
- (50) Niehus, H.; Blum, R.-P.; Ahlbehrendt, D. *Surf. Rev. Lett.* **2003**, *10*, 353.
- (51) Surnev, S.; Kresse, G.; Sock, M.; Ramsey, M. G.; Netzer, F. P. *Surf. Sci.* **2001**, *495*, 91.
- (52) Xiao, W.; Xie, K.; Guo, Q.; Wang, E. G. *J. Phys. Chem. B* **2002**, *106*, 4721.
- (53) Surnev, S.; Vitali, L.; Ramsey, M. G.; Netzer, F. P.; Kresse, G.; Hafner, J. *Phys. Rev. B* **2000**, *61*, 13945.
- (54) Tasker, P. W. *J. Phys. C: Solid State Phys.* **1979**, *12*.
- (55) Czekaj, I.; Hermann, K.; Witko, M. *Surf. Sci.* **2003**, *525*, 33.
- (56) Rohr, F.; Bäumer, M.; Freund, H.-J.; Mejias, J. A.; Staemmler, V.; Müller, S.; Hammer, L.; Heinz, K. *Surf. Sci.* **1997**, *371*, L291.
- (57) Abus-Haija, M. The surface structure and the chemical activity of V₂O₃(0001) model catalysts. PhD thesis, Technische Universität Berlin, 2006.
- (58) Romanyshyn, Y.; Guimond, S.; Kuhlenbeck, H.; Kaya, S.; Blum, R. -P.; Niehus, H.; Shaikhutdinov, S.; Simic-Milosevic, V.; Nilius, N.; Freund, H. -J.; Ganduglia-Pirovano, M. V.; Fortrie, R.; Döbler, J.; Sauer, J. *Topics Catal.* **2008**, *50*, 106.
- (59) Ramsier, R. D.; Jr., J. T. Yates. *Surf. Sci. Rep.* **1991**, *12*, 246.
- (60) Menzel, D. *Surf. Interface Anal.* **2006**, *38*, 1702.
- (61) Cazaux, J. *J. Electron Spectrosc. Relat. Phenom.* **1999**, *105*, 155.
- (62) Knotek, M. L.; Feibelman, P. J. *Phys. Rev. Lett.* **1978**, *40*, 964.
- (63) Zimmermann, R.; Steiner, P.; Claessen, R.; Reinert, F.; Hüfner, S.; Blaha, P.; Dufek, P. *J. Phys.: Condens. Matter* **1999**, *11*, 1657.

- (64) Dulub, O.; Batzill, M.; Solovev, S.; Loginova, E.; Alchagirov, A.; Madey, T. E.; Diebold, U. *Science* **2007**, *317*, 1052.
- (65) Julien, C.; Guesdon, J. P.; Gorenstein, A.; Khelfa, A.; Ivanov, I. *Appl. Surf. Sci.* **1995**, *90*, 389.
- (66) Murawski, L.; Gledel, C.; Sanchez, C.; Livage, J.; Audières, J. P. *J. Non-Cryst. Solids* **1987**, *89*, 98.
- (67) Ramana, C. V.; Smith, R. J.; Hussain, O. M.; Julien, C. M. *J. Vac. Sci. Technol. A* **2004**, *22*, 2453.
- (68) Silversmit, G.; Poelman, H.; Gryse, R. De. *Surf. Interface Anal.* **2004**, *36*, 1163.
- (69) Wang, X. J.; Li, H. D.; Fei, Y. J.; Wang, X.; Xiong, Y. Y.; Xiong, Y. X.; Nie, Y. X.; Feng, K. A. *Appl. Surf. Sci.* **2001**, *177*, 8.
- (70) Groult, H.; Balnois, E.; Mantoux, A.; Van, K. Le; Lincot, D. *Appl. Surf. Sci.* **2006**, *252*, 5917.
- (71) Bouzidi, A.; Benramdane, N.; Nakrela, A.; Mathieu, C.; Khelifa, B.; Desfeux, R.; Costa, A. Da. *Mater. Sci. Eng. B* **2002**, *95*, 141.
- (72) Madix, R. J.; Biener, J.; Bäumer, M.; Dinger, A. *Faraday Discuss.* **1999**, *114*, 67.
- (73) Magg, N.; Giorgi, J. B.; Schroeder, T.; Bäumer, M.; Freund, H.-J. *J. Phys. Chem. B* **2002**, *106*, 8756.
- (74) Guo, Q.; Lee, S.; Goodman, D. W. *Surf. Sci.* **1999**, *437*, 38.
- (75) Sambti, M.; Negra, M. Della; Granozzi, G. *Thin Solid Films* **2001**, *400*, 26.
- (76) Wong, G. S.; Conception, M. R.; Vohs, J. M. *Surf. Sci.* **2003**, *526*, 211.
- (77) Byström, A.; Wilhelmi, K.-A.; Brotzen, O. *Acta Chem. Scand.* **1950**, *4*, 1119.
- (78) Enjalbert, R.; Galy, J. *Acta Cryst. C* **1986**, *42*, 1467.
- (79) Chambliss, D. D.; Wilson, R. J.; Chiang, S. *Phys. Rev. Lett.* **1991**, *66*, 1721.
- (80) Helveg, S.; Lauritsen, J. V.; Lægsgaard, E.; Stensgaard, I.; Nørskov, J. K.; Clausen, B. S.; Topsøe, H.; Besenbacher, F. *Phys. Rev. Lett.* **2000**, *84*, 951.
- (81) Biener, M. M.; Biener, J.; Schalek, R.; Friend, C. M. *Surf. Sci.* **2005**, *594*, 77.
- (82) Moffat, W. G. *The handbook of binary phase diagrams*; General Electric Company: Schenectady (N.Y.), USA, 1981; Vol. 1.
- (83) Wyckoff, R. W. G. *Crystal Structures, Second Ed.*; Wiley Interscience: New York, 1965.
- (84) Wilhelmi, K.-A.; Waltersson, K.; Kihlberg, L. *Acta Chem. Scand.* **1971**, *25*, 2675.
- (85) Schoiswohl, J.; Sock, M.; Eck, S.; Surnev, S.; Ramsey, M. G.; Netzer, F. P.; Kresse, G. *Phys. Rev. B* **2004**, *69*, 155403.

- (86) Demeter, M.; Neumann, M.; Reichelt, W. *Surf. Sci.* **2000**, 454-456, 41.
- (87) Starr, D. E.; Mendes, F. M. T.; Middeke, J.; Blum, R.-P.; Niehus, H.; Lahav, D.; Guimond, S.; Uhl, A.; Kluener, T.; Schmal, M.; Kuhlenbeck, H.; Shaikhutdinov, S.; Freund, H.-J. *Surf. Sci.* **2005**, 599, 14.
- (88) Abbate, M.; Pen, H.; Czyzyk, M. T.; Groot, F. M. F. de; Fuggle, J. C.; Ma, Y. J.; Chen, C. T.; Sette, F.; Fujimori, A.; Ueda, Y.; Kosuge, K. *J. Electron Spectrosc. Relat. Phenom.* **1993**, 62, 185.
- (89) Chen, J. G.; Kim, C. M.; Frühberger, B.; DeVries, B. D.; Touvelle, M. S. *Surf. Sci.* **1994**, 321, 145.
- (90) Kolczewski, C.; Hermann, K. *J. Chem. Phys.* **2003**, 118, 7599.
- (91) Kolczewski, C.; Hermann, K. *Surf. Sci.* **2004**, 552, 98.
- (92) Biener, M. M.; Friend, C. M. *Surf. Sci.* **2004**, 559, L173.
- (93) Biener, M. M.; Biener, J.; Schalek, R.; Friend, C. M. *J. Chem. Phys.* **2004**, 121, 12010.
- (94) Quek, S. Y.; Biener, M. M.; Biener, J.; Friend, C. M.; Kaxiras, E. *Surf. Sci.* **2005**, 577, L71.
- (95) Smith, R. L.; Rohrer, G. S.; Lee, K. S.; Seo, D.-K.; Whangbo, M.-H. *Surf. Sci.* **1996**, 367, 87.
- (96) Magonov, S. N.; Whangbo, M.-H. *Adv. Mater.* **1994**, 6, 355.
- (97) Blum, R.-P.; Niehus, H.; Hucho, C.; Fortrie, R.; Ganduglia-Pirovano, M. V.; Sauer, J.; Shaikhutdinov, S.; Freund, H.-J. *Phys. Rev. Lett.* **2007**, 99, 226103.
- (98) Oshio, T.; Sakai, Y.; Ehara, S. *J. Vac. Sci. Technol. B* **1994**, 12, 2055.
- (99) Goschke, R. A.; Vey, K.; Maier, M.; Walter, U.; Goering, E.; Klemm, M.; Horn, S. *Surf. Sci.* **1996**, 348, 305.
- (100) Smith, R. L.; Lu, W.; Rohrer, G. S. *Surf. Sci.* **1995**, 322, 293.
- (101) Eyert, V.; Höck, K.-H. *Phys. Rev. B* **1998**, 57, 12727.
- (102) Ganduglia-Pirovano, M. V.; Sauer, J. *Phys Rev B* **2004**, 70, 045422.
- (103) Mathieu, C.; Péralta, S.; Costa, A. Da; Barboux, Y. *Surf. Sci.* **1998**, 395, L201.
- (104) Koma, A. *Thin Solid Films* **1992**, 216, 72.
- (105) Hermann, K.; Witko, M.; Druzinic, R.; Chakrabarti, A.; Tepper, B.; Elsner, M.; Gorschlüter, A.; Kuhlenbeck, H.; Freund, H.J. *J. Electron Spectrosc. Relat. Phenom.* **1998**, 98-99, 245.
- (106) Hermann, K.; Witko, M.; Druzinic, R.; Tokarz, R. *Appl. Phys. A* **2001**, 72, 429.
- (107) Derry, G. N.; Ross, P. N. *Surf. Sci.* **1984**, 140, 165.
- (108) Norton, P. R. *Surf. Sci.* **1975**, 47, 98.

- (109) Dziembaj, R. *Bull. Acad. Polon. Sci.* **1976**, *24*, 965.
- (110) Dziembaj, R. *React. Kinet. Catal. Lett.* **1978**, *9*, 389.
- (111) Lewis, K. B.; Oyama, S. T.; Somorjai, G. A. *Appl. Surf. Sci.* **1991**, *52*, 241.
- (112) Heber, M.; Grünert, W. *J. Phys. Chem. B* **2000**, *104*, 5288.
- (113) Wu, Q.-H.; Thissen, A.; Jaegermann, W.; Liu, M. *Appl. Surf. Sci.* **2004**, *236*, 473.
- (114) Devriendt, K.; Poelman, H.; Fiermans, L. *Surf. Sci.* **1999**, *433-435*, 734.
- (115) Su, D. S.; Schlögl, R. *Catal. Lett.* **2002**, *3-4*, 115.
- (116) Ramana, C. V.; Utsunomiya, S.; Ewing, R. C.; Becker, U. *Solid State Commun.* **2006**, *137*, 645.
- (117) Lindström, R.; Maurice, V.; Groult, H.; Perrigaud, L.; Zanna, S.; Cohen, C.; Marcus, P. *Electrochim. Acta* **2006**, *51*, 5001.
- (118) *Gmelins Handbuch der Anorganischen Chemie*; 8th ed.; Gmelin-Institut, Ed.; Verlag Chemie GmbH: Weinheim (Germany), 1967; Vol. 48 B1.
- (119) *CRC Handbook of Chemistry and Physics*; 84th ed.; Lide, D. R., Ed.; CRC Press: New York, 2003-2004.
- (120) Berkowitz, J.; Chupka, W. A.; Inghram, M. G. *J. Chem. Phys.* **1957**, *27*, 87.
- (121) Farber, M.; Uy, O. M.; Srivastava, R. D. *J. Chem. Phys.* **1972**, *56*, 5312.
- (122) Gao, W.; Altman, E. I. *Surf. Sci.* **2006**, *600*, 2572.
- (123) Gao, W.; Wang, C. M.; Wang, H. Q.; Henrich, V. E.; Altman, E. I. *Surf. Sci.* **2004**, *559*, 201.
- (124) Bowker, M.; Carley, A. F.; House, M. *Catal. Lett.* **2008**, *120*, 34.
- (125) Ressler, T.; Wienold, J.; Jentoft, R. E.; Girgsdies, F. *Eur. J. Inorg. Chem.* **2003**, *2*, 301.
- (126) Moraes, M. A. Bica de; Trasferetti, B. C.; Rouxinol, F. P.; Landers, R.; Durrant, S. F.; Scarminio, J.; Urbano, A. *Chem. Mater.* **2004**, *16*, 513.
- (127) Julien, C.; Khelfa, A.; Hussain, O. M.; Nazri, G. A. *J. Cryst. Grow.* **1995**, *156*, 235.
- (128) Fleisch, T. H.; Zajac, G. W.; Schreiner, J. O.; Mains, G. J. *Appl. Surface Sci.* **1986**, *26*, 488.
- (129) Kihlberg, L. *Ark. Kemi* **1963**, *21*, 357.
- (130) Al-Kuhaili, M. F.; Durrani, S. M. A.; Khawja, E. E. *Thin Solid Films* **2002**, *408*, 188.
- (131) Hussain, O. M.; Rao, K. Srinivasa; Madhuri, K. V.; Ramana, C. V.; Naidu, B. S.; Pai, S.; John, J.; Pinto, R. *Appl. Phys. A* **2002**, *75*, 417.
- (132) Gaigneaux, E. M.; Fukui, K.; Iwasawa, Y. *Thin Solid Films* **2000**, *374*, 49.
- (133) Katrib, A.; Logie, V.; Saurel, N.; Wehrer, P.; Hilaire, L.; Maire, G. *Surf. Sci.* **1997**, *377-379*, 754.

- (134) Smuddle, G. H.; Stair, P. C. *Surf. Sci.* **1994**, *317*, 65.
- (135) Zhang, C.; Hove, M. A. van; Somorjai, G. A. *Surf. Sci.* **1985**, *149*, 326.
- (136) Schroeder, T.; Zegenhagen, J.; Magg, N.; Immaraporn, B.; Freund, H.-J. *Surf. Sci.* **2004**, *552*, 85.
- (137) Radican, K.; Berdunov, N.; Manai, G.; Shvets, I. V. *Phys. Rev. B* **2007**, *75*, 155434.
- (138) Petukhov, M.; Rizzi, G. A.; Domenichini, B.; Granozzi, G.; Bourgeois, S. *Surf. Sci.* **2007**, *601*, 3881.
- (139) Werfel, F.; Minni, E. *J. Phys. C: Solid State Phys.* **1983**, *16*, 6091.
- (140) Saburi, T.; Murata, H.; Suzuki, T.; Fujii, Y.; Kiuchi, K. *J. Plasma Fusion Res.* **2002**, *78*, 3.
- (141) Biener, M. M.; Biener, J.; Schalek, R.; Friend, C. M. *J. Chem. Phys.* **2004**, *121*, 12010.
- (142) Hermann, K.; Hove, M. A. Van. LEEDpat21, 2006.
- (143) Cavalleri, M.; Hermann, K.; Guimond, S.; Romanyshyn, Y.; Kuhlenbeck, H.; Freund, H.-J. *Catal. Today* **2007**, *124*, 21.
- (144) Sing, M.; Neudert, R.; Lips, H. von; Golden, M. S.; Knupfer, M.; Fink, J.; Claessen, R.; Mücke, J.; Schmitt, H.; Hüfner, S.; Lommel, B.; Assmus, W.; Jung, Ch.; Hellwig, C. *Phys. Rev. B* **1999**, *60*, 8559.
- (145) Smith, R. L.; Rohrer, G. S. *J. Solid State Chem.* **1996**, *124*, 104.
- (146) Fialko, E. F.; Kikhtenko, A. V.; Goncharov, V. B.; Zamaraev, K. I. *J. Phys. Chem. A* **1997**, *101*, 8607
- (147) Deng, X.; Quek, S. Y.; Biener, M. M.; Biener, J.; Kang, D. H.; Schalek, R.; Kaxiras, E.; Friend, C. M. *Surf. Sci.* **2008**, *602*, 1166.
- (148) Göbke, D.; Romanyshyn, Y.; Guimond, S.; Sturm, J. M.; Kuhlenbeck, H.; Döbler, J.; Reinhardt, U.; Ganduglia-Pirovano, M. V.; Sauer, J.; Freund, H. -J. *Angew. Chem. Int. Ed.* **2009**, *submitted*.
- (149) Bielanski, A.; Najbar, M. *Appl. Catal. A* **1997**, *157*, 223.

List of Abbreviations

| | |
|---------|---|
| XPS: | X-ray photoelectron spectroscopy |
| UPS: | ultraviolet photoelectron spectroscopy |
| PES: | photoelectron spectroscopy |
| STM: | scanning tunneling microscopy |
| LEED: | low energy electron diffraction |
| NEXAFS: | near-edge X-ray absorption fine structure |
| TPD: | temperature programmed desorption |
| UHV: | ultrahigh vacuum |
| LDOS: | local density of states |
| MLE: | monolayer equivalent |
| QMS: | quadrupole mass spectrometer |

Publications

1. **S. Guimond**, D. Goebke, Y. Romanyshyn, J. M. Sturm, M. Naschitzki, H. Kuhlenbeck and H.-J. Freund, Growth and characterization of ultrathin V_2O_y ($y \sim 5$) films on Au(111), *J. Phys. Chem. C* **112**, 12363-12373 (2008).
2. **S. Guimond**, J. M. Sturm, D. Goebke, Y. Romanyshyn, M. Naschitzki, H. Kuhlenbeck and H.-J. Freund, Well-ordered $V_2O_5(001)$ thin films on Au(111): Growth and thermal stability, *J. Phys. Chem. C* **112**, 11835-11846 (2008).
3. Y. Romanyshyn, **S. Guimond**, H. Kuhlenbeck, S. Kaya, R.-P. Blum, H. Niehus, S. Shaikhutdinov, V. Simic-Milosevic, N. Nilius, H.-J. Freund, M.V. Ganduglia-Pirovano, R. Fortrie, J. Döbler and J. Sauer, Selectivity in methanol oxidation as studied on model systems involving vanadium oxides, *Topics Catal.* **50**, 106-115 (2008).
4. M. Cavailleri, K. Hermann, **S. Guimond**, Y. Romanyshyn, H. Kuhlenbeck and H.-J. Freund, X-ray spectroscopic fingerprints of reactive oxygen sites at the $MoO_3(010)$ surface, *Catal. Today* **124**, 21-27 (2007).
5. **S. Guimond**, M. Abu Haija, S. Kaya, J. Lu, J. Weissenrieder, S. Shaikhutdinov, H. Kuhlenbeck, H.-J. Freund, J. Döbler and J. Sauer, Vanadium oxide surfaces and supported vanadium oxide nanoparticles, *Topics Catal.* **38**, 117-125 (2006).
6. M Abu Haija, **S. Guimond**, Y. Romanyshyn, A. Uhl, H. Kuhlenbeck, T.K. Todorova, M.V. Ganduglia-Pirovano, J. Dobler, J. Sauer and H.J. Freund, Low temperature adsorption of oxygen on reduced $V_2O_3(0001)$ surfaces, *Surf. Sci.* **600**, 1497-1503 (2006).
7. M. Abu Haija, **S. Guimond**, A. Uhl, H. Kuhlenbeck and H.J. Freund, Adsorption of water on thin $V_2O_3(0001)$ films, *Surf. Sci.* **600**, 1040-1047 (2006).

Selbständigkeitserklärung

Ich versichere hiermit, dass ich die vorliegende Dissertation selbständig erarbeitet und verfasst habe.

Sebastien Guimond
St.Gallen, 04.03.2009